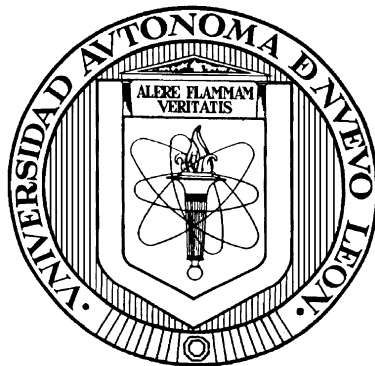


**UNIVERSIDAD AUTÓNOMA DE NUEVO LEÓN**

**FACULTAD DE CIENCIAS QUÍMICAS**



**SYNTHESIS OF ZINC OXIDE NANORODS VIA CONDUCTIVE POLYMERIC  
TEMPLATE AND ITS POTENTIAL APPLICATION  
IN HYBRID SOLAR CELLS**

**Por**

**DENA POURJAFARI NOKANDEH**

**Como requisito parcial para obtener el  
Grado de Doctorado en Ciencias  
con Orientación en  
Química de los Materiales**

**Julio, 2014**

## ***ACKNOWLEDGEMENT***

Finally my Ph.D project arrived at its final point. During these three years I have learned and experienced a lot of things in my life, from the first day when I arrived to Mexico till today that I am writing these final pages.

I remember when I arrived to Mexico, I didn't know Spanish, except some words. Everything was different from my country like the language, the weather, the culture and the FOOD. I had to learn Spanish to be able to communicate with people and manage my life. I had to learn how to eat spicy food, sweating and enjoy my meal!! It was not easy at all but it was all fun since I was in many funny situations learning Spanish!

I had many good moments with my friends and during my travels in Mexico. We made good memories inside the lab, working and doing experiments and outside the lab with our friendly reunions where the science had not any place and it was just for being relaxed and far from the serious scientific life for couple of hours.

As life has "up and down" to maintain its equilibrium, I had also bad moments when I was sick, tired, disappointed or missing my family, friends, language and country. Now I passed all of these good and bad moments and just one thing is left -Its me- a person who has gained more experience in life and ability of manage difficult situations. I really appreciate it and I want to say that the completion of this doctoral dissertation was not possible without the support of many people.

First and foremost I would like to thank to my Ph.D advisor Dr. Idalia Gómez de la Fuente, for her joy, patience, motivation, enthusiasm, and immense knowledge during these past three years. She is such a strong woman and excellent director in research projects and guiding me and her other students. I appreciate her contributions of time, ideas, and funding to make my Ph.D Project. I am also thankful for the excellent example she has provided as a successful woman physicist, researcher and profesor.

Thank to Dra. Yolanda Peña Méndez, Dra. Lorena Leticia Garza Tovar and Dr. Edgar Jocsan Ruiz Ruiz - my thesis committee- for being my advisors and were guiding me through all three years with their questions, recommendations and scientific support.

I would like to express my especial gratitude to Dra. Dora Irma Martinez who offered me using the materials and devices in her laboratory during all these three years. I need to say that without her help I could not finish this project. I am so grateful because she always behaved me like her own students and taught me many useful concepts in electrochemistry.

Thank to Dr. Edgar Omar García Sánchez who helped me a lot by offering me materials and devices when I just wanted to start my project and I didn't have any idea of how the things going on. With his experience in the field of aluminum, he helped me a lot to buy my materials. Thousands of thanks to him for the friendly and nice atmosphere that he provided in the laboratory for all of us to work with higher motivation and forget about the problems and tiredness.

I would like to express my gratitude to engineer Hugo Salas who helped a lot in SEM with his excellent work and knowledge. Also to Dr. Marco Antonio L. Hernandez-Rodriguez who kindly supported me during these years.

I would like to thank to “*Consejo Nacional De Ciencia Y Tecnología (Conacyt)*” for financial supports during these three years, to “*Facultad de Ciencias Químicas*”, “*Facultad de Ingeniería Mecánica y Eléctrica*”, “*Centro de Innovación, Investigación y Desarrollo en Ingeniería y Tecnología (CIDIT)*” and “*Centro de Investigación e Innovación en Ingeniería Aeronáutica (CIIA)*” of “*Universidad Autónoma de Nuevo León (UANL)*” and also “*Instituto de Energías Renovables (IER)*” of “*Universidad Nacional Autónoma de México (UNAM)*”, for giving me the opportunity to obtain my Ph.D degree and doing my research by using the facilities offered by these faculties. Also I would like to thank to “*Red de Nanociencias y Nanotecnología*” that supported me financially for a 3-month internship in “*Instituto de Energías Renovables (IER)*”.

My greatest thanks to my lovely Mexican friends from the laboratory or from other parts of Mexico whom without them I could not finish this project. My friends who made me feel happy and being at home. Thelma Serrano, Gabriela González, Victor Ventura, Karina Cabriales, Antoño Garrido, Angel Valdez, Alejandro Vázquez, Israel Lopez, Mary de la Garza, Shadai Loredo, Erik Gonzalo Salvador Escobar, Thanks a lot to all of you for being always friendly with me and supporting me during these three years. Also I would like to say thanks to my Mexican parents José de la Luz Serrano Ramírez y María Esthela Quezada Cortés for all of their supports when I arrived to Mexico at their house and also during three years of my residence in Mexico.

Special thank to my friend Uriel Vázquez who never left me alone these years and always was in my side helping me and supporting me.

Thanks also to my Iranian friends who filled my loneliness during these years by talking to me or chatting with me and giving me enthusiasm and courage to continue and finish my project. My lovely cousin Mina Saki, my friends Pardis Hamzeie, Atie Behravesht, Ghazale Ghaleie, Azadeh Tabaraie, Marjan Benhari, Maryam Ahmadiani, Hossien Ehsani, Syavash Azarmi, Hoda Emami, Sanaz Ketabi and more and more friends. Thank you so much for your support.

Now I would like to express my special thanks to my parents “Aghdas Fazelpour” and “Mohammad Reza Pourjafari”. I want to tell them that without their support I could not finish this project. Thank to you to be patient and tolerating to be far from me just because I wanted to reach my goals in my life. Thank you mom to be so kind and nice to

give me motivation to finish the thing that I have started. Thanks to my lovely father because of his support and his open-minded personality who always gives me the enthusiasm to being active and enjoy the life. I would like to thank to my brother “Dr. Alborz Pourjafari” who is not just my brother also my best friend. Who I can share with him my happiness and sadness as I cannot share my sadness with my parents!! Thank you Alborz for listening to my secretes! Also I would like to thank to “Dr. Arzu Hushmand” for all of the moments when we were talking and laughing. Thank you Arzu for listening all of my funny histories in Mexico. You make me happy.

At the end I would like to give my thousands of thanks to the objects that participated in my project and without those I never could finish my Ph.D. Thanks to my nice and purple Volkswagen that took me to the school, investigation centers, gym shopping and parties! Thanks to all kind of little small tools like screws, screwdriver, stick tapes, cola Loka, wires, cables, alligators, multimeter, papers, pencils and my laptop which had an outstanding role to do my experiments and writing my thesis.

## ***Table of content***

<b>Chapter</b>	<b>Page</b>
List of figures	i
List of tables	ii
List of abbreviations and chemical substances	iii
Chapter 1. Introduction	1
1. INTRODUCTION	1
1.1 Nanotechnology and solar energy	3
1.1.1 Definition of nano scale and nanotechnology	3
1.1.2 Nanotechnology in solar cells industry	5
2. THESIS MOTIVATIONS	6
3. CHAPTERS DESCRIPTION	6
Chapter 2. Concepts & Literature review	8
2.1 CONCEPTS AND DEFINITIONS	9
2.1.1 Photovoltaic effect	9
2.1.2 Semiconductors	10
2.1.2.1 Definition of semiconductors	10
2.1.2.2 Fundamental and type of semiconductors	10
2.1.3 Reasons for low efficiency of solar cells	12
2.1.4 Important parameters to determine the solar cells performance	12
2.1.5 Materials for solar cells in general	16
2.1.6 Type of solar cells	16
2.1.7 Structure of hybrid solar cells	20
2.1.7.1 Fundamental of hybrid solar cells and device operation	21
2.1.7.2 Ideal materials for hybrid solar cells	22
2.1.7.3 Photoactive layer nanomorphology	23
2.1.8 Synthesis methods for fabrication of one- dimensional nanomaterials	25
2.1.8.1 Template synthesis method	26
2.1.8.1.1 Anodic aluminum oxide (AAO) template	26
2.1.9 Electrochemistry	27
2.1.9.1 Potentiostatic method	29
2.1.9.2 Galvanostatic method	29
2.1.9.3. Cyclic voltammetry (CV)	29
2.1.9.4 Electrochemical Impedance spectroscopy (EIS)	30
2.1.10 Conductive polymers	30
2.1.10.1 Poly (3-hexylthiophene)(P3HT)	32
2.1.11 Metal oxides	32
2.1.11.1 Zinc oxide	32
2.2 Literature review	33
2.3 Hypothesis	46
2.4 General Objectives	46

<b>Chapter</b>	<b>Page</b>
2.5 Specific objectives	47
Chapter 3. Methodology (Synthesis and characterization methods)	49
3.METHODS, MATERIALS AND EXPERIMENTAL CONDITIONS	49
3.1 First step: anodic aluminum oxide (AAO) template fabrication processes	49
3.1.1 Setup and cell design	50
3.1.2 Surface cleaning or Pre-treatment on pure aluminum surface	52
3.1.2.1 Pre-treatments: Mechanical polishing and Electropolishing	53
3.1.3 First anodization step	54
3.1.4 Etching	54
3.1.5 Second anodization step	54
3.1.6 Pore-widening	55
3.1.7 Making the template conductive	56
3.2 Second step: Polymerization- Synthesis of poly (3-hexylthiophene) (P3HT)	59
3.2.1 Chemical polymerization	59
3.2.2 Electrochemical polymerization	61
3.2.2.1 Electrochemical polymerization on ITO substrate	61
3.2.2.2 Electrochemical polymerization on AAO template	62
3.3 Third step: Electrodeposition of Zn oxide	63
3.3.1 Electrochemical deposition of ZnO on ITO	64
3.3.2 Electrochemical deposition of ZnO on AAO template	65
3.4 Characterization methods used in this project	66
3.4.1 Power source	66
3.4.2 Sputtering	66
3.4.3 Microstructural analysis	67
3.4.4 Optical characterization	67
3.4.5 Electrical characterization	68
3.4.6 Surface and structural characterization	69
Chapter 4. Results & Discussions	70
4.1 Pre-treatment on pure aluminum surface	71
4.2 Anodization of aluminum and fabrication of AAO template	72
4.2.1 Control the first anodization and etching time	74
4.2.2 Control the second anodization time	75
4.2.3 Control the pore widening time	77
4.2.4 Al substrate removal to obtain conductive template	78
4.2.5 Comparison between the experimental data and the theoretical formula for template parameters	81
4.3 Polymer synthesis	83
4.3.1 Optical and structural comparison between chemical and electrochemical polymerization	83
4.3.1.1 Fourier transform infrared spectroscopy (FTIR)	84

<b>Chapter</b>	<b>Page</b>
4.3.1.2 X-ray diffraction analysis	85
4.3.1.3 Ultraviolet-Visible spectroscopy (UV-Vis)	86
4.3.1.4 Conductivity measurements	87
4.3.2 Optoelectrical properties of the polymer	90
4.3.2.1 Cyclic voltammetry for polymer E	90
4.3.2.2 HOMO energy level calculation	91
4.3.2.3 Band gap and LUMO energy level calculations from Optical spectroscopy	92
Transmittance spectra	
4.4 Polymer deposition into the pores of AAO template	93
4.4.1 Control of polymeric nanorods length	93
4.4.2 Morphology of P3HT nanostructures	97
4.5 Zinc oxide synthesis	100
4.5.1 Electrochemical study of ZnO deposition	100
4.5.2 Band gap calculation for electrodeposited Zinc oxide on ITO	102
4.5.3 Zinc oxide deposition into the pores of AAO template	103
4.6 Combination of P3HT and ZnO to fabricate hybrid active material	106
4.6.1 Hybrid material-Reflectance	106
4.6.2 Hybrid material-Photoluminescence	107
4.7 Summary	108
Chapter 5. Conclusions	110
5.1 Conclusions	111
REFERENCES	115

## ***List of figures***

<b>Figure</b>		<b>Page</b>
1.1	Order of magnitude of energy sources on earth	2
1.2	Solar direct radiation map for different countries around the world, the bar shows the amount of annual solar energy which is received by different zone on Earth from the Sun	3
2.1	Simple schematic view of photovoltaic phenomena in semiconductor materials	9
2.2	Presentation of semiconductor and comparing between semiconductor materials with metals and insulators . CB is conduction band and VB is valence band	10
2.3	Schematic view of a solar cell, a module and an array	11
2.4	The concept of air mass	13
2.5	Current density–voltage (J–V) characteristics for a solar cell that indicates the three major device characteristics which determine PCE	15
2.6	Equivalent circuit for a real solar cell including series and parallel resistances and photogenerated current	16
2.7	Schematic view of a hybrid solar cell structure consisting of four parts	20
2.8	Schematic diagram of a hybrid solar cell operation, the efficiencies which are presented in equation (2.1) are shown in the diagram	21
2.9	Energy level diagram of an organic– inorganic hybrid solar cell	22
2.10	Schematic views of different types of active layer morphology in hybrid solar cells	24
2.11	Schematic view of (a) bilayer and (b) bulk heterojunction morphology. $e^-$ , $h^+$ , $L_{pol}$ and $L_{ex}$ represent electrons, holes, the thickness of polymeric layer and the exciton diffusion length respectively	24
2.12	Schematic view of charge transport in vertically aligned heterojunction morphology in which $e^-$ , $h^+$ , $L_{pol}$ and $L_{ex}$ represent electrons, holes, the thickness of polymeric layer and the exciton diffusion length respectively	25
2.13	Schematic view of AAO template, $D_p$ is pore diameter, $D_c$ is cell diameter and $t_b$ is the thickness of barrier layer	27
2.14	Schematic structures of conductive polymers	31



<b>Figure</b>		<b>Page</b>
Flowchart 1	Fabrication steps for anodic aluminum oxide template	48
3.1	Left side: Schematic side view of the cell and Right side: Up view of the cell	50
3.2	Structure of the peltier on the left side and peltier itself on the right side	50
3.3	Schematic view of entire set up for anodization process consisting of agitator, cell, peltier, distributor, ventilator and power source	51
3.4	Electropolishing cell with the bowl to pour the electrolyte and the pince for holding the aluminum foil	52
3.5	Schematic view of AAO template fabricated steps	54
3.6	Structure of the AAO template with pure aluminum: Substrate, barrier layer and channels	55
3.7	Steps involved in making conductive template	56
Flowchart 2	Synthesis steps for polymerization of poly (3-hexylthiophene)	58
3.8	Left side: chemical polymerization procedure, Right side: Obtained poly (3-hexylthiophene) by this method	59
3.9	Schematic view of chemical oxidative polymerization mechanism for poly (3-hexylthiophene)	59
3.10	Left side: electrochemical polymerization procedure, Right side: obtained poly (3-hexylthiophene) by this method	61
3.11	Schematic view of electropolymerization mechanism for P3HT C: chemical step and E: electrochemical step	61
3.12	Schematic view of set up for electropolymerization of P3HT onto the channels of AAO template	62
Flowchart 3	Synthesis steps for electrochemical deposition of ZnO	63
3.13	Schematic view of set up for electrodeposition of ZnO on ITO substrate	64
3.14	Schematic view of set up for electrodeposition of ZnO on AAO substrate	65
4.1	AFM images of pure aluminum surface: (a) original surface, (b) after mechanical polishing and (c) after electrochemical polishing	71

<b>Figure</b>		<b>Page</b>
4.2	I-V curve during electropolishing on pure aluminum obtained by potentiostat	72
4.3	Fabricated template on aluminum substrate with diameter of 1 cm	73
4.4	SEM image of AAO template on (a) Al1100 and (b) pure aluminum both after second anodization in oxalic acid 0.3 M at 40 V for 120 min, the image scale is 1 $\mu\text{m}$	73
4.5	SEM image of AAO template (a) First anodization of 30 minutes, etching of 10 min and second anodization of 2 hours (b) First anodization of 2hours, etching of 40 min and second anodization of 2 hours, the image scale is 1 $\mu\text{m}$	75
4.6	SEM images of different templates obtained by changing the etching and second anodization time	76
4.7	Relationship between the template thickness and the second anodization time	77
4.8	The template (a) before pore widening with average pore diameter of 45 nm and (b) after 10 min of pore widening with average pore diameter of 67 nm; the image scale is 1 $\mu\text{m}$	78
4.9	(a) SEM image of template structure after partial removing of aluminum metal, (b) the bottom of pores after complete removing of aluminum metal; the image scale is 1 $\mu\text{m}$	79
4.10	The SEM image showing the bottom of pores; (a) with out pore opening, (b) after 20 min of pore opening, (c) after 35 min of pore opening and (d) after 40 min of pore opening, all in 5wt% phosphoric acid and room temperature. (The image scale is 1 $\mu\text{m}$ )	80
4.11	AAO template fabricated during 2 hours of anodization at 40 V with average pore diameter of 45 nm and the average inter-pore distance of 105 nm	82
4.12	AAO template fabricated during 2 hours of anodization at 40 V with average cell diameter of 138 nm	82
4.13	AAO template fabricated during 2 hours of anodization at 40 V with average barrier layer thickness of 34 nm	83
4.14	FTIR Spectra for the P3HT synthesized by two methods of chemical polymerization (black curve) and electropolymerization(blue dashed curve)	84
4.15	X-ray diffraction pattern for (a) polymer C and (b) polymer E	86

<b>Figure</b>		<b>Page</b>
4.16	Uv-vis spectra for the P3HT synthesized; electrochemical method (blue dashed curve) and chemical polymerization (black curve)	87
4.17	Left side: I-V curve for chemically synthesized P3HT and right side: schematic view of contacts to measure conductivity	88
4.18	Left side: I-V curve for electrochemically synthesized P3HT and right side: the schematic view of the contacts to measure conductivity	89
4.19	Cyclic voltammetry of poly(3-hexylthiophene) in 0.1M TBAPF <sub>6</sub> by applying voltage between -0.1 and +1.8 V, scan rate of 50 mV/s and for 5 cycles	90
4.20	Onset of oxidation peak from the 5th cycle of electropolymerization of P3HT	91
4.21	(a) Tauc plot: $(\alpha hv)^2$ vs. $hv$ extrapolated to zero absorbance for P3HT, the data was collected from the transmittance vs. wavelength (b)	92
4.22	Electropolymerization of P3HT from 50 mM 3HT monomer in 0.1 M TBAPF <sub>6</sub> , at 2 V for 300 seconds. Pt wire, Ag/AgCl and 7 $\mu$ m AAO template were CE, RE and WE respectively. (a) the polymers inside and out of the channels without template removing, (b) how large the polymers are by going out from the channels and laying down on AAO surface, (c) side view of the polymeric rods after template removing in 1 M NaOH solution	95
4.23	Electropolymerization of P3HT from 50 mM 3HT monomer in 0.1 M TBAPF <sub>6</sub> , at 2 V for 100 seconds. Pt wire, Ag/AgCl and 7 $\mu$ m AAO template were CE, RE and WE respectively. The image is after removal of the template in 1M NaOH solution	95
4.24	Electropolymerization of P3HT from 50 mM 3HT monomer in 0.1 M TBAPF <sub>6</sub> , at 2 V for 30 seconds. Pt wire, Ag/AgCl and 7 $\mu$ m AAO template were CE, RE and WE respectively. (a) and (b) both up views, (b) showing the longitude of the polymer rods. The image is after removal of the template in 1M NaOH solution	96
4.25	Electropolymerization of P3HT from 50 mM 3HT monomer in 0.1 M TBAPF <sub>6</sub> , at 2 V for 15 seconds. Pt wire, Ag/AgCl and 3 $\mu$ m AAO template were CE, RE and WE respectively.(a) large-scale image and (b) higher magnification. The image is after partially removal of the template in 1M NaOH solution	97
4.26	Current vs. time for electropolymerization of P3HT in different monomer concentrations of 5 mM, 15 mM and 30 mM during 100 seconds of deposition	98

<b>Figure</b>		<b>Page</b>
4.27	(a) SEM image of P3HT nanotubes, electropolymerization: at 2V, 15 seconds and 5mM of monomer in 0.1 M solution of TBAPF <sub>6</sub> in acetonitrile	99
4.27	(b) SEM image of P3HT partially filled nanotubes, electropolymerization : at 2V, 15 seconds and 15mM of monomer in 0.1 M solution of TBAPF <sub>6</sub> in acetonitrile	99
4.27	(c) SEM image of P3HT nanotubes, electropolymerization: at 2V, 15 seconds and 30mM of monomer in 0.1 M solution of TBAPF <sub>6</sub> in acetonitrile	100
4.28	Schematic view of polymer growth mechanism inside of AAO channels	100
4.29	Cyclic voltammetry for ZnO deposition on ITO from 0.05M zinc nitrate solution at 70 °C; voltage range -1.5 to -0.2 V vs Ag/AgCl, counter electrode: Pt wire, scan rate: 50 mV/s, 5 cycles	101
4.30	(a) Tauc plot: $(\alpha hv)^2$ vs. $hv$ extrapolated to zero absorbance for electrodeposited ZnO, the data was collected from (b) transmittance vs. wavelength	102
4.31	SEM image of electrodeposited ZnO from 0.05 M Zn(NO <sub>3</sub> ) <sub>2</sub> .6H <sub>2</sub> O solution, at -0.95 V and 70 °C and for 1800 seconds	103
4.32	SEM image of electrodeposited ZnO from 0.005 M Zn(NO <sub>3</sub> ) <sub>2</sub> .6H <sub>2</sub> O solution, at -0.95 V and 70 °C and for 1800 seconds	104
4.33	SEM image of electrodeposited ZnO from 0.005 M Zn (NO <sub>3</sub> ) <sub>2</sub> .6H <sub>2</sub> O solution at -0.95 V and 80 °C and for 900 seconds	104
4.34	SEM image of electrodeposited ZnO from 0.005 M Zn(NO <sub>3</sub> ) <sub>2</sub> .6H <sub>2</sub> O solution, at -0.95 V and 80 °C and for 300 seconds after template removal in NaOH 1 M	105
4.35	Reflectance spectra for template, ZnO, P3HT and mixture of P3HT and ZnO	107
4.36	PL spectra for template, ZnO, P3HT and mixture of P3HT and ZnO	108

## *List of tables*

<b>Table</b>		<b>Page</b>
2.1	Classification and efficiencies of different solar cells. The efficiencies measured under the global AM 1.5 spectrum ( $1000 \text{ W/m}^2$ ) at $25 \text{ }^\circ\text{C}$	19
2.2	Properties comparison between conductive polymers	31
2.3	A summarized list of selected hybrid materials and parameters of hybrid solar ce	42
2.4	Comparable assumed characteristics for future hybrid solar cells	45
3.1	Experimental parameters involved in anodization process	57
4.1	Elemental comparison between Al1100 and pure aluminum obtained by optical emission spectroscopy and handbook of aluminum	74
4.2	Comparison between experimental and theoretical parameters	81
4.3	Comparison of FTIR spectra of the polymers synthesized from different method	84
4.4	Parameters for conductivity measurements	89

## ***List of abbreviations and chemical substances***

$^{\circ}\text{C}$ : Celsius degree, temperature unit  
1D: One-dimensional  
3D: Three-dimensional  
AAO: Anodic aluminum oxide  
AC: Alternating current  
AFM: Atomic force microscopy  
Ag: Silver  
AIST: Japanese national institute of advanced industrial science and technology  
Al: Aluminum  
 $\text{Al}_2\text{O}_3$ : Aluminum Oxide  
AM: Air mass  
Amp: Amperes, unit of current  
AN: Acetonitrile  
APTES: (3-Aminopropyl) triethoxysilane  
AR: Aspect ratio= length/diameter  
ASTM: American society for testing and materials  
Au: Gold  
BFEE: Boron trifluoroborate diethyl etherate  
BHJ: Bulk Heterojunction  
 $\text{Bu}_4\text{NBF}_4$ : Tetrabutylammonium tetrafluoroborate  
 $\text{C}_{60}$ : Buckminsterfullerene  
 $\text{C}_B$ : Conduction Band  
Cd: Cadmium  
CdS: Cadmium sulfide  
CdSe: Cadmium Selenide  
CdTe: Cadmium Telluride  
CE: Counter electrode  
 $\text{CeO}_2$ : Cerium (IV) oxide  
 $\text{CHCl}_3$ : Chloroform  
CIGS: Copper Indium Gallium Selenide  
cm: Centimeter, unit of length  
 $\text{cm}^2$ : Square centimeters, unit of area  
 $\text{cm}^3$ : Cubic centimeter, unit of volume  
Cu: Copper  
 $\text{CuInS}_2$ : Copper indium disulfide  
 $\text{CuInSe}_2$ : Copper Indium selenide  
CV: Cyclic voltammetry  
D/A: Donor/Acceptor  
 $D_c$ : Cell diameter  
DC: Direct current  
 $D_{\text{int}}$ : Inter-pore distance  
DMSO: Dimethyl sulfoxide  
 $D_p$ : Pore diameter  
DSSCs: Dye sensitized solar cells  
 $e^-$ : Electron  
E: Electrode potential  
 $E^0$ : Standard electrode potential  
 $E_c$ : Conduction band Energy

E<sub>g</sub>: Band gap Energy  
EIA: Energy Information Administration  
EIS: Electrochemical impedance spectroscopy  
EJ: Exajoule= Energy unit equals to 10<sup>18</sup> Joule  
EQE: External quantum efficiency  
Et<sub>4</sub>NBF<sub>4</sub>: Tetraethylammonium tetrafluoroborate  
eV: Electron volt= Energy unit equals to 1.6021× 10<sup>-19</sup> Joule  
E<sub>v</sub>: Valence band Energy  
f: Faraday's constant =96485.3 C.mol<sup>-1</sup>  
Fe(ClO<sub>4</sub>)<sub>3</sub>: Iron (III) perchlorate  
Fe<sub>2</sub>O<sub>3</sub>: Iron (III) Oxide  
FF: Fill factor  
Ga: Gallium  
GaAs: Gallium Arsenide  
GO: Graphene oxide  
h<sup>+</sup>: Hole  
H<sup>+</sup>: Proton  
H<sub>2</sub>: Hydrogen  
H<sub>2</sub>O: Water  
HOMO: Highest occupied molecular orbital  
HPV: Hybrid photovoltaic  
HSCs: Hybrid solar cells  
I-V plot: Current-Voltage plot  
I<sub>2</sub>: Iodine  
IEA: International Energy Agency  
In: Indium  
InGaAs: Indium Gallium Arsenide  
InGaP: Indium Gallium Phosphide  
I<sub>sc</sub>: Short circuit current  
ITO: Indium tin oxide  
J<sub>m</sub>: Maximum current density  
J<sub>sc</sub>: Short circuit current density  
k: Boltzmann's constant= 1.3806488 ×10<sup>-23</sup> m<sup>2</sup> kg s<sup>-2</sup> K<sup>-1</sup>  
K: Kelvin= temperature unit equal to -272.15 Celsius  
KCl: Potassium chloride  
LED: Light-emitting diode  
L<sub>ex</sub>: Exciton diffusion length  
LiClO<sub>4</sub>: Lithium perchlorate  
LiI: Lithium iodide  
L<sub>PL</sub>: Polymeric layer length  
LUMO: Lowest unoccupied molecular orbital  
m<sup>2</sup>: Square meter, unit of area  
mA: Milliampere  
MDMO-PPV: Poly [2-methoxy-5-(3',7'-dimethyloctyloxy)-1,4-phenylenevinylene]  
MEHPPV: Poly [2-methoxy-5-(2-ethyl-hexyloxy)-1,4-phenylene-vinylene]  
MeOH: Methanol  
meV: Mili electron volt  
MPs: Micropyramids  
n: Number of transferred electrons  
NaOH: Sodium Hydroxide  
Nb<sub>2</sub>O<sub>5</sub>: Niobium Pentoxide

NC: Nanocrystalline  
 nm: Nanometer  
 NPs: Nanoparticles  
 NREL: National renewable energy laboratory  
 NRs: Nanorods  
 NS: Nanostructure  
 NT: Nanotube  
 NW: Nanowire  
 O: Oxidized species  
 O/I: Organic/inorganic  
 OC<sub>1</sub>C<sub>10</sub>-PPV: Poly [(2- methoxy-5-(3',7'-dimethyloctyloxy)-1,4 paraphenylenevi- nylene)]  
 OSC<sub>s</sub>: Organic solar cells  
 P3CT: Poly (3-carboxy-dithiophene)  
 P3HbpT: poly [3-(6-(cyanobiphenyloxy)thiophene)-alt-4,7-(benzothiadiazole)]  
 P3HT: Poly (3-hexylthiophene)  
 P3MT: Poly (3-methylthiophene)  
 P3OT: Poly (3-octylthiophene)  
 Pb: Lead  
 PbS: Lead (II) sulfide  
 PbSe: Lead selenide  
 PCBM: [6,6]-phenyl-C<sub>61</sub> -butyric acid methyl ester  
 PCDTBT: Poly [[9-(1 octylnonyl)-9H-carbazole-2,7-diyl]- 2,5-thiophenediyl-2,1,3 benzothiadiazole-4,7-diyl-2,5-thiophenediyl]  
 PCE: Power conversion efficiency  
 PCPDTBT: Poly [2,6-(4,4-bis-(2-ethylhexyl)-4*H*-cyclopenta [2,1-*b*;3,4-*b'*]dithiophene)-*alt* 4,7(2,1,3-benzothiadiazole)]  
 PDI: Perylenediimide  
 PDDTPD: 2,5-di (thiophen-2-yl)thieno[3,2-*b*]thiopheneand thieno[3,4-*c*]pyrrole-4,6-dione  
 PEDOT: Poly (3,4-ethylenedioxythiophene)  
 P<sub>max</sub>: Maximum output power  
 PSBTBT-NH<sub>2</sub>: Poly [(4,4'-bis(2-ethylhexyl)-dithieno[3,2-*b*:2',3'-*d*]silole)-2,6-diyl-*alt*-(2,1,3-benzothiadiazole)-4,7-diyl]  
 PSiF:DBT: Poly [2,7-(9,9-dioctyl-dibenzosilole)-alt-4,7-bis(thiophen-2-yl)benzo-2,1,3 thiadiazole],Poly [2,1,3-benzothiadiazole-4,7-diyl-2,5-thiophenediyl(9,9-dioctyl-9*H*-9-silafluorene-2,7-diyl)-2,5-thiophenediyl]  
 PSS: Poly (styrenesulfonate)  
 Pt: Platinum  
 PT: Polythiophene  
 PTB7: Poly [[4,8-bis[(2-ethylhexyl)oxy]benzo[1,2-*b*:4,5-*b'*]dithiophene-2,6-diyl][3-fluoro-2-[(2-ethylhexyl)carbonyl]thieno[3,4-*b*]thiophenediyl]]  
 PV: Photovoltaic  
 P<sub>z</sub>: An atomic orbital  
 q: magnitude of the electronic charge  
 QD: Quantum dot  
 Q<sub>e</sub>: Incident light power  
 R: Gas constant = 8.3145 J.mol<sup>-1</sup>.K<sup>-1</sup>  
 R: Reduced species  
 RE: Reference electrode  
 redox: Reduction/Oxidation



R<sub>s</sub>: Series resistance  
R<sub>sh</sub>: Shunt or parallel resistance  
S: Siemens, unit of electrical conductance  
SCs: Solar Cells  
Se: Selenium  
Si: Silicon  
SnO<sub>2</sub>: Tin dioxide  
STC: Standard test condition  
T: Absolute temperature  
t<sub>b</sub>: Barrier layer thickness  
TBAFP<sub>6</sub>: Tetrabutylammonium hexafluorophosphate  
TBAP: Tetraethylammonium perchlorates  
Te: Tellurium  
TiO<sub>2</sub>: Titanium Oxide  
USA: United States of America  
UV-vis: Ultraviolet-Visible  
V: Volts, unit of voltage  
V<sub>B</sub>: Valence Band  
V<sub>m</sub>: Maximum voltage  
V<sub>oc</sub>: Open circuit voltage  
W: Watt, unit of power  
WE: Working electrode  
yr: Year  
ZnCl<sub>2</sub>: Zinc chloride  
Zn(NO<sub>3</sub>)<sub>2</sub>.6H<sub>2</sub>O: Zinc nitrate  
ZnO: Zinc Oxide  
Zn(OH)<sub>2</sub>: Zinc hydroxide  
ZnSe: Zinc selenide  
ZrO<sub>2</sub>: Zirconium Oxide  
ΔE<sub>ES</sub>: Excited energy offset  
ΔE<sub>GS</sub>: Ground state energy offset  
ε<sub>r</sub>: Dielectric constant  
η<sub>A</sub>: Photon absorption yield  
η<sub>cc</sub>: Charge collection yield  
η<sub>diff</sub>: Exciton diffusion yield  
η<sub>diss</sub>: Exciton dissociation yield  
η<sub>tr</sub>: Charge carrier transport yield  
μm: Micrometer  
σ: Sigma: A type of covalent chemical bond

# *Chapter 1*

*Introduction & thesis motivations*

## ***1. INTRODUCTION***

The discovery of the steam engine, which consumed coal as a fuel, in 1712 by *Thomas Newcomen*, was the start of industrialization and changing of the human being's life. Thereafter solid coal, liquid crude oil and natural gas have consumed by human beings as main sources of energy. By increasing the population, consumption and price of the fossil fuels was raised up drastically. For example in the last century the global population has increased by a factor of 4 and the energy demand by a factor of 24 [1]. By considering the concept of the peak oil<sup>1</sup>, in the past few decades the supply has been growing at the same time of the demand, therefore there has been enough oil to meet the demand. However after the peak, the supply reduces and the oil price will rise, so the demand will not be met by supply. According to the international energy agency (IEA) and energy information administration (EIA), from now till 2040 the world population will increase to 9 billion, the world energy consumption will grow by 56% and the worldwide energy-related carbon dioxide emissions increase by 46% [2]. On the other hand the distribution of the fossil fuel resources is not uniform in the world. For example 2/3 of crude oil resources are in the Middle East region and the most petrol consumption is in the USA, Europe and Japan [1]. This causes some problems such as environmental destruction (destroying of the lands, leakage from tanks and pipes) and political issues between countries.

Therefore, today the energy is one of the primary issues of concern and many countries and scientist are searching the new and cost-effective ways to use the renewable sources of energy and reduce reliance on the fossil fuel. There are various renewable sources of energy such as sunlight, wind, hydro, tides, geothermal heat and biomass. Figure 1.1 shows a comparison between annual renewable energy and total non-renewable resources.

The energy content of annual solar radiation which reaches the earth and its atmosphere is 2895000 EJ, compared to the total annual non-renewable energy resources of 325300 EJ for oil, gas, uranium and coal. The energy content of other major renewable

---

<sup>1</sup> If we plot the rate of oil production versus time, there will be a point (peak) which represents the maximum rate of oil production at time.

is estimated as 1960 EJ/yr for wind, geothermal and hydro which is a very small fraction of annual solar radiation. The world energy consumption is about 425 EJ/yr. Although the renewable sources of energy are more available than non-renewable sources, today almost 80% of worldwide energy consumption is based on fossil fuels including 33% of consumption of the oil, 24% of the natural gas and 30% of the coal [2,3]. The annual worldwide energy consumption of 9% comes from the nuclear power and 11% from the renewable energy including 54% from biomass, 31% from hydro, 11% from wind, 3% from geothermal and 1% from solar radiation [2].

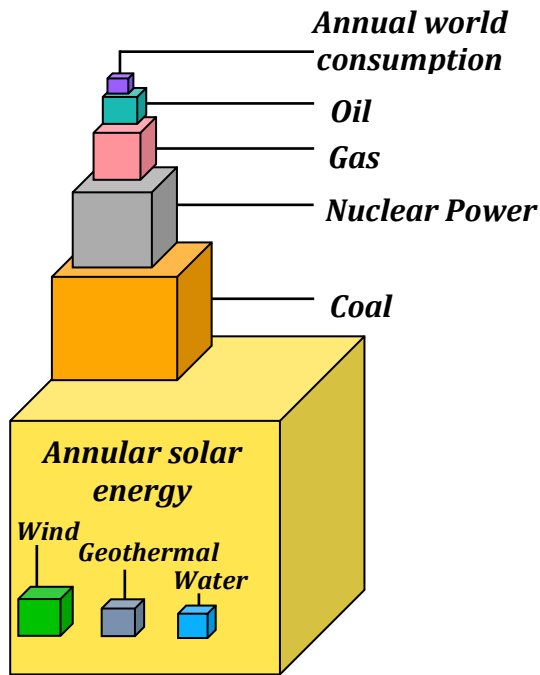


Fig 1.1 Order of magnitude of energy sources on earth [3]

According to this figure, solar energy can be considered the most available renewable energy sources around us.

The human being has used the solar radiation from many centuries ago to set the fire by focusing the sunlight, or warming the houses and cooking the food with sunlight collectors. By the discovery of the photovoltaic effect in 1839 by *Becquerel* and the discovery of the photoconductivity of selenium, the use of solar radiation became more specific. After the first solar cell by *Charles Fritts* in 1883 which made from selenium wafers, many materials like copper oxide, cadmium sulfide and silicon were probed in

the solar cells. Till today many scientists and research groups have proposed different types of solar cells composed from different materials and methods of synthesis.

Figure 1.2 represents the importance of the use of solar radiation. Everyday a vast amount of solar energy is incident on Earth. The energy supply for a solar cell is photons coming from the sun. The amount of solar energy that is received by different places on Earth depends on variables like latitude, time of day and atmospheric conditions over different wavelengths. However many regions received high amount of solar spectra. That's why it is necessary to develop the investigations to utilize the Sun radiation to produce the required energy for human beings and to be independent of the fossil fuel resources and save the next generation and our planet.

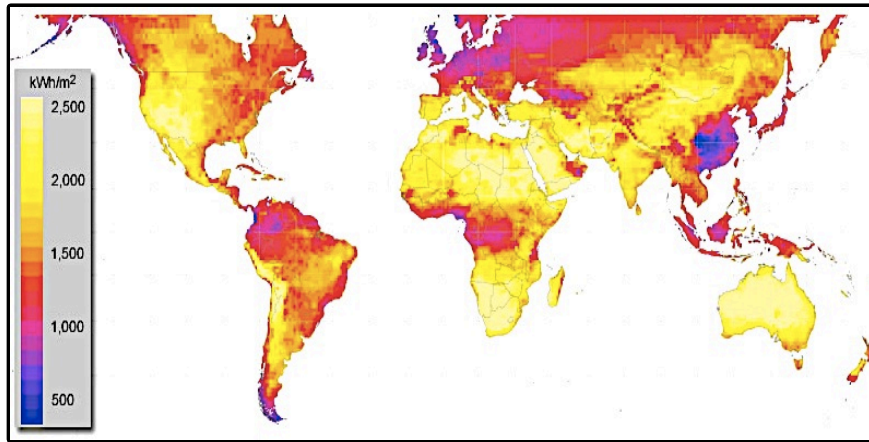


*Fig 1.2 Solar direct radiation map for different countries around the world, the bar shows the amount of annual solar energy which is received by different zone on Earth from the Sun [3]*

## **1.1 Nanotechnology and solar energy**

### **1.1.1 Definition of nano scale and nanotechnology**

In 1974, for the first time *Norio Taniguchi* proposed the term “*nanotechnology*” which is a technology to deal with the materials in nano scale. It means the materials with at least one dimension in the range of 1 to 1000 nanometers ( $10^{-9}$  meter) [4,5].

The nano scale dimension results in the specific mechanical, electrical, thermal, magnetic, optical and chemical properties of nanomaterials and make these materials suitable for a wide range of applications such as electronic and magnetic devices, sensors, energy storage and conversion, semiconductors, medical and biomedical area and

aerospace applications [6]. Unlike bulk materials, properties of nanomaterials are strongly depending on their shapes [7].

Up to now many investigation groups are looking for the reason of this difference between nanoscale and bulk materials. However one reason can be explained by the concept of critical quantum radius. When the particle size becomes small, it approaches the critical quantum radius, which is called Exciton Bohr radius. In this case particle diameter is of the same magnitude as the wavelength of the electron wave function and the electronic and optical properties of the particle is changed. The electronic and optical properties of such a small particle is hence more like those of a molecule than an extended solid. These properties depend not only on the material of which the particle composed but also on its size [8,9, 10,11,12]. Because of the important role of nanomaterials and nanotechnology in human's life, developing our knowledge on the synthesis and characteristics of these materials is necessary.

There are two approaches for the synthesis of nanomaterials; the top-down and bottom-up. In top-down approach large objects are modified to give smaller objects for example synthesis by lithography. In contrast bottom-up approach starts from smaller building blocks which are assembled to fabricate larger structures for example; chemical synthesis [13]. Both approaches have advantages and disadvantages. In general bottom-up approach shows the better results of fabricated nanomaterials with less structural defects, more homogenous chemical composition and better long range ordering compared to the top-down approach. Because the bottom-up approach is based on the reduction of Gibbs energy, so the product of synthesis is in a state closer to a thermodynamic equilibrium state.

Nanomaterials can be zero-dimensional (nanoparticles), one-dimensional (nanowires, nanotubes, nanorods) and two-dimensional (thin film or stacks of thin films) [14]. In this project synthesis and properties of one-dimensional nanomaterials will be mentioned.

Among many applications of nanotechnology in our today lives, the energy conversion and use of the solar radiation is the purpose of this thesis. Next section represents the role of nanotechnology in solar cell application.

### ***1.1.2 Nanotechnology in solar cells industry***

The photovoltaic effect which is the direct conversion of the solar radiation into the electricity takes place in semiconductor materials. Two semiconductors in which one is electron donor and the other one is electron acceptor are coupled together to convert the solar radiation into electricity. Semiconductor materials in nanoscale have higher surface area to volume ratio compare to the bulk materials. The amount of energy converted from sunlight to electricity directly depends upon how many electrons can pass through the interfaces between two layers. Thank to nanotechnology, the efficiency of solar cells and so the use of solar radiation is increasing rapidly. One way that nanotechnology can help, is increasing the size of these interfaces resulting in more pathways for electrons and increasing the efficiency. This characteristic of nanomaterials leads to the better solar radiation collection and efficiency by exposing more conducting surfaces to the sunlight.

As well as increasing the interfaces between two materials, nanotechnology helps to synthesis quantum dot semiconductors (just few nanometers in size) to enhance the performance of solar cells. These quantum dot-small semiconductor solar cells are already used in spacecraft application to replace the heavy and fragile solar cells by a mixture of organic and inorganic nanomaterials to make ultra-lightweight, flexible and low cost solar cells. Not only there are investigations on nano-synthesis of active materials, but also the nanotechnology plays an important role to improve the performance of other parts of solar panels. For example by the aid of nanotechnology, in July 2012 *ecoSolargy* US company has achieved to 6% more absorption efficiency of regular solar modules, by producing the smooth surface panel that prevents water, dust and dirt accumulations, making them self-cleaning, anti-fogging, anti-fading and anti-bacterial without needing for periodical cleaning maintenance that implies costs [15]. Another example is the use of organic dye monolayer by the researchers of Northwestern University in dye-sensitized solar cells. These solar cells suffered from the leakage of their liquid electrolyte leading to poor lifetime and making them commercially unusable. By the aid of nanotechnology the researchers of northwest university proposed a new material for the electrolyte that actually starts as liquid but solidifies at the end and with this innovation, they could achieve the more stable and longer-lasting cells [16].

Using nanoparticles in manufacturing the solar cells results in reducing the fabrication costs because of low temperature synthesis and deposition methods like printing or spraying instead of high temperature vacuum deposition process which is typically used to manufacture conventional crystalline silicon solar cells. Besides of the manufacturing costs, the installation costs also will be reduced by fabrication of flexible panels instead of rigid panels.

Currently available nanomaterials solar cells are not efficient as traditional ones, however by daily development of nanotechnology it is possible to reach the higher efficiency nanomaterials solar cells while the production price is much lower than conventional solar cells.

## ***2. THESIS MOTIVATIONS***

By this brief introduction it can be said that the aim of this work is investigation on nanomaterials synthesis and morphology for solar cells application. These materials are used in new generation of solar cells named “hybrid solar cells”. As it will be explained in the next chapter the contact between the synthesized materials is an important issue of this type of cells. So finding out the optimum experimental conditions to have the better contact between two materials and producing more interfaces between them by the aid of electrochemistry may help to achieve the better performance of hybrid solar cells.

Other goal of this work is obtaining one-dimensional materials by using AAO template. Fabrication of template and the synthesis of photoactive layer of hybrid solar cell consisting of P3HT and ZnO have been studied. This PhD thesis shows that how electrochemistry helps to find the optimum conditions to fabricate a suitable AAO template which used as mold to synthesis the active materials with major interface contact.

## ***3. CHAPTERS DESCRIPTION***

This thesis is divided in five main chapters as followings:

- ❖ The first chapter presents a brief introduction and the motivations of this thesis.



- ❖ The second chapter focuses on some concepts that the reader will encounter while reading this document. In this chapter the previous works from different research groups on hybrid solar cells, the methods and materials and the challenges in this field will be reported. At the end of this chapter the hypothesis, general and specific objectives will be introduced.
- ❖ The third chapter presents the materials, methodology, experimental conditions, set ups and the characterization methods which were applied in this thesis to synthesize and characterize the materials.
- ❖ The fourth chapter represents the experiments results; images, curves and calculations. In this chapter the extensive discussion on obtained results and conclusions are reported.
- ❖ The fifth chapter is conclusion of this work and the future works which may be done to improve the results.

*Chapter 2*  
*Concepts & Literature review*

This chapter contains two parts. Part 2.1 presents the concepts and definitions that are involved with this thesis. This part starts with a description of photovoltaic effect and useful explanation on fundamental and type of semiconductors. Extensive information will be found on solar cells efficiencies up today, the reasons of low efficiency of solar cells, hybrid solar cells definition and their mechanism and information on materials and method using in this project. Part 2.2 is a review of previous studies on hybrid solar cells as well as the challenges and drawbacks of this kind of cells.

## 2.1 CONCEPTS AND DEFINITIONS

### 2.1.1 Photovoltaic effect

The photovoltaic effect is the direct conversion of the solar radiation shining upon the solid or liquid system, into the electricity. This conversion consists of the following steps;

- Absorption of light which causes a transition in absorber material from a ground state to an excited state and the conversion of the excited state into the electron-hole pair.
- The separation of the electrons and holes by the structure of the device in which the electrons go to the negative terminal and the holes to the positive terminal.
- The combination of the electrons with the holes causes returning the absorber in its ground state [17].

These steps of energy conversion from sunlight to electricity occur in p-n junction semiconductor materials.

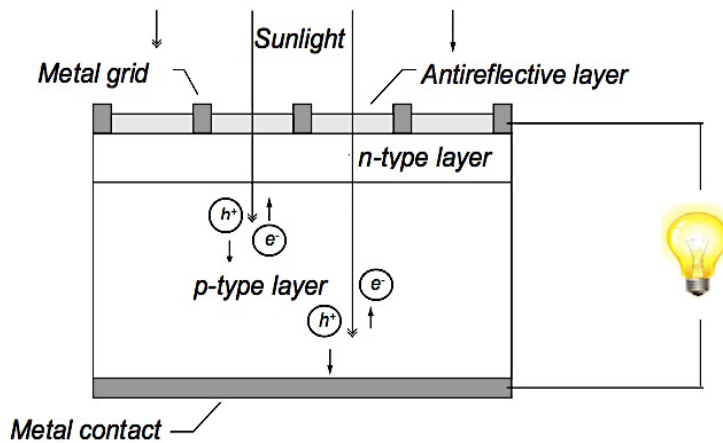


Fig 2.1 Simple schematic view of photovoltaic phenomena in semiconductor materials [17]

## 2.1.2 Semiconductors

### 2.1.2.1 Definition of semiconductors

Semiconductor material is a solid substance which is neither an insulator nor a conductor [18]. As it is shown in figure 2.2 for insulator materials there is a large energy gap between conduction band ( $C_B$ ) and valence band ( $V_B$ ). Because of presence of this energy gap, at ordinary temperature no electron can reach the conduction band from the valence band. This energy gap decreases in semiconductor materials results in the small fraction of the electrons which are weakly bounded with their atoms move from valence band to the conduction band under some conditions such as heating the material or addition of impurities. In the case of conductor materials, there is no difference between the energy level of conduction band and valence band leading to the overlap between them.

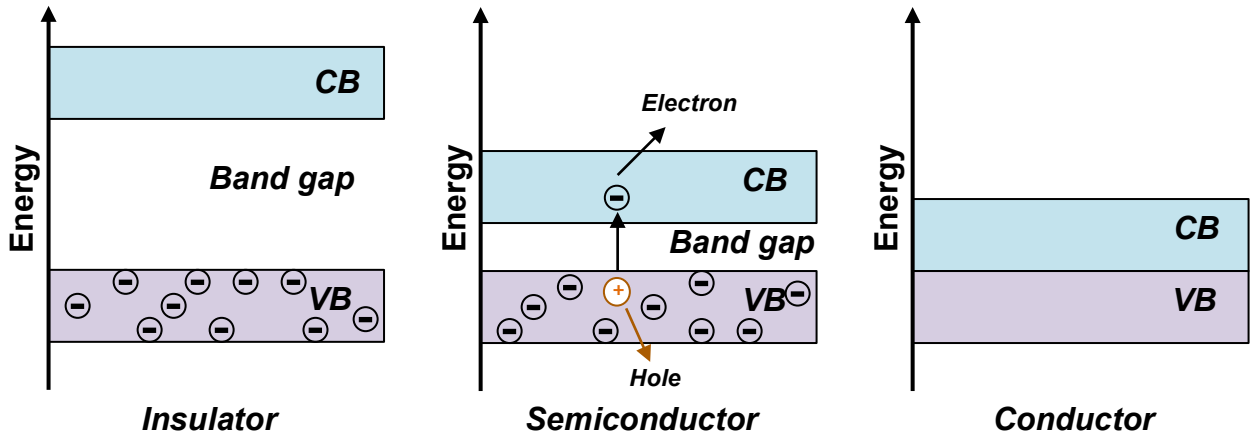


Fig 2.2 Presentation of semiconductor and comparing between semiconductor materials with metals and insulators.  $C_B$  is conduction band and  $V_B$  is valence band [18]

### 2.1.2.2 Fundamental and type of semiconductors

When free atoms form a crystal (like in the case of semiconductor), their discrete energies convert to the bands. The lower band called valence band with the valence band energy ( $E_v$ ), the upper is the conduction band with the conduction band energy ( $E_c$ ) and the gap between them called the band gap with the band gap energy ( $E_g$ ). At zero Kelvin, all the energy levels in valence band are occupied by electrons and those in conduction band are empty.

There are two groups of semiconductors; intrinsic and extrinsic semiconductors. Intrinsic semiconductors are the pure materials like silicon crystal in which at any temperature above 0 K, electrons and holes can be thermally generated without presence of any impurities. For this group the number of the electrons is equal to the number of the holes. However they have high electrical resistivity and low electrical conductivities. This problem can be overcome by doping a semiconductor material with impurities. This group of semiconductor is called extrinsic semiconductors. These impurities change the properties of intrinsic semiconductors. If the impurity leads to extra electrons in semiconductor structure, the impurity called donor and the semiconductor called n-type semiconductor. And if the impurity causes positively charged holes, the impurity called acceptor and the semiconductor is p-type. Binding a p-type semiconductor with n-type results in p-n junction [19].

Solar cells are made of layers of semiconductor materials. Solar cells are generally small and each one maybe produces a DC photovoltage of 0.5 to 1 volts and in short circuit a photocurrent of some tens of milliamps per  $\text{cm}^2$  of the solar cell unit. To produce useful DC voltage, usually 28 to 36 cells are connected together in series and formed a module or panel. A module generates a voltage of 12V in standard illumination conditions. The 12V-module can be used singly or be connected in parallel or series together to form an array with a larger output voltage and current. Figure 2.3 shows solar cell, module and array [17, 20].

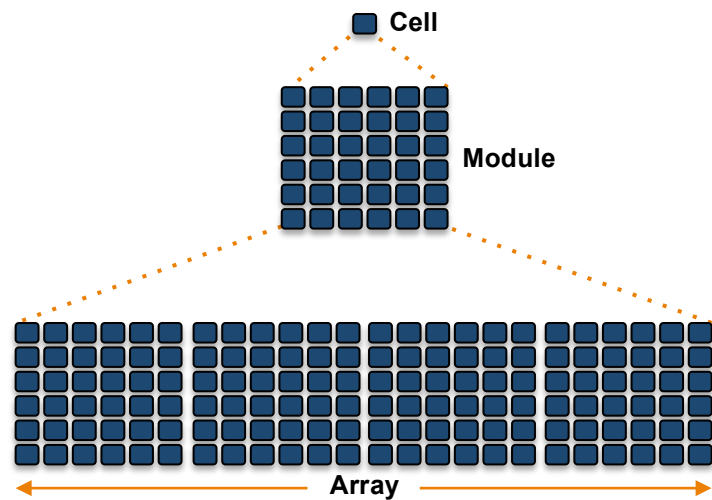


Fig 2.3 Schematic view of a solar cell, a module and an array [17,20]

### ***2.1.3 Reasons for low efficiency of solar cells***

The complete conversion of solar radiation to the electricity never happens in a semiconductor. The solar cell's efficiency and performance is highly dependent on synthesis and morphology of semiconductors. Here the reasons for low efficiency of up-to-date-solar cells are explained.

Certain wavelength detection: a semiconductor can only detect the light with the photon energy bigger than its band gap or with the wavelength shorter than the cutoff wavelength.

Energy loss: when the energy of photon is bigger than the band gap energy this excess energy wastes as heat.

Voltage losses: which happens during the recombination of electrons and holes. It means that the solar cell can never fully use the maximum voltage. To control the open-circuit voltage (the ideal maximum voltage of solar cells), it is necessary to control the number of minority carriers at the junction edges which lead to the fast recombination. The presence of a surface or grain boundary next to the junction also results in fast recombination. To minimize the concentration of minority carriers one way is increasing the concentration of dopant. Another way is lower the speed of recombination by decreasing the length of diffusion path that depends on the type of materials and processing methods.

Structural defects: the defects of the materials stem from their fabrication procedure and synthesis. These defects lead to the current leakage through the edge and decrease the efficiency of solar cells [19].

### ***2.1.4 Important parameters to determine the solar cells performance***

To determine the performance of a solar cell, the voltage, current, external quantum efficiency, power conversion efficiency and fill factor are important parameters. These

measurements must be done under the standard experimental conditions defined by ASTM<sup>2</sup> International [21].

The standard condition for calculation of solar cell's efficiency is introduced as air mass (AM) which is the measure of how far the sun light travels through the Earth's atmosphere and how adsorption in the atmosphere affects the spectral content and intensity of the solar radiation reaching the Earth's surface. Figure 2.4 shows this concept.

$$\text{Air mass (AM)} = \frac{1}{\cos \theta} \quad (2.1)$$

in which  $\theta$  is the angle between the solar incident and the Earth's atmosphere.

AM0 describes the solar radiation in space where it is unaffected by the atmosphere. To determine the efficiency of a solar cell the standard test condition (STC) defines as delivery of 1000W/m<sup>2</sup> of sunlight intensity at 25 °C with airmass of 1.5 (AM1.5) corresponding to  $\theta=48.2^\circ$  [22].

Under these conditions the solar cell performance is determined by following parameters:

External Quantum Efficiency (EQE): is the ratio of photogenerated collected electrons to the number of incident photons at a specific wavelength and is described as:

$$EQE = \eta_A \eta_{diff} \eta_{diss} \eta_{tr} \eta_{cc} \quad (2.2)$$

$\eta_A$ : photon absorption yield, this parameter depends on both band gap and adsorption coefficient of material as well as the thickness of the active layer.

$\eta_{diff}$  : exciton diffusion yield, is the ability of an exciton to diffuse to a donor/acceptor interfaces. This parameter depends on the excitonic diffusion length which is a material

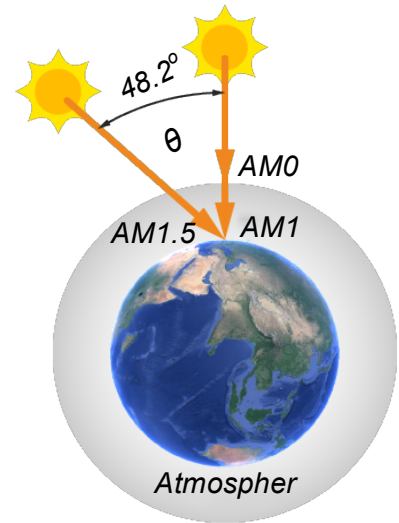


Fig 2.4 The concept of air mass [22]

<sup>2</sup> ASTM International: American Society for Testing and Materials is a globally recognized leader in the development and delivery of international voluntary consensus standards for a wide range of materials, products, systems, and services [21].

property, and the distance between excitation and the nearest interface which can be controlled by architecture of the active layer.

$\eta_{\text{diss}}$ : exciton dissociation yield, defines as an energy offset required to overcome the exciton binding energy to release the electrons from exciton and allow conduction to occur. This energy typically is in the range of 0.1-0.5eV. The exciton dissociation takes place at the boundaries between the two materials and therefore distribution of the interface through the active layer is crucial factor.

$\eta_{\text{tr}}$ : charge carrier transport yield, charge transport occurs by a hopping between energy states and is influenced by traps and recombination sites in the photoactive layer. This parameter depends on the charge mobility of the associated semiconductors.

$\eta_{\text{cc}}$ : charge collection yield, this parameter describes the ability of the charge carriers to be injected into the electrodes from the photoactive layer. This parameter depends on the electronic composition of the device. Large portion of electrons can be injected to the cathode if the magnitude of the conduction band energy level of the acceptor material is less than the work function of the metal. For successful injection of holes into the anode, the magnitude of the HOMO level of the donor material must be higher than work function of the transparent anode.

Power Conversion Efficiency (PCE): which is the ratio of maximum output power to incident light power and is calculated from the equation (2.3):

$$PCE = P_{\text{max}} / \phi_e \quad (2.3)$$

and

Fill factor (FF): which is determined by the equation (2.4):

$$FF = P_{\text{max}} / I_{\text{sc}} V_{\text{oc}} \quad (2.4)$$

In which  $I_{\text{sc}}$  and  $V_{\text{oc}}$  are short circuit current and open circuit voltage respectively and they are measured from I-V plot of the solar cell which is shown in figure 2.5 [17,18,19,20,22,23].



The short circuit current density ( $J_{sc}$ ) is the maximum photocurrent density generated by device under short circuit conditions. The maximum power density obtained from device is given by  $J_m \times V_m$  which is the area of the inner rectangle. The outer rectangle has the area of  $J_{sc} \times V_{oc}$ . If the fill factor becomes equal to 1, the I-V curve would follow the outer rectangle. The power of real cells cannot reach at maximum due to the resistance of the contacts and current leakage around the sides of the device.

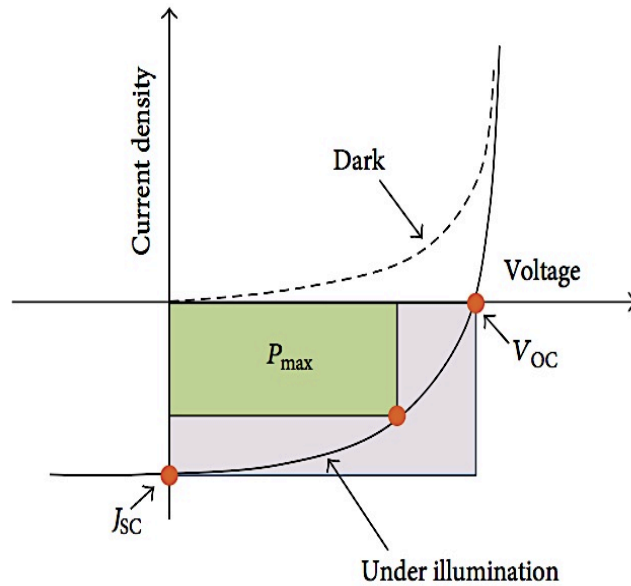


Figure 2.5 Current density–voltage ( $J$ – $V$ ) characteristics for a solar cell which indicates the three major device characteristics which determine PCE [20, 23,24]

These effects come from two resistances in series ( $R_s$ ) and in parallel ( $R_{sh}$ ). The series resistance is due to the resistance of the cell materials and resistive contacts against the flow of current. The parallel or shunt resistance arises from leakage of the current from the edges of the device. Presence of series and parallel resistances reduce the fill factor. For an efficient cell the  $R_s$  should be small that means the high current will flow through the cell at low applied voltage and  $R_{sh}$  should be as large as possible meaning that there are no shorts or leakages of photocurrent in the device. Figure 2.6 shows the equivalent circuit for a cell [25,26].

The series resistance not only comes from the contact between the electrodes and semiconductors but also from the bulk resistance of the blend in the PV device. Contact between a metal and semiconductor materials can either be ohmic or non-ohmic. The

most important non-ohmic barrier is Schottky barrier. For a semiconductor device with one ohmic and one Schottky contact, the current- voltage characteristics is described by Shockley equation as below [25]:

$$I(V) = I_0 \left[ e^{\left( \frac{qV}{nKT} \right)} - 1 \right] \quad (2.5)$$

Where  $I_0$  is the saturation current,  $q$  the magnitude of the electronic charge,  $V$  the applied voltage,  $n$  the ideality factor,  $k$  Boltzmann's constant, and  $T$  the absolute temperature. The ideality factor  $n$  takes account of recombination and tunneling processes and lies between 1 (ideal diode) and 2 (mainly recombination processes) for contacts between a metal and an inorganic semiconductor.

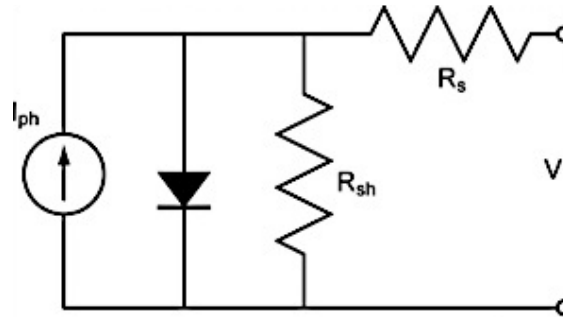


Fig 2.6 Equivalent circuit for a real solar cell including series and parallel resistances and photogenerated current [26]

### 2.1.5 Materials for solar cells in general

One of the important issues in solar cell industry is choosing the proper semiconductor materials which can reach the higher efficiency. Different semiconductor materials including both solid and liquid materials are used for solar cells. These materials can be organic, inorganic, crystalline, polycrystalline or amorphous. To bring this materials in industrial scale, the candidate materials should have some criteria such as direct band gap between 1.1 eV and 3.5 eV, non-toxic, easy synthesis, not expensive, reproducibility in large-scale production and highly stable [20, 27,28].

### 2.1.6 Type of solar cells

Depending on the type of materials, there are 5 main classifications of solar cells as listed in table 1 with corresponding efficiency reported in 2013. After developing of the first **silicon solar cell** in 1954 by *Chapin et al* with the efficiency of 4%, many attempts

were done to increase the efficiency of crystalline Si-based solar cells and they reached to the efficiency of about 25% [28]. However silicon wafer production is costly. Thus the other types of cells with different materials like amorphous silicon, **thin film semiconductors of group III and V**, **dye sensitized solar cells (DSSCs)**, **organic solar cells (OSCs)** and **multijunction devices** have been the center of scientific researches and interests [29]. Possible alternatives to crystalline silicon solar cells are inorganic thin film devices. The lower thickness of these thin films reduces the cost of solar cell industry. The current components used for today technology are Cu(In-Ga)Se<sub>2</sub> and cadmium telluride (CdTe). Although these devices may fabricate from cost-effective methods, their production requires the use of very rare materials. The search for low cost photovoltaic devices has led researchers to organic materials as possible candidate [30]. Conjugated conductive polymers are flexible, lightweight and they have very high absorption coefficient which allows very thin film to be used while still absorbing a sufficient portion of the solar spectrum. The main advantage of these organic solar cells is their low processing cost because of using solution phase methods such as jet printing and roll-to-roll techniques which lead to very cheap and large-scale manufacturing. However they have low power conversion efficiency, low electron mobility typically in the range of  $10^{-4}$  -  $10^{-3}$  cm<sup>2</sup>.V<sup>-1</sup>.S<sup>-1</sup> because of the presence of electron traps such as oxygen and poor operational stability because of phase degradation of organic materials [30,31,32, 33,34,35,36,37]. Other disadvantage is that in contrast to inorganic semiconductors, photo absorption in organic semiconductors does not directly result in the formation of free charge carriers that are required for photovoltaic effect. In silicon solar cells, an incident light breaks a covalent bond and forms an electron-hole pair.

Due to the crystalline nature of silicon lattice, just there is a small interaction force between charge carriers and as a result, absorption in silicon leads to effectively free charge carriers. However, the low relative dielectric constant of organic semiconductors ( $\epsilon_r \approx 3$ ), leads to a large electrostatic force between electron and holes. By incident light to the organic semiconductors, a strongly bound electron-hole pair, or exciton, is generated. It means that the electron and hole are coulombically bound and a force is required to overcome this excitonic binding energy which is in the range of 0.05 – 1.0 eV.

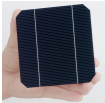
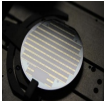
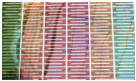
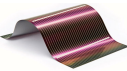
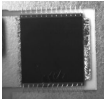
This exciton can be separated into free charge carriers only at the interface between an electron donor (p-type) and electron acceptor (n-type) material where the differences in the electron affinities and the ionization potentials between the contacting materials are sufficiently large to overcome the exciton binding energy. Since the exciton diffusion lengths in conjugated polymer are around 10-20 nm, the optimum distance of the exciton to the donor/acceptor (D/A) interface should be in the same length range [30,38,39,40].

The first polymer solar cells made of *MEHPPV* and  $C_{60}$  had the efficiency of 0.04%. By considering the equation (2.1) for the polymer, the exciton diffusion yield is much lower than unity ( $\eta_{\text{diff}} \ll 1$ ) due to the bigger polymeric layer length in comparison to the exciton diffusion length ( $L_{\text{PL}} > L_{\text{ex}}$ ). Thus the recombination of the electrons and holes take places before the exciton dissociation. Also there are losses during charge transport of electrons and holes to their respective electrodes. It means that  $\eta_{\text{tr}} \ll 1$  and the *EQE* is too low [23,41]. Recently there are more attempts to modify the performance of organic solar cells. One recent way is replacing one of the organic semiconductors with an inorganic semiconductor [42]. In 1994 *Yu et al* demonstrated the dispersion of an inorganic nanomaterial inside the polymeric phase in order to achieve the bulk heterojunction solar cells (*BHJ*) [29,43]. Therefore the new generation of solar cells came through with the name of **hybrid solar cells** (HSCs) with the intent of combining the advantages of both organic and inorganic materials. From one side, inorganic materials still maintaining the low cost processability and from the other hand they are more environmentally stable than organic materials. It means that inserting an inorganic material in polymeric matrix reduces the degradation of the polymer [30,34,38,39,40,44,45,46,47,48,49]. Additionally, quantum confinement that deals with the modification of size and shape of inorganic nanoparticles, leads to change the band gap and thus absorption profile of nanoparticles. Using quantum dots nanoparticles not only extend the window of the absorption profile, but also causes to ultrafast photo-induced charge carrier transfer to organic material. This transfer rate has been observed in the order of picoseconds which is more faster than recombination rate of electron and holes and results in efficient charge transfer between donor and acceptor. Band gap tuning in nanoparticles can be achieved by adjusting the device architecture.

The energy levels of polymers can be tuned by chemical modification of the backbone chain and the energy levels of organic nanomaterials can be tuned through the size-dependent quantum confinement effect. That's why the mixture of two materials offers the possibility of tailoring optimal conditions for solar cells [47]. As mentioned above although there are theoretical advantages associated with using an inorganic acceptor semiconductor in polymeric matrix, the currently achieved efficiency for hybrid solar cells are significantly lower than polymer: fullerene OPV devices. The surface chemistry of materials, the contact between organic and inorganic materials and the morphology of hybrid film are reasons related to this lower efficiency [48,49].

This thesis focuses on synthesis and morphology of nanomaterials in hybrid solar application. For this reason in next section this type of solar cells are introduced extensively.

*Table 2.1 Classification and efficiencies of different solar cells  
The efficiencies measured under the global AM 1.5 spectrum (1000 W/m<sup>2</sup>) at 25 °C [50]*

<b>Classification</b>	<b>Efficiency (%)</b>	<b>V<sub>oc</sub> (V)</b>	<b>J<sub>sc</sub> (mA/cm<sup>2</sup>)</b>	<b>Fill Factor (%)</b>	<b>Test Center</b>
<b>Silicon solar cells</b> Si (crystalline) 	25	0.76	42.7	82.8	Sandia
<b>III-V cells</b> GaAs (thin-film) 	28.8	1.122	29.68	86.5	NREL
<b>Thin-film chalcogenide (CIGS)</b>	19.6	0.713	34.8	79.2	NREL
<b>Dye sensitized</b> 	11.9	0.744	22.47	71.2	AIST
<b>Organic solar cells</b> 	10.7	0.872	17.75	68.9	AIST
<b>Multijunction devices</b> InGaP/GaAs/InGaAs 	37.9	3.065	14.27	86.7	AIST

Sandia: Sandia national laboratories (USA)

NREL: National Renewable Energy Laboratory (USA)

AIST: Japanese National Institute of Advanced Industrial Science and Technology

### 2.1.7 Structure of hybrid solar cells

The structure of a hybrid solar cell is presented in figure 2.7 and consisting of:

Photoanode: the anode is usually transparent substrate such as ITO glass. Its role is to allow the light to pass through and to collect the holes from the device. Usually the layer of conductive polymer PEDOT: PSS spin coated on ITO surface and serves as hole transporting layer and exciton blocker. Its role is matching the fermi level of the photoanode to HOMO energy level of the polymer for hole collection. Also it seals the active layer from oxygen and prevents the cathode material from diffusing into the active layer.

Photocathode: the cathode usually is aluminum and sometimes magnesium is used. The function of the cathode is to collect electrons from the device. This layer is deposited via thermal evaporation.

Photoactive layer: the photoactive layer is sandwiched between two electrodes and consisting of the donor conductive polymer like MEHPPV, PCDTBT or polythiophene derivatives and inorganic acceptor like CdSe, PbS, PbSe and CuInS<sub>2</sub> [23,30,51]. Also several metal oxides like TiO<sub>2</sub>, ZnO, Fe<sub>2</sub>O<sub>3</sub>, ZrO<sub>2</sub>, Nb<sub>2</sub>O<sub>5</sub>, Al<sub>2</sub>O<sub>3</sub>, and CeO<sub>2</sub> have been used in HSCs [42,51,52]. Metal oxides are cheap and non-toxic and they have good optoelectrical and magnetic properties, proper hardness, high thermal stability and good chemical resistance. Among them TiO<sub>2</sub> and ZnO can be considered as future candidates because they showed better performances than the other metal oxides. In comparison to TiO<sub>2</sub>, ZnO shows higher electron mobility and longer electron lifetimes which means lower charge recombination. Also ZnO can be obtained from a wide variety of easy and low-cost synthesis method in different nano-form with easy tuning of its morphology. Zinc oxide is a direct band gap semiconductor with the  $E_g = 3.37$  eV and large exciton binding energy of 60 meV [30,42,53,54,55].

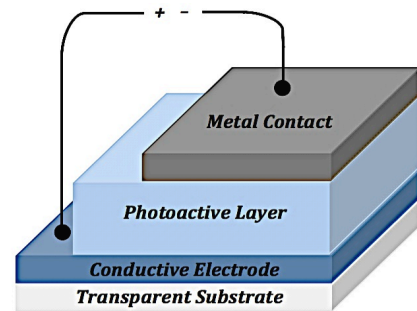


Fig 2.7 Schematic view of a hybrid solar cell structure consisting of four parts [17]

### 2.1.7.1 Fundamental of hybrid solar cells and device operation

Figure 2.8 shows the device operation of a hybrid solar. When a photon is absorbed by the active layer, the exciton is generated at the interface of donor/acceptor and once the exciton separated to free charges, the electron in donor material is transported to the cathode for charge collection and the hole produced in donor materials travels to anode to be collected [30,49, 56, 57].

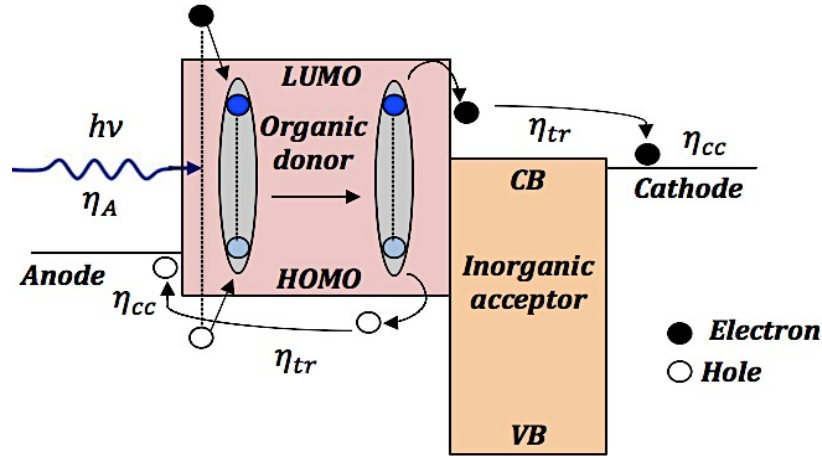


Fig 2.8 Schematic diagram of a hybrid solar cell operation, the efficiencies which are presented in equation (2.1) are shown in the diagram

As mentioned before, in hybrid solar cells, to overcome the exciton binding energy and separate the excitons to the free charge carriers, a force is required. For dissociation of the exciton which are formed in the donor material, the energy level offset of the lowest unoccupied molecular orbital (LUMO) of the donor and the conduction band edge of the acceptor materials is required. In figure 2.9 this energy offset is shown as  $\Delta E_{ES}$  which is the excited energy offset. For dissociation of the exciton which are formed in acceptor material, the energy level offset of the highest occupied molecular orbital (HOMO) of the donor and the valence band edge of the acceptor materials is required to be overcome. In figure 2.9 this energy offset is represented by  $\Delta E_{GS}$  which is the ground state energy offset. Since the excitonic dissociation due to these energy offsets occurs at the interface between the donor and the acceptor phase, the arrangement of the two materials in active layer is crucial for the successful operation of the device.

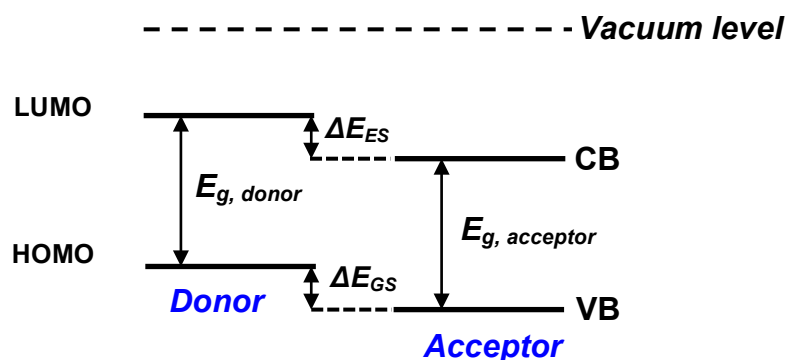


Fig 2.9 Energy level diagram of an organic– inorganic hybrid solar cell [30,42,58]

### 2.1.7.2 Ideal materials for hybrid solar cells

Donor material: to choose the donor material, electronic composition, hole mobility, the band gap and the HOMO and LUMO levels are important factor to be considered. In 2006 Scharber and his colleagues proposed the design rules for donor in bulk heterojunction solar cells when the acceptor is PCBM. They suggested for an ideal donor material the band gap must be less than 1.74 eV and the LUMO level less than -3.92 eV with respect to vacuum level. With this small band gap, large portion of solar spectrum can be utilized. Search for donor materials to enhance the performance of hybrid solar cells, led the researchers to poly (3-hexylthiophene). From around 2002, P3HT became the suitable polymer donor and regioregular P3HT shows environmental stability and higher hole mobility than other donors [59, 60]. Another excellent candidate for donor materials can be cyclipentadithiophene-based polymer which is a low band gap and high absorbing donor.  $J_{sc}$  for this polymer is much higher than that of the P3HT. More recent suitable donor polymer is PTB7 which has a band gap of 1.6 eV and exhibits good hole mobility and good solubility in organic solvents. It seems that these polymers are candidates for high performance of hybrid solar cells in the future [61,62].

Acceptor material: the electronic structure of the inorganic acceptor is an important factor to choose it. This electronic structure should be suitable for combining inorganic material with organic material. Xiang et al proposed that the ideal inorganic material should have a band-gap of 1.5 eV which is small enough to ensure good photon adsorption, so thus  $J_{sc}$ . The band gap of the acceptor material must be minimize to utilize more solar spectrum. Also these authors suggested the HOMO level of offset of 0.3 eV



which provides enough energy for exciton dissociation [63]. However, in addition of electronic structure, there are other physical requirements to be considered for choosing the acceptor material such as solubility in common solvent with the donor material, abundance, cost and tuning its nanomorphology [30].

### ***2.1.7.3 Photoactive layer nanomorphology***

The most important challenge for all type of solar cells, is achieving to the higher PCE values. In hybrid solar cells, the nanoscopic morphology of the composite plays a fundamental role for efficient performance of solar cells [30,47].

There are different morphology of active materials such as bi-layer, bulk heterojunction, nanoparticles dispersed heterojunction and vertically aligned heterojunction morphology which are shown in figure 2.10. In bi-layer morphology, two layers of donor polymer and inorganic acceptor are completely separated and in this case the recombination of exciton is so fast due to the long travel distance for electrons and holes to reach the terminals. In contrast in heterojunction morphology, two layers of materials are not separated but one phase is dispersed through other phase. This morphology provides less travel distance for the electrons and holes to reach the terminals compared to bi-layer morphology. The heterojunction morphology (figure 2.10) is defined as:

- Bulk heterojunction: in which the inorganic materials is randomly dispersed inside the organic matrix

- Nanoparticles dispersed: in which also there are dispersion of inorganic nanoparticles in polymeric phase as shown in figure 2.10. However in this case the diameter of nanoparticles is a key factor for efficiency of hybrid solar cells. As will be explained later, the quantum dot (diameter of almost 5 nm) nanoparticles have shown better cell performance.

- Vertically aligned morphology: in which the vertically aligned inorganic materials present in whole polymeric matrix. Researches of recent years have shown that using inorganic materials with the rod-like shape increased the efficiency of hybrid solar cells due to the formation of more charge transport pathways and their high surface-to-volume ratio [29,30,34,40,44,45,51,53, 55].

Figure 2.11 represents the pathways for electrons and holes in bi-layer and heterojunction morphologies. As it can be seen from the image, in the case of bi-layer, the length of donor phase (polymer) is more than the exciton diffusion length leading to the recombination of electrons and holes before arriving to the corresponding terminals. However in the case of bulk heterojunction, a much higher portion of donor phase is less than the distance of  $L_{ex}$  from the interface.

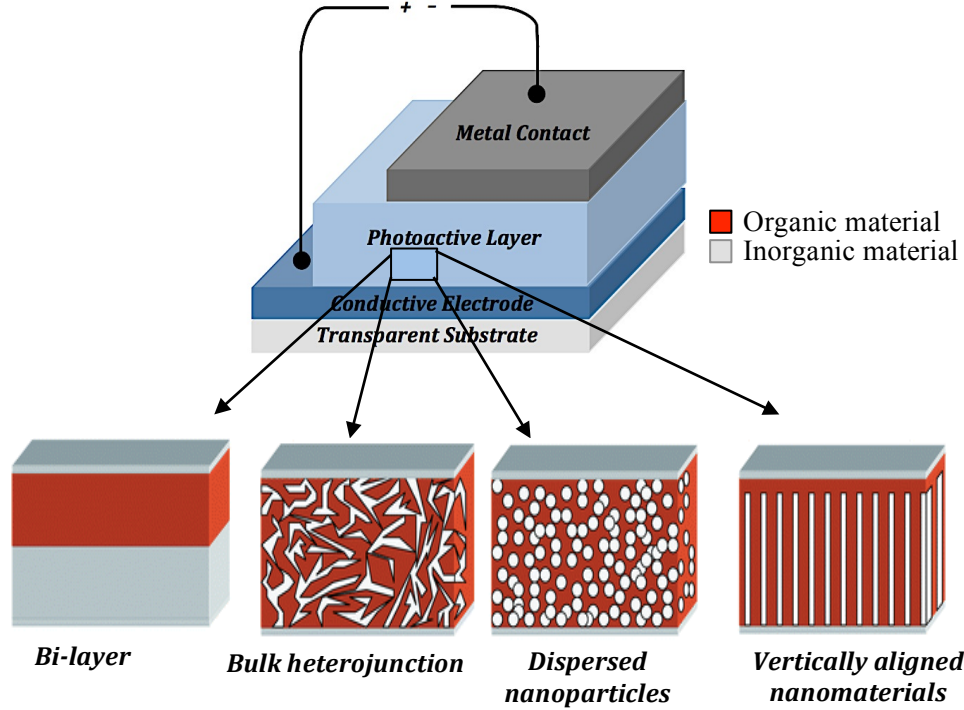


Fig 2.10 Schematic views of different types of active layer morphology in hybrid solar cells [40,53,64]

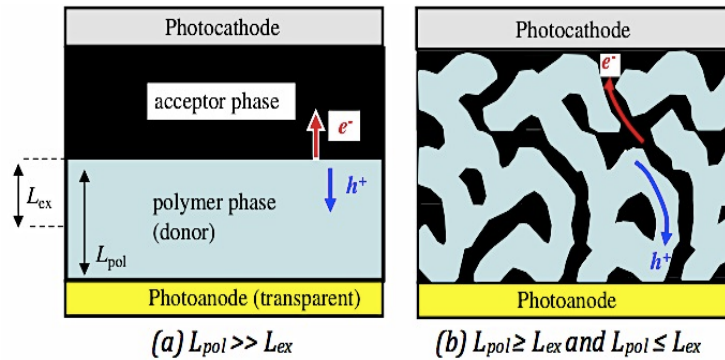
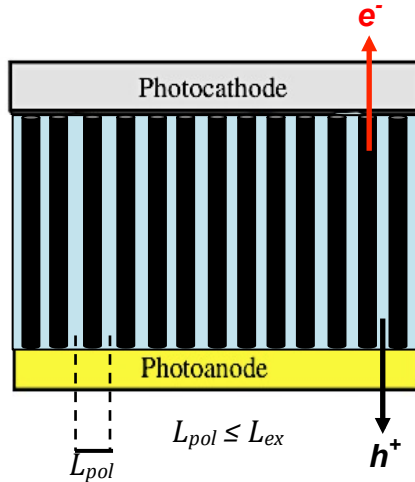


Fig 2.11 Schematic view of (a) bilayer and (b) bulk heterojunction morphology.  $e^-$ ,  $h^+$ ,  $L_{pol}$  and  $L_{ex}$  represent electrons, holes, the thickness of polymeric layer and the exciton diffusion length respectively [23,65,66]

According to different reports, the ideal morphology for when one material is dispersed through other materials, is rod-shape morphology [63,64,67]. Figure 2.12 shows how rod-shape materials provide more pathways for electrons and holes to arrive directly to the terminals with minimum recombination between them.



*Fig 2.12 Schematic view of charge transport in vertically aligned heterojunction morphology in which  $e^-$ ,  $h^+$ ,  $L_{pol}$  and  $L_{ex}$  represent electrons, holes, the thickness of polymeric layer and the exciton diffusion length respectively [65,66]*

Choosing the synthesis method to obtain vertically oriented nanorods (NRs) and controlling their distribution is important. Since one of current thesis objective is the synthesis of rod-shape active nanomaterials, in next section the synthesis method will be explained.

### ***2.1.8 Synthesis methods for fabrication of one- dimensional nanomaterials***

There are different methods to synthesize the metal oxide nanorods such as chemical and physical vapor deposition, hydrothermal process, solvothermal method, template growth, microwave assisted method, micelles, electrochemical deposition technique and etc. Vapor deposition techniques need to work in vacuum or at high temperature so they require sophisticated and expensive equipment. In contrast, solution methods consume lower energy for large-scale production.

Among these methods template-based synthesis is commonly and widely used method to obtain well-ordered freestanding nanowires, nanorods and nanotubes

[43,68,69]. The template method is a low cost, controllable and highly yields technique for synthesis of 1D nanomaterials [70, 71]. Templates are considered as a mold to fabricate micro and nano materials through their porous structure [72,73]. The diameter and length of the final product depend on the pore diameter and thickness of the template which are controlled by controlling the experimental conditions during the template fabrication. Up to now many materials like metals, metal oxides and conductive polymers have been synthesized by this method [74]. Since the template synthesis is the method using to obtain the materials in this project, in next section the brief information on template is introduced.

#### ***2.1.8.1 Template synthesis method***

Template method is classified to hard template and soft template. Usually organic materials like polymer networks, carbon nitrides and carbonaceous materials are example of soft templates and conversely porous solids such as silica, zeolites, and aluminum oxide are examples of hard templates [75,76]. In this project the materials were synthesized by hard template method from anodic aluminum oxide (AAO).

##### ***2.1.8.1.1 Anodic aluminum oxide (AAO) template***

Porous alumina has been studied for more than three decades. AAO template is suitable for application such as nanopatterning, fabrication of highly ordered one-dimensional nanostructures and nanocapacitor arrays in sensors, computing device, tool storage, magnetic and recording area. Also this template has been used as catalyst supports and adsorbents. This wide range of applications is due to its easy and low cost fabrication, good thermal and chemical stability and easy control of pore distribution, pore diameter, length and thickness of the template [70,77,78]. In addition also it is possible to synthesize nanowires, nanotubes and nanorods by using these templates.

AAO is described as a honeycomb structure consisting of hexagonal cell array with cylindrical nanoporous which are perpendicular to the template surface (figure 2.13) with pore diameter ranging from 10 nm to 200 nm, pore densities in the range of  $10^8 \text{ cm}^{-2}$  to

$10^{12} \text{ cm}^{-2}$  and the membrane thickness ranging from few tens of nanometers to more than several hundred micrometers [68, 69,79,80].

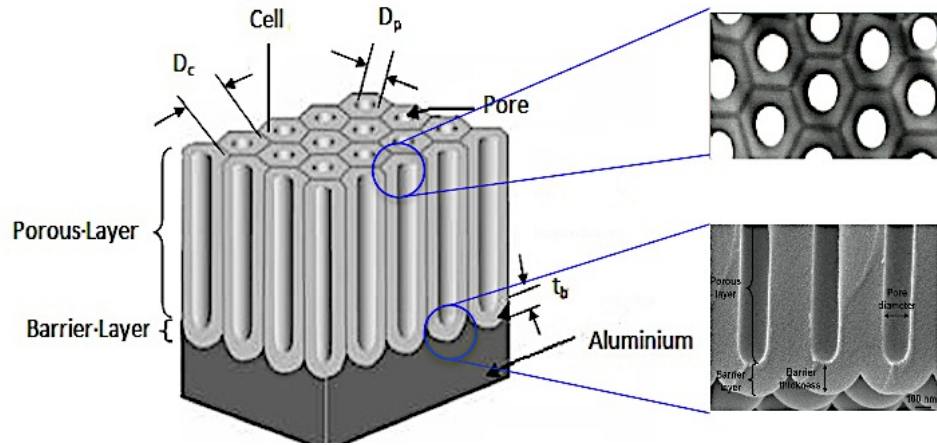


Fig 2.13 Schematic view of AAO template  $D_p$  is pore diameter,  $D_c$  is cell diameter and  $t_b$  is the thickness of barrier layer [79]

Since the method using in this project is electrochemical deposition using AAO template thus here the brief explanation of electrochemistry is needed.

### 2.1.9 Electrochemistry

Electrochemistry is the science concerning with the relation between electrical and chemical phenomena and is the measurements of electrical quantities such as current, voltage and conductivity and their relationship with chemical parameters like solution concentration, pH [81, 82]. If we consider a redox (reduction/oxidation) reaction in electrochemical cell (equation 2.6):



In which  $O$  is oxidized species,  $R$  is reduced species and  $n$  is the number of electron exchanged between  $O$  and  $R$ . The Nernst equation (equation 2.7) describes the concept of electrochemistry.

$$E = E^0 + \frac{RT}{nf} \ln \frac{[O]}{[R]} \quad (2.7)$$

Where  $E$  is potential between two electrodes,  $E^0$  is standard electrode potential,  $R$  is the gas constant  $8.3145 \text{ J.mol}^{-1}.\text{K}^{-1}$ ,  $T$  is the temperature (K), and  $f$  is faraday's constant

$96485.3 \text{ C}\cdot\text{mol}^{-1}$ ,  $[O]$  is the concentration of oxidized species and  $[R]$  is the concentration of reduced species [82].

In this manuscripts some terminology will be used and they are listed below:

- **Oxidation:** refers to the process in which a chemical species loses one or more electrons.
- **Reduction:** refers to the process in which a chemical species gains one or more electrons.
- **Electrochemical cell:** device that involves the presence of faradic currents as results of redox chemical reactions. There are two types of electrochemical cells: galvanic cells where spontaneously electrical energy produced and electrolytic cells that consume electrical energy and convert it to chemical energy.
- **Anode:** electrode where the oxidation takes place.
- **Cathode:** electrode where the reduction takes place.
- **Electrode:** an electrical conductor or semiconductor where the electron transfer occurs. (It can be anode or cathode).
- **Potential:** is the driving force for the redox reaction.
- **Current:** electron flow is the result of a redox reaction. Current measures the rate of the reaction (electrons per second).
- **Working electrode (WE):** the electrode where the redox processes under study occur. WEs are typically cathodes in electrochemical cell.
- **Reference electrode (RE):** electrode that can maintain a constant potential under exchanging experimental conditions. The WE is referred vs. the RE potential. REs are typically anodes in electrochemical cell.
- **Counter electrode (CE):** electrode that helps the current pass through the cell. The current travels between WE and CE.
- **Supporting electrolyte:** an ionic substance (typically salt) that presents as solution to ensure the charge carrier mobility in the cell. It does not undergo redox reaction. Sometimes supporting electrolyte simply called electrolyte.
- **Potentiostat:** an electronic instrument that measures and controls the voltage difference between working and reference electrodes and the current flow between working and counter electrodes.

Another important formula in electrochemistry is Faraday's law which correlated the total charge ( $Q$ ) passing through the cell with the amount of products ( $N$ ).

$$Q = nfN \quad (2.8)$$

Where  $Q$ ,  $n$ ,  $f$  and  $N$  are the total charge passing through the cell, the number of transferred electrons per 1 mole of product, faraday's constant and the amount of product respectively. One of the applications of faraday's law is to find the amount of substance deposited at an electrode [83].

Electrodeposition methods such as potentiostatic and galvanostatic methods allow us to synthesis a wide range of materials on the surface of an electrode and electrochemical analyses such as cyclic voltammetry and impedance spectroscopy help us to find out the behavior of the deposited materials.

#### ***2.1.9.1 Potentiostatic method***

In this method a constant voltage is applied between working and reference electrodes and the current between working electrode and counter electrode is measured with time. The thickness of the deposited film on the electrode surface depends on the deposition time and is calculated from faraday's law.

#### ***2.1.9.2 Galvanostatic method***

In this method a fixed current or charge is applied between the working and counter electrodes and the change in potential induced in the working electrode by the passage of current, is measured against the reference electrode.

#### ***2.1.9.3. Cyclic voltammetry (CV)***

Cyclic Voltammetry (CV) may is the most effective and versatile electroanalytical technique available for the mechanism study of redox systems. CV is often the first experiment performed in an electrochemical study. In CV the potential of WE linearly changes with time starting from a known potential, reaching to the final potential and again sweeping back from the final potential to the initial potential at fixed scan rate [84]. From the peaks of triangle-shape current –voltage curve, the reduction/oxidation potential

and current at peaks will be obtained. These values are useful to determine the reversibility and stability of the system, HOMO/LUMO energy levels and band gap.

#### ***2.1.9.4 Electrochemical Impedance spectroscopy (EIS)***

Electrochemical impedance spectroscopy is a technique which has been utilized over a century because of its ability to determine physical and electronic properties of electrochemical systems such as diffusion coefficient, electron transfer rate constant, adsorption mechanism, charge transfer resistance and capacitance. The technique is based upon complex mathematical transforms defining impedance as the complex ratio of the voltage and current in an AC circuit [85].

Since the materials which were synthesized in this project are a conductive polymer and metal oxide, thus in the following parts the brief information on these materials will be introduced.

#### ***2.1.10 Conductive polymers***

Polymers have been used as insulating materials for many ages because they can be shaped and processed more easily than for example metals. After the invention of the first conductive polymer i.e. polyacetylene in 1970s, these materials became the center of attention for researchers. Their wide range of electrical conductivity can be achieved with various doping levels, while they are maintaining mechanical flexibility and high thermal stability. These properties make them suitable for applications such as LED, supercapacitors, photovoltaic cells, electrochromic device, biosensors and so on [86]. In the structure of conductive polymers there are single and double bonds between carbon atoms.

The carbon atoms are in  $sp^2$ -hybridized state. Each of these  $sp^2$  carbon atoms has 3  $\sigma$  (sigma) bonds and a remaining  $p_z$  atomic orbital which exhibits  $\pi$ -overlap with the  $p_z$  atomic orbital of nearest neighbor. The chain of atoms with  $\pi$ -overlap of  $p_z$  atomic orbitals leads to the formation of  $\pi$ -states delocalized along the polymer chain where the flow of electrons leads to electrical conductivity of the polymer. However this is not quite



enough to conduct electricity since the electrons are still tightly linked to the polymeric chain. What needs to be done is to remove or to add some electrons to the chain. This process is called doping.

Removing electrons from the polymer backbone results in p-doping and adding electrons to the backbone results in n-doping. Doping can increase the conductivity of a plastic like material by a billion times up to the level matching that of the metallic materials. For example the conductivity of copper is a bit less than  $10^6$  S/cm and the conductivity of polyacetylene doped with  $AsF_5$  was reported more than  $10^5$  S/cm [87].

Most famous conductive polymers are polyacetylene, polyaniline, polypyrrole and polythiophene. Figure 2.14 shows the structures of these polymers and table 2.2 is the comparison between the properties of these polymers.

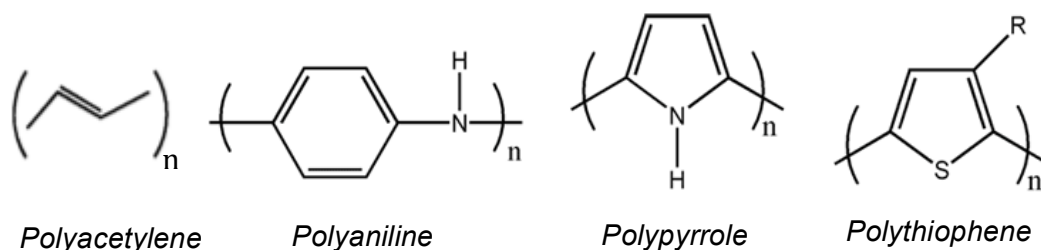


Fig 2.14 Schematic structures of conductive polymers [87]

Table 2.2 Properties comparison between conductive polymers [88]

<i>Polymer</i>	<i>Conductivity (S/cm)</i>	<i>Stability (doped state)</i>	<i>Processing possibilities</i>
Polyacetylene	$10^3 - 1.7 \times 10^5$	Poor	Limited (air-sensitive)
Polyaniline	0-200	Good	Good
Polypyrrole	$10^2 - 7.5 \times 10^3$	Good	Excellent
Polythiophene	$10 - 10^3$	Good	Good

Among the conductive polymers, although polythiophene and its derivatives have less solubility in water because of their higher crystallinity [89], they have attracted considerable attention due to their conductivity, high charge carrier mobility, longer

wavelength absorption and chemical stability in air and moisture in both neutral and doped states compared to the other conductive polymers [90, 91,92,93].

#### ***2.1.10.1 Poly (3-hexylthiophene)(P3HT)***

P3HT is one of polythiophene family with excellent properties such as hole mobility as high as  $0.1 \text{ cm}^2/\text{V.S}$  and optical absorption coefficient in the visible spectra in the order of  $10^5 \text{ cm}^{-1}$  [25,94]. The electrical properties of P3HT are highly dependent on the fabrication process. For example the reported values for the band gap energy of the P3HT are in the range of 1.7-2.1 eV, the electron affinity values are in the range of 3.2–3.5 eV and the doping concentrations are in the range of  $1 \times 10^{15}$  to  $1 \times 10^{17} \text{ cm}^{-3}$ . The highest value for conductivity of poly (3-hexylthiophene) was reported 1000 S/cm at room temperature [94, 95].

#### ***2.1.11 Metal oxides***

Wide band gap oxide semiconductors such as  $\text{TiO}_2$ ,  $\text{SnO}_2$ ,  $\text{CeO}_2$  and  $\text{ZnO}$  have been used as inorganic acceptors in hybrid solar cells because they are cheap and non-toxic and they have good thermal stability and optoelectrical properties. The major advantage possessed by these semiconductors is the ability to form vertically aligned oxide nanostructures. Currently, the most heavily investigated of these materials is  $\text{TiO}_2$ , as it has been extensively used in dye sensitized solar cells due to the high surface area of the semiconductor.

##### ***2.1.11.1 Zinc oxide***

The stability of hybrid solar cells using  $\text{ZnO}$  has also been investigated. In comparison to  $\text{TiO}_2$ , zinc oxide has higher electron mobility and longer electron lifetimes which results in lower charge recombination.

$\text{ZnO}$  is a direct band gap semiconductor with piezoelectric property, band gap of 3.3 eV and a large exciton binding energy of 60 meV. Zinc oxide can be synthesized from a wide variety of easy and low-cost methods in various nano forms and it is easy to tune its nanomorphology by changing the experimental conditions.

The next section is a review on the materials which have currently been investigated in hybrid solar cells. Their synthesis methods are explained and finally the summary of the major limitations and challenges in the field of hybrid solar cells will introduce.

## ***2.2 Literature review***

As a promising alternative to inorganic silicon solar cells, in 1991 Brian Oregan and Michael Grätzel invented a photochemical solar cell called dye-sensitized solar cells (DSSC) consisting of liquid electrolyte and TiO<sub>2</sub> films [96]. Up to now these cells have reached more than 10% of light conversion efficiency and being competitive with amorphous silicon solar cells. However these Grätzel cells have to be sealed to prevent the leakage of the electrolyte during the whole time operation. In 1995, Cao and his colleagues fabricated a photoelectrochemical cell with polymer gel electrolyte consisting a mixture of polyacrylonitrile, ethylene carbonate, propylene carbonate, acetonitrile and nanocrystalline TiO<sub>2</sub> electrode. This cell achieved the overall energy conversion efficiencies of 3-5%, V<sub>oc</sub> of 0.6V, I<sub>sc</sub> of 3 mA/cm<sup>2</sup> under 30 mW/cm<sup>2</sup> illumination. They mentioned that this quasi-solid-state cell exhibited the behavior similar to cells with liquid electrolyte, suggesting that ion transport in the polymer gel electrolyte does not influence the performance of these cells [97]. Two years later Haarer *et al* published a report on combining the advantages of organic and inorganic materials with the name of novel hybrid solar cells. This cell consisting of TiO<sub>2</sub> and propylene carbonate mixed with LiI and I<sub>2</sub> and Ruthenium complex as sensitizer. The TiO<sub>2</sub> screen printed on ITO and sintered at 450 °C to burn out the organic additives. Although they could successfully replace the volatile and unstable liquid electrolyte in Grätzel cell with a solid organic material, they just achieved the external quantum efficiency of 0.2% with this cell design [98]. After this report many research groups had focused seriously on replacement of one inorganic material with different type of polymers [99, 100,101, 102].

According to the review of Arici et al in 2004 on hybrid solar cells, there are three common methods to prepare organic/inorganic hybrid blend film; spin-coating from a solution, electrodeposition and layer-by-layer assembly [47]. In spin-coating method the nanocrystalline inorganic materials typically are synthesized by colloidal chemistry in

organic solutions such as alkyl thiol, amines, phosphines, or phosphine oxides and they are usually soluble in common organic solvents and can be mixed together with the conjugated polymers. However organic surfactant and ligands on the surface of inorganic materials tend to be insulated and decrease the electron transport between adjacent nanocrystallines.

Huynh *et al* synthesized the mixture of CdSe nanorods and P3HT. The nanorods of CdSe was not perpendicular on polymeric film but they were planar on polymer matrix. They selected P3HT because of its effective hole transport among other conductive polymers which can reach up to  $0.1 \text{ cm}^2/\text{V}\cdot\text{s}$  hole mobility. They synthesized the nanorods of CdSe separately and solved it in pyridine and chloroform mixture which is also suitable solvent for P3HT. Then the mixture of materials span coated on ITO.

They suggested that the length of nanorods have greater influenced on light adsorption by the material than their diameter by preparing different nanocrystalline of CdSe with diameter of 7nm/ length of 7nm, diameter of 7nm/ length of 30 nm, diameter of 7nm/ length of 60nm; it means the aspect ratio (AR: length/diameter) of 1 to 10. They suggested the rod-shape materials show better cell performance. It means by increasing the aspect ratio from 1 to 10, the charge transport and external quantum efficiency of cells increased by a factor of approximately 3. According to their report the best device which contained 7nm diameter and 60 nm length performed with a maximum EQE of 55% under  $0.1 \text{ mW}/\text{cm}^2$  illumination at 485 nm wavelength. For the rods shorter than 60 nm the electron transport is dominated by hopping. Also they investigated the surface chemistry between organic and inorganic materials by the influenced of the solvent which was used. They proposed the pyridine-chloroform mixture as suitable solvent for having the major interfaces and contacts between organic and inorganic materials [103]. A year later, the same authors, studied how it is possible to improve the efficiency of the cell consisting of CdSe (D: 7 nm –L: 60 nm) /P3HT materials by I-V characteristics using improved circuit model and modified Shockley equation considering series and shunt resistances. They reported that under illumination, the efficiency of photocurrent generations was dependent on the applied bias, unlike conventional inorganic semiconductors devices in which photocurrent is constant. They suggested that a theoretical understanding of the device physics of nanocrystal-polymer PV cells is

essential for improving this class of materials for using in high light intensity applications like solar cells [25].

After theoretical studies of device performance, this research group did extensive investigation on the role of the solvent in casting process of the O/I mixture. To create a high interfacial surface area, good dispersion of the inorganic nanoparticles within the polymer is essential. When in 2002 they mixed pyridine and chloroform as solvent, they did not mentioned the role and the volume portion of each solvent. One year later, with more studies they mentioned that with using suitable binary solvent, the PCE of cell was increase more than 50%. Suitable binary solvent with optimum volume portion of species will enhance the solubility of both organic and inorganic materials. The suggested the mixture of 4 vol.% to 12 vol.% of pyridine in chloroform as optimum volume ratio for this solvent. Pyridine is miscible in chloroform and pyridine-coated inorganic nanomaterials are more soluble in chloroform than their naked counterparts. Thus low amount of pyridine leads to insufficient solubility of inorganic materials resulting in phase separation. They also mentioned that the interaction of inorganic materials with polymer is mainly controlled by organic ligands adsorbed onto the surface of inorganic nanomaterials that makes their surface passive and unstable. The advantage of using pyridine is that this solvent does not bind to the inorganic nanomaterials and just covers their surface. Thus the low boiling point of pyridine (116 °C) allows the easily removal of this organic ligands from inorganic surface by heat treatment. With this modification in solvent their cell reached the EQE of 59% under 0.1 mW/cm<sup>2</sup> illumination at 450 nm which was higher than EQE of the same cell (54%) by using 1/2 volume ratio of pyridine to chloroform in 2002 [104].

The heat treatment on pyridine contained solvent also examined for PCPDTBT: CdSe and MEHPPV: CdSe composites materials and in both cases the better electron transport between NCs by reducing the insulating effects of the ligand and more contact between NCs and polymer was observed leading to improvement of  $J_{sc}$ ,  $\eta_{diss}$  and  $\eta_{tr}$  [105,106].

In addition to pyridine other solvent can work as capping organic ligands from the surface of inorganic materials. These solvents are tributylamine, oleic acid, pyridine, stearic acid, and butylamine and have been tested in P3HT:CdSE HPV cells. The highest

PCE (up to 1.8%) was obtained by using butylamine- capped CdSe NPs with a w/w mixing ratio of 12: 1 (CdSe: P3HT) and a post-treatment temperature of 110 °C [107,108].

In spin coating preparation of the hybrid films, beside the type of solvent and morphology of the inorganic materials, the synthesis method of nanocrystalline materials and spin speed also are important factors to be considered. High-temperature synthesis and toxicity of Cd-based materials motivated the researchers to find alternative materials. Transparent semiconducting metal oxides like TiO<sub>2</sub> and ZnO can also be used as the electron accepting material in combination with p-type donor conjugated polymers. These metal oxides are not toxic and are abundance. The synthesis of TiO<sub>2</sub> nanoparticle powders mainly occurs in water or alcohol based media. Transferring these nanoparticle powders into organic solvents regularly leads to aggregate formation and therefore a low miscibility with conjugated polymers. Besides crystallization of TiO<sub>2</sub> requires high temperature (more than 350 °C). These drawbacks of TiO<sub>2</sub>, make ZnO more suitable for hybrid solar cell application [38,39,48]. Janssen *et al* showed that ZnO crystallizes in lower temperature. The nanoparticles of ZnO synthesized from diethylzinc by sol-gel process showed lack of adsorption above 250 nm. After heating up the products just to 110 °C, the adsorption onset shifted to 375 nm. Janssen assembled a hybrid solar cell with these crystalline ZnO particles combined with MDMO-PPV conductive polymer and reached the 1.1% of PCE under AM1.5 standard condition [39]. Beek and Janssen investigated on effect of solvent, spin speed and morphology in ZnO:MDMO-PPV hybrid solar cells. ZnO nanoparticles were synthesized by hydrolysis and condensation of zinc acetate dihydrate by potassium hydroxide in methanol and ZnO nanorods were formed from the nanoparticles by heating a concentrated nanoparticle solution. The length of the rods tuned by varying the heating time. Nanorods prepared at 60 °C for 20 h had 60 nm in length. The device fabricated from spin casting of ZnO:MDMO-PPV mixture from chlorobenzene: methanol (95:5/v:v) solution. Higher fill factor of 0.62 was observed for rod-shape ZnO with volume portion of 26% in the mixture by spin speed of 1500 (rpm) from chlorobenzene solvent [109].

In 2006 Olson and his colleagues discussed on performance of ZnO nanofibers/poly (3-hexylthiophene) composite. Seed layer of ZnO deposited on ITO using zinc acetate solution in 2-methoxyethanol following by hydrothermally growth of ZnO nanofiber

from nucleation sites in zinc nitrate solution at 70 °C. Then the 200 nm of P3HT was spin coated on ZnO nanofibers. The device reached the  $V_{oc}$  of 0.44 V which was lower than expected from the effective band gap of the donor–acceptor couple, defined as the difference between the energies of the highest occupied molecular orbital (HOMO) of the donor and the lowest unoccupied molecular orbital (LUMO) of the acceptor. In the case of P3HT–ZnO, the effective band gap is approximately 0.9 eV. They reported that the reason for the lower measured  $V_{oc}$  may be because of the presence of mid-gap states on the surface of the ZnO that pin the Fermi level; or the electron mobility of the ZnO nanofibers could actually be too high, resulting in increased carrier recombination at the ZnO/P3HT interface and in a reduced  $V_{oc}$ . Also the spacing between the ZnO nanofibers as grown was on the order of 100 nm larger than the typical exciton diffusion length in P3HT. They improved the  $V_{oc}$  by incorporation of PCBM into P3HT. The  $V_{oc}$  reached the 0.475 V and the  $J_{sc}$  increased by the factor of 5 for a device ZnO nanofibers:P3HT compared to ZnO nanofibers: P3HT/PCBM.

This result demonstrates efficient electron transfer from PCBM to ZnO, as there were no direct pathways for electrons to be transferred from PCBM to the ITO without first being transferred to either the ZnO nucleation layer or the ZnO nanofibers. Also the P3HT/PCBM blend effectively reduced the distance between donor and acceptor materials resulted in higher EQE [110]. The same authors investigated the effect of solvent selection and polymer processing on photovoltaic performance of the hybrid solar cells consisting of ZnO nanofibers: P3HT. The device using dichlorobenzene showed better performance in comparison to the device using chloroform because of better contact between donor-acceptor materials. Also they annealed the active materials in two temperatures of 150 °C and 250 °C. For the device at 150 °C, PCE and FF of 0.25% 46.6 % were reported respectively and the device at 250 °C reached to PCE of 0.28% and FF of 48.4%. It was assumed that annealing caused the better infiltration of P3HT polymer chain into ZnO nanorods which led to improve of interfacial contact between organic and inorganic materials. One disadvantage of annealing is changing ordered polymer to more disordered polymer. This can be overcome by slow drying of polymer. In Olson experiments this phenomenon was observed from the loss of shoulders in absorbance spectrum of the device [111].

Beside solvent type, morphology and annealing of active materials, the solidification time of polymer has effect on contact between donor and acceptor.

Chen *et al* showed this effect of polymer solidification on hybrid cell contained ZnO nanorods: P3HT/PCBM. They prepared a sample with ZnO nanorods and P3HT solved in dichlorobenzene. After annealing at 250 °C, the sample was cooled down from 5 min to 54 min with different spin coating rate from 1000 to 400 rpm. All cell parameters were reported higher for the sample with drying time of 54 min. They suggested that the slow drying gives polymer longer time to self-organize and reaches the higher order. The absorption spectra of the samples showed larger absorption for slow dried sample. So lengthening the cooling rate causes thicker active layer which leads to better light harvesting [46].

In previous paragraphs, the synthesis of rod-shape inorganic materials by different research groups was explained. Kim and Cho synthesized conductive polymer nanorods by using AAO template for organic solar cells application. AAO template was fabricated by anodic oxidation of an aluminum sheet in 0.3 M oxalic acid at 40V. P3HT in chloroform was spin-coated onto PEDOT/PSS-coated ITO glass. The AAO template was next placed on top of the film and the combination was heated to 250 °C under vacuum, well above the melting temperature of P3HT. The molten P3HT chains readily entered the nanopores by capillary action. By this method they obtained nanorods of P3HT with 50 nm of diameter and 150 nm of length. The P3HT nanorods showed 20 times more hole mobility compared to P3HT continuous films as mentioned also by McGehee and coworkers [112]. For their organic cells the efficiency of P3HT nanorods/C<sub>60</sub> was a factor of 6.6 higher than the efficiency of planar P3HT/C<sub>60</sub> (0.17% versus 1.12%)[113].

In 2012, Russell and his coworkers synthesized the nanopillars of P3HT via AAO template by new approach. A 2wt % P3HT chlorobenzene solution was spin-coated on ITO glass to form a polymeric layer on ITO. The ITO faced down on surface of AAO and sandwiched between two glass slides and clamped together putting in the furnace and heating up to 230 °C for 10 min. The P3HT on ITO melted and filled the channels of AAO template. They obtained P3HT nanopillars of 30 nm and 50 nm in diameters by using two different templates. The layer of C<sub>60</sub> span coated on the pillars and the cell



efficiencies were calculated. The pillars with 30 nm of diameter showed PCE of 2.4% while the pillars with 50 nm of diameters reached the 2.0% of efficiency [114].

As mentioned previously, the vertically aligned morphology is a promising and ideal morphology in hybrid solar cells which cannot be reached by spin coating of both materials from the same solution on the substrate and it is difficult to control the composite morphology. Although the rods of materials can be obtained in polymeric matrix, but these rods are lean on the matrix and are not perpendicular to the polymeric film.

Other method of hybrid film preparation is via electrochemistry combined with template method which results in synthesis of vertically-aligned nanomaterials. Films of nanocrystalline inorganic materials can be deposited by electrochemical method from non-aqueous solution such as DMSO containing solutions and metal salts. Second step is electropolymerization of conductive polymers onto inorganic layer. Many inorganic materials for photovoltaic application were synthesized by this method such as CdS, CdTe, CuInS<sub>2</sub>, CuInSe<sub>2</sub>, TiO<sub>2</sub>, ZnO, ZnSe, conductive polymers and etc [115,116,117,118,119,120,121,122].

In 2005, Kim *et al* fabricated a hybrid solar cell consisting of CdTe nanorods and poly (3-octylthiophene) (P3OT). The power conversion efficiency of cell was 1.06% which was higher than this value without the rods (PCE of 0.0006%). They used AAO template as working electrode with diameter about 200 nm, thickness of 30 μm and pore density of  $5 \times 10^8 / \text{cm}^2$ . The cathodic deposition of CdTe was performed from an aqueous solution and then the P3OT was spin coated on nanorods. They reported the resistivity and electron density of rods by the Hall effect which were  $2 \times 10^6 \Omega \cdot \text{cm}$  and  $1.3 \times 10^{10} \text{cm}^{-3}$  respectively which showed fast electron transport in O/I blend by this morphology. Other solar cell parameters that they reported were the short-circuit current density, open-circuit voltage and fill factor of 3.12 mA / cm<sup>2</sup>, 0.714 V and 47.7% respectively [123].

In 2010, Zhang's research group electrodeposited ZnO on transparent reduced graphene oxide electrode (rGO) to fabricate ZnO nanorods. The aim of their work was to investigate the substrate surface chemistry on cell performance. They prepared the rGO electrodes with different thickness of 5, 9 and 13 nm by transferring the hydrazine vapor reduced graphene oxide (GO) film onto a 3-amino-propyl-triethoxysilane (APTES)-

coated quartz. Electrodeposition of ZnO nanorods carried out at -0.98 V and 80 °C from ZnCl<sub>2</sub> and KCl solution on rGO.

They observed that the obtained electrochemically deposited ZnO varies from a random porous structure to the highly c-axis oriented nanorod structure, as the thickness of rGO films increases. The thinner rGO film has a lower current flow and the charge density on electrodes is small, leading to a lower concentration of hydroxide ions, which are generated through electrochemical reduction of oxygen. They assembled two cells with quartz/rGO(13nm)/ZnO NRs/P3HT/PEDOT:PSS/Au and quartz/rGO (13nm)annealed /ZnO NRs/P3HT/PEDOT:PSS/Au with the efficiencies of 0.14% and 0.31% respectively. Since the work function of electrodes plays an important role in enhancing the performance of solar cells, they suggested that the decrease of work function after thermal annealing has two advantages: 1) an increase in  $V_{oc}$  to favor more efficient electron-hole separation and 2) a better match between the Fermi level of rGO and  $E_c$  of ZnO to improve the efficiency of electron collection. Compared to the other reports on ZnO/P3HT hybrid solar cells with carbon nanotubes (CNTs) or ITO as electrodes, their device showed less PCE and this might be due to more defects, lower conductivity, and relatively poor optical transmittance of rGO films, as compared to CNTs and ITO [124].

In electrochemical method, control the parameters like substrate type, voltage, electrolyte, current density, temperature and deposition time are critical to obtain the suitable final product with less structural defects.

Lin *et al* investigated the effect of temperature and deposition time in synthesis of ZnO nanorods via electrochemical deposition method on ITO substrate at -0.9 V from 0.005 M Zn (NO<sub>3</sub>)<sub>2</sub>. The experiments were done at two growth temperatures of 60 and 80 °C for different deposition time. They reported the longer ZnO nanorods by increase the deposition time, whereas the deposition time had minor influence on diameter of rods. It was observed that the temperature increase had effect on faster deposition rate. They obtained ZnO nanorods with 260, 360 and 740 nm heights at 80 °C and 99, 120 and 210 nm at 60 °C during 5,10 and 20 minutes of deposition respectively. In both cases the rods diameter was  $102 \pm 12$  nm [125].

Also there are several reports on electrochemical synthesis of organic materials. Some conductive polymeric films like polypyrrole, polythiophene, thiophene-derivatives,

polyacetylene, polyaniline have been synthesized by various research groups from different methods of electropolymerization such as potentiostatic, galvanostatic and cyclic voltammetry [126, 127, 128, 129, 130, 131, 132, 133, 134]. In 1992, Roncali wrote an extensive report on electrochemical synthesis of polythiophene. This report was on the mechanism of electropolymerization, different synthesis route such as cathodic and anodic routes, monomer concentration, type of organic solvent, type of electrolyte, electrical conditions like voltage, current or scan rate and the obtained values for conductivity by changing the experimental conditions [135].

For the first time, Charles Martin reported the electropolymerization of conductive polymers into the AAO channels for fabrication of wires, rods and tubes of conductive polymers. He fabricated the fibers of polypyrrole from the pyrrole-contained solution [136]. Later he synthesized the fibers of poly(3-methylthiophene) from the solution of 0.6M of 3-methylthiophene and  $\text{Fe}(\text{ClO}_4)_3$  in acetonitrile as electrolyte [137]. After the report of Martin, many groups have synthesized the polymer nanowire, nanorods and nanotube by electropolymerization and template methods. In this method, the AAO template as working electrode is placed in 3-electrode cell containing the solution of monomer and supporting electrolyte. The behaviors of polymers like oxidation and reduction peak voltages and currents can be obtained from I-V curve of cyclic voltammetry. Common electrolytes are  $\text{Bu}_4\text{NBF}_4$  [138],  $\text{BF}_4^-$  [139], TBAP [140],  $\text{LiClO}_4$  [141],  $\text{Et}_4\text{NBF}_4$  [142] and  $\text{TBAFP}_6$  [143].

As is understood from the previous reports on hybrid solar cells, the efficiency of these cells is still too low when industrial applications are targeted. One of the main reasons of low efficiency is because of the contact between organic and inorganic materials. The selection of these materials and the manner of contact between them are critical issues to gain better optoelectrical properties as well as mechanical properties. In 2005, Mammeri and Sanchez reported an extensive review on mechanical properties of hybrid inorganic-organic materials [144]. They mentioned that by increasing the interfacial interactions between both components via the formation of hydrogen bonds or covalent bond, by mixing various polymers or the adequate choice of the inorganic precursor, homogeneously dispersed organic-inorganic nanocomposites can be obtained.

The properties of O/I are dependent on their micro- and nanostructures and the nature of interface between them.

Also, other important issue is the interface between the hybrid film and the substrate since the strong adhesion can ensure the less delamination of the film. The table 2.3 shows the efficiencies of up-to-date hybrid solar cells with different organic and inorganic materials and morphologies.

*Table 2.3 A summarized list of selected hybrid materials and parameters of hybrid solar cells*

Acceptor	Structure	Donor	J <sub>sc</sub> (mA/cm <sup>2</sup> )	V <sub>oc</sub> (V)	FF	PCE (%)	Illumination (mW/cm <sup>2</sup> )	Year	Ref
CdS	QD	P3HT	10.9	1.1	0.35	4.1	100	2011	[145]
CdS	NW	P3HT	5.26	0.6	0.54	1.73	-	2009	[146]
CdS	NR	MEH-PPV	2.96	0.85	0.466	1.17	100	2007	[147]
CdSe	NR:QD	PCPDTBT	13.86	0.48	0.51	3.64	100	2012	[148]
CdSe	NP	PCPDTBT	9.2	0.78	0.49	3.5	100	2012	[149]
CdSe	NR	P3HT	9.7	0.553	0.494	2.65	100	2010	[150]
CdSe	Tetrapod	OC <sub>1</sub> C <sub>10</sub> -PPV	6.42	0.76	0.44	2.4	89.9	2005	[151]
CdSe	Tetrapod	PCPDTBT	10.1	0.678	0.51	3.19	100	2010	[105]
CdSe	Tetrapod	PDTTPD	7.26	0.88	0.46	2.9	100	2011	[152]
CdSe	QD	PCPDTBT	8.3	0.591	0.56	2.7	100	2011	[61]
CdSe	QD	P3HT	5.5	0.78	0.47	2	100	2011	[108]
CdSe	NC	P3HT	5.62	0.8	0.43	1.9	100	2012	[153]
CdSe	NS	P3HT	6.5	0.7	0.42	1.9	100	2011	[154]
CdTe	QD	PPV	10.7	0.5	0.4	2.14	100	2011	[155]
CdTe	Tetrapod	PSBTBT-NH <sub>2</sub>	7.23	0.79	0.56	3.2	100	2011	[156]
CdTe	NR	P3OT	3.12	0.714	0.477	1.06	100	2005	[123]
CdTe	NC	PNV	6.14	0.44	0.32	0.86	100	2011	[157]
CuInSe <sub>2</sub>	QD	P3HT	8.07	0.335	0.527	1.425	100	2011	[158]
PbS	NC	MEH-PPV	0.13	1	0.28	0.7	5	2005	[159]
PbS	QD	P3HT	1	0.42	0.39	0.16	-	2011	[160]
Si	QD	P3HT	3.8	0.8	0.47	1.47	100	2010	[161]
Si	NW	P3HT	11.61	0.425	0.39	1.93	100	2009	[162]
Si	NW	PEDOT:PSS	24.24	0.532	0.651	8.4	100	2012	[163]
ZnO	NP	MDMO:PPV	2.67	0.828	0.399	0.88	100	2011	[164]
ZnO	NP	P3HbpT	2.1	0.83	0.35	0.61	100	2012	[165]
ZnO	NW	P3HT	0.32	0.4	0.28	0.036	100	2010	[166]
ZnO	NR	P3HT	7.46	0.60	0.535	2.4	-	2012	[114]
ZnS	NP	P3HT	0.00081	1.2	0.25	0.2	-	2009	[167]
TiO <sub>2</sub>	NT	P3HT	1.8	0.62	0.58	0.5	100	2011	[168]
TiO <sub>2</sub>	NR	P3HT	4.33	0.78	0.65	2.2	100	2009	[169]
TiO <sub>2</sub>	Porous	P3HT	4.71	0.87	0.68	2.81	100	2011	[170]

There are some reports on hybrid solar cells to improve their performance by using other morphologies or techniques. For example in 2007 Alivisatos and his coworkers mentioned the synthetic method for the creation of 3D dendritic inorganic nanocrystals with controlled size and branching structure. These hyperbranched nanocrystals allow the creation of hybrid solar cells, whose architecture affords advantages over conventional approaches. They suggested that the branching structure of the nanocrystals, controls the dispersion of the inorganic phase in the polymer matrix. Thus ensuring a large, distributed surface area for charge separation. Moreover, each hyperbranched particle spans the entire device thickness and thus contains a built-in percolation pathway for transport of electrons to the anode. These composites based on these 3D particles can therefore be spin cast from a single solvent and this prevents the phase separation between inorganic and organic materials. They reported  $V_{oc}$  and PCE of 0.6 V and 2.18% under Am1.5G for a blend of hyperbranched of CdSe and P3HT [54].

Another example is tuning the energy levels of hybrid films by inserting other organic material. Kutsenco *et al* synthesized the CdSe (both rod and dot-like):P3MT composite and dispersed it in the P3HT matrix.

They mentioned that the effect of the P3MT layer is to moderate charge and energy transfer between CdSe and P3HT in the ternary nanocomposite system. They shown that excitation of the low-molecular P3MT resulted in energy transfer to both CdSe and P3HT components, and it also served as a barrier against recombination of electrons and holes separated at CdSe and P3HT, respectively. The open circuit voltage of ternary-phase system was more than just CdSe: P3HT composite [57].

In 2012, the researches of Stanford university fabricated Si nanocone: PEDOT:PSS hybrid solar cell. With this nanocone morphology reaching the 35.6 mA/cm<sup>2</sup>, 0.51 V, 41.3% and 7.54% of current density, open circuit voltage, fill factor and power conversion efficiency respectively which were higher than these parameters in Si (planar): PEDOT:PSS composite with  $J_{sc}$  of 22.5 mA/cm<sup>2</sup>,  $V_{oc}$  of 0.55 V, FF of 48% and PCE of 5.92%. The synthesis method of Si nanocone was reactive-ion etching (RIE) [171].

Other examples of efforts for improve the performance of hybrid solar cells is hybrid solar cell in tandem architecture proposed by Trimmel in 2013. This structure

consisting of Glass/ITO/PEDOT:PSS/PSiF:DBT-CIS/PEDOT:PSS/PTB7:PBCM/Al (electrode) and reached the  $V_{oc}=0.9$  V,  $J_{sc}= 8.04$  mA/cm<sup>2</sup>, FF= 0.57 and PCE= 4.1% [172].

The last but not the least example is the work of Wei and He on Si/PEDOT:PSS hybrid solar cell. They increased the junction area by new morphology consisting of micropylramids (MPs) and nanowires (NWs) of silicon. The MP arrays were fabricated on Si substrates via an electrodeless chemical etching process. After the formation of MP arrays, the Si wafer was immersed into an etchant composed of hydrofluoric acid and hydrogen peroxide mixtures for an anisotropic wet-chemical etching process. Etching the micropylramids caused the formation of Si nanowires. The lengths of the Si NWs were controlled by the etching time. Lengths of 30, 185, 234, 357, and 602 nm correspond to the etching time of 2, 3, 5, 6, and 9 min were obtained. Hybrid cells with hierarchical Si surfaces consisting of micropylramids and nanowires exhibited open-circuit voltage of 0.52 V, short-circuit current density of 34.46 mA·cm<sup>2</sup>, fill factor of 64.06% and PCE of 11.48%, which was the highest PCE among all the reported Si/organic hybrid cells [173].

In previous pages the two main challenges of hybrid solar cells i.e. morphology of active materials and contact between them were discussed and some procedure to resolve these problems were explained but Other challenge is the degradation of organic materials which results in low life cycles of hybrid solar cells compared to other types of cell. The degradation is caused by the diffusion of oxygen and water into the devices.

Krebs *et al* has recently reported the long-term stability of a HSC made of ZnO nanoparticles and the polymer poly (3-carboxy-dithiophene) (P3CT). The author modified the planar HSC configuration of ITO/ZnO(dense layer):MEH-PPV/Ag applying ZnO as dense thin films, to ITO/ZnO(nanoparticles):P3CT/PEDOT:PSS/Ag using ZnO nanoparticles. The lifetime of the first configuration was limited to only a few minutes (hours), the new configuration shows a lifetime of up to 500 h, in both cases without the use of a UV filter [174]. This higher stability of the polymer is due to the removing of carboxylic acid groups which is more stable towards oxygen. Also the time required for the solar cell to exchange oxygen and degrade the polymer could also be related to the total active surface area of the oxide. If the latter is true, in a HSC made of

dense thin films of ZnO (about 30 nm thickness) the exchange of oxygen and the stabilization in the dark would take place in only a couple of hours while in a nanostructured ZnO thin film made of nanoparticles the stabilization period could take several days, even months [42]. Other way to overcome the polymer instability is physically separation of the electron and hole transporting components.

Wang *et al* carried out stability analyses of a cell consisting of Al/P3HT:ZnO:PDI/PEDOT/ITO where ZnO was used in the form of nanoparticles and the dye PDI was used to improve photovoltaic performance. They reported that dye-treated device showed longer lifetime, better charge transfer yield and slower half-life [31].

Nowadays the stability of hybrid solar cell improved thanks to many studies in this field.

According to the reports of Azzopardi and Mutale in 2010 on life cycles of different type of solar cells, the life cycle of organic solar cells and hybrid solar cells in their studies assumed to be 25 years which is a bit less than the lifetime of mono-crystalline cell of 30 years and is more than some thin-film solar cells (table 2.4) [175]. However with good advantage of hybrid materials like flexibility of device and combination of both organic and inorganic advantages and also with the recent approaches to improve their performance it is worth it to investigate and do research on these kind of cells.

*Table 2.4 Comparable assumed characteristics for future hybrid solar cells [175]*

<b>Solar cells type</b>	<b>PCE (%)</b>	<b>Lifetime (year)</b>
Hybrid QD-based	10	25 (assumed)
Organic cell	5	25 (assumed)
Mono-crystalline	13.2	30
Thin-film (CIS)	11	20
Thin-film (CdTe)	9	20

An example of recent investigation is a report of University of London with the name of “*Solar cells get down with pop music*” published in PhysicsWorld.com in November 2013, focusing on piezoelectric properties of ZnO (mentioned in part 2.11.1).

In this work they suggested an interesting hypothesis that in the cell consisting of ZnO nanorods and P3HT, how the piezoelectric effect can help in PV generation and a 50% improvement of cell performance. Their experiments suggested that the improved performance was down to the zinc oxide nanorods converting the kinetic energy of the vibrations into electrical energy. This electric energy interacted with the excited charge carriers formed by sunlight in the PV polymer, and this interaction prolonged their lifetime and reduces the rate at which they are lost to recombination. According to the researchers, pop and rock music gets the cells going more than classical music, but they suggest that any noise with a broad range of frequencies will produce similar effects. The discovery might be exploited by placing the devices on top of buses, air-conditioning units and in other noisy spots [176].

From the literature review it could be concluded that the poly (3-hexylthiophene) as organic material and zinc oxide as inorganic material are the promising materials for hybrid solar cells. The challenge is mixing these two materials together to have the best interfacial contacts between them and charge carrier mobility by one-dimensional morphology. It is assumed that the template assisted electrochemical deposition will result in better infiltration and connection between organic and inorganic materials as well as obtaining the rod morphology of active materials. This assumption led to propose the following hypothesis.

### ***Hypothesis***

*“The synthesis of zinc oxide nanorods by conductive polymeric template will allow fabricating the vertically aligned morphology of active materials and the hybrid film can be a candidate in hybrid solar cell applications”.*

### ***General Objectives***

*“Synthesis of zinc oxide nanorods by template assisted method from conductive polymer with the application of the hybrid film in hybrid solar cells”.*



### *Specific objectives*

- ❖ Fabrication of anodic aluminum oxide (AAO) template and finding the optimum conditions through an anodization process in an electrolytical cell. Changing the experimental conditions resulting in control the pore size and the thickness of the template.
- ❖ P3HT synthesis and characterization from two methods of electrochemical and chemical polymerizations in which the AAO template which is obtained from the first stage, will be used as substrate to deposit the polymer into its pores.
- ❖ Synthesis of zinc oxide nanorods by the polymeric template which is obtained from the previous step and finding out the optimum parameters such as diameter and length of rods.
- ❖ Characterization of active layer consisting of ZnO nanorods and polymeric phase such as structural and optical analysis by methods such as: SEM and UV-vis.
- ❖ Hybrid material analysis by different methods like: absorption (Uv-vis), photocurrent measurements and photoluminescence.

*Chapter 3*  
*Methodology*  
*(Synthesis and characterization methods)*

### 3.METHODS, MATERIALS AND EXPERIMENTAL CONDITIONS

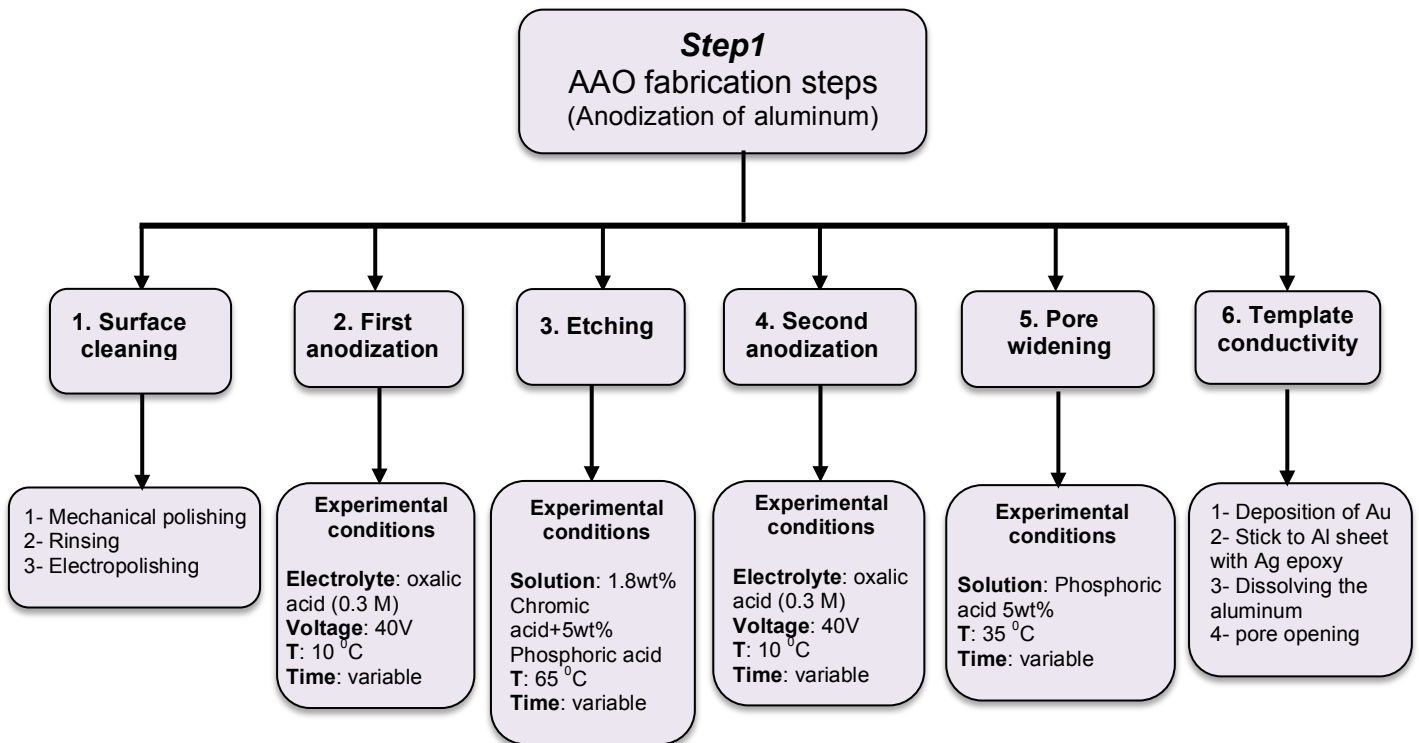
This chapter explains the experimental and characterization methods, materials and experimental conditions that have been used in this PhD thesis. First of all, the method for template fabrication is described. Then, the chemical and electrochemical synthesis of polymer are presented. At the end, the synthesis method of zinc oxide will be described.

#### 3.1 First step: anodic aluminum oxide (AAO) template fabrication processes

Fabrication of AAO template consists of 5 steps:

- 1- Surface cleaning of pure aluminum
- 2- First anodization
- 3- Etching
- 4- Second anodization
- 5- Pore widening

The flowchart below shows this procedure.



Flowchart 1. Fabrication steps for anodic aluminum oxide template

AAO fabrication is an electrochemical process which takes place in an electrochemical cell consisting of electrolyte and two electrodes connected to the DC power source.

The electrodes are pure aluminum foil which will be oxidized and converted into aluminum oxide during the process. This electrode serves as anode. Another electrode can be carbon, nickel, palladium, platinum, stainless steel or any electron conductor, which is inert to electrolyte and serves as cathode. When the current passing through the cell, the electrochemical reactions take place, the aluminum metal reacts with the acidic electrolyte and the oxide layer (anodic film) is formed on its surface. To do this process special design of cell was necessary.

### ***3.1.1 Setup and cell design***

The structure of the cell is shown in figure 3.1. The sample (pure Al foil) was placed at the bottom of the cell. With this cell design there is no need to connect the aluminum by a wire to the DC terminal. Because of the presence of high temperature and voltage during the anodization, the wire will be corroded so fast and just the platinum wire can resist in these experimental conditions since it does not react with the acid. However the platinum wire is expensive. The cell body is made of poly vinyl chloride (PVC) cylinder which has proper resistance to acidic solution and high temperature. At the bottom of the cell there is a hole where the sample is placed and will be in contact with the electrolyte from one face. The sample was fixed with a gasket and from the other face was connected to the sheet of aluminum and screwed with the pins to the aluminum plate. The aluminum sheet was connected to the positive terminal of DC power with alligator to pass the electricity to the sample (anode).

During the anodization, the electrolyte was agitated vigorously by an agitator which was fixed above the cell by the laboratory clamp. This provides uniform temperature distribution through the electrolyte and prevents the accumulation of ions on the surface of the sample. To reduce the temperature, peltier was connected to the bottom of cell. Peltier function is based on the thermoelectric effect which is a direct conversion of temperature difference to the electric voltage and vice versa.

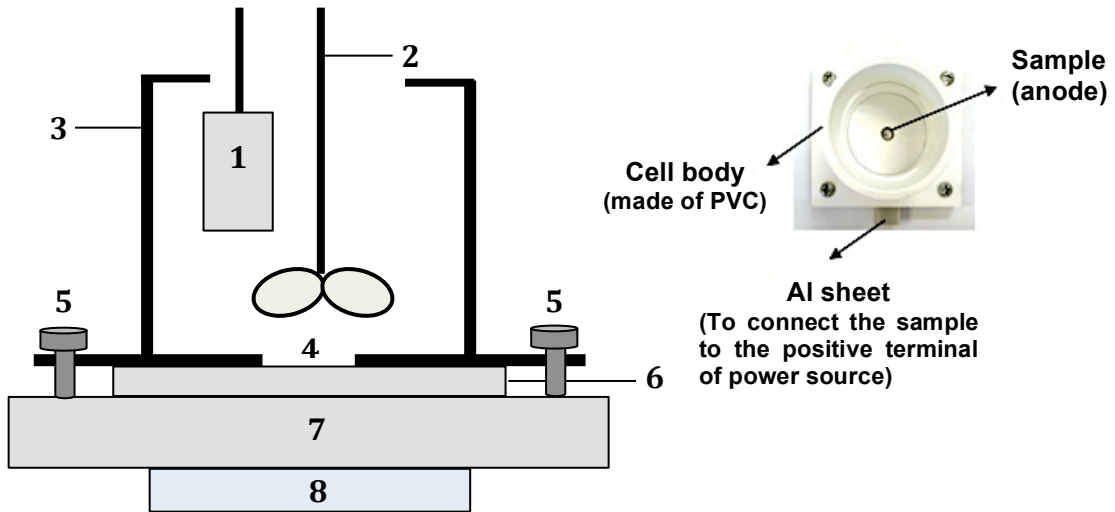


Fig 3.1 Left side: schematic side view of the cell: (1) aluminum sheet (cathode), (2) agitator, (3) cell body made of PVC, (4) gasket at the bottom of the cell to place the sample (pure aluminum, anode), (5) pins to fixed the cell body to aluminum plate to prevent the leakage of the electrolyte, (6) aluminum sheet to connect the sample to the power source, (7) aluminum plate to fixe whole structure and (8) peltier. Right side: up view of the cell

This phenomenon can be useful when it is necessary to transfer heat from one medium to another on a small scale. The Peltier consists of two semiconductors of n and p type sandwiched between two thermally conductive ceramic plates which is shown in figure 3.2.

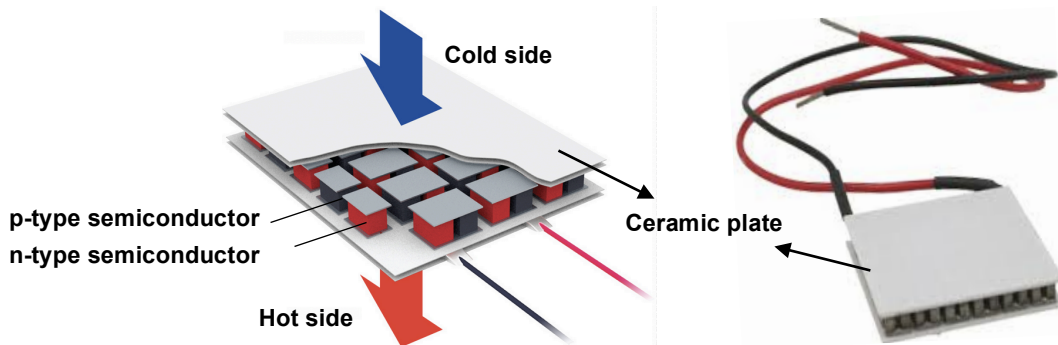
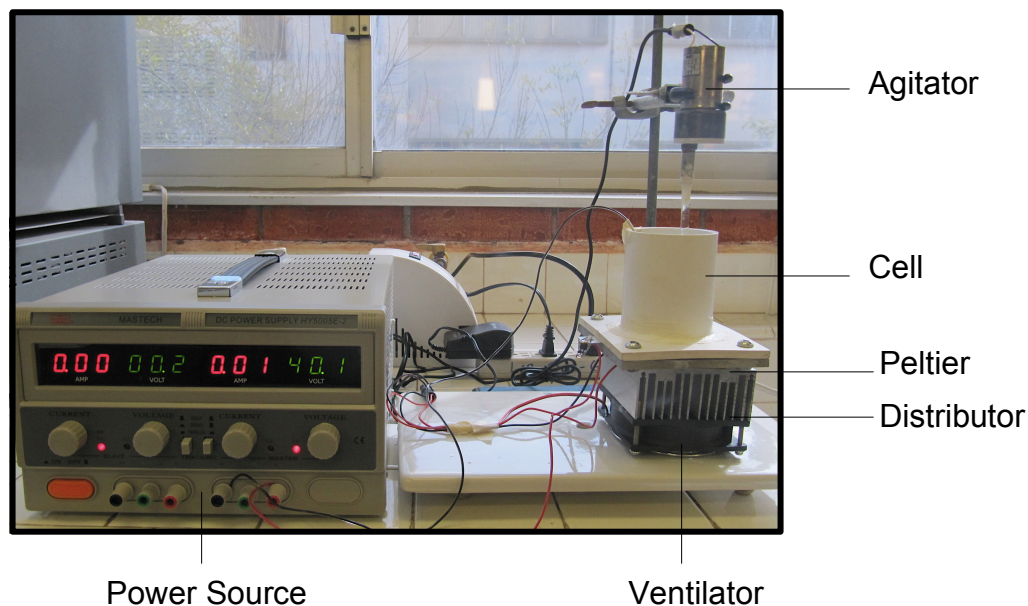


Fig 3.2 Structure of the peltier on the left side and peltier itself on the right side

When the peltier is connected to the power supply, the applied voltage creates a temperature difference between two plates that stems from the charge mobility from one semiconductor to another one. With this temperature gradient one plate becomes cool

while the other one is hot. In our case the cold side of peltier was in contact with the bottom of the cell to cool down the temperature of the sample and the hot side was in contact with a ventilator to remove the heat. Figure 3.3 shows the entire setup that was used to fabricate the AAO template.



*Fig 3.3 Schematic view of entire set up for anodization process consisting of agitator, cell, peltier, distributor, ventilator and power source*

### ***3.1.2 Surface cleaning or Pre-treatment on pure aluminum surface***

The quality of the template depends on the aluminum surface. To obtain the well-ordered pores with the uniform distribution, a clean and uniform surface of aluminum is necessary which was obtained by pre-treatment on the aluminum metal surface before starting the template fabrication. Pretreatments consisting of:

- *Rinsing* the piece of aluminum foil in water and in ultrasonic bath of acetone for 10 minutes to clean the surface from the dust and dirt.
- *Mechanical polishing* by using the polishing cream to remove the surface grease and small surface scratches following by washing the aluminum piece.
- *Electropolishing* to have a smooth, clean and shiny surface free of scratches.

### 3.1.2.1 Pre-treatments: Mechanical polishing and Electropolishing

Mechanical polishing was done on the surface of aluminum by polishing cream in order to obtain clean and more smooth surface than the original surface. The AFM images of original surface and the surface after mechanical polishing will be shown in the next chapter.

Electrochemical polishing was done in the cell shown in figure 3.4. The cell was filled by electrolyte that was the mixture of ethanol and perchloric acid with the volume ratio of 4:1. The mixture of perchloric acid and ethanol is so exothermic and explosive. (High precautions should be considered for mixing these two solutions).

In this case these solutions were mixed inside an ice bath. The aluminum piece was held between the heads of the pincer. The cell with red wire connected to the positive terminal and the alligator from one side connected to the negative terminal and from the other side connected to the pincer. The temperature was kept under 10 °C because of the two reasons; first the explosive nature of perchloric acid and ethanol mixture especially by applying the voltage and another reason is that the higher temperature causes the local heating of the sample during passing the voltage. When the voltage is increasing in its initial seconds, the current density also increases sharply and the local temperature of the sample will increase as well. The low temperature of the solution helps the uniform distribution of heat on sample surface and prevents the local burning.

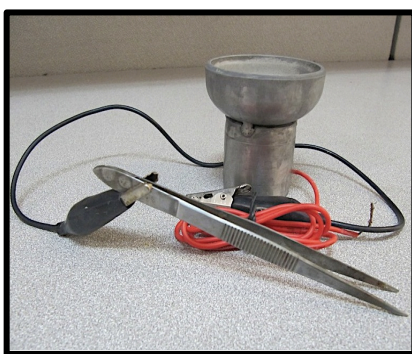


*Fig 3.4 Electropolishing cell with the bowl to pour the electrolyte and the pincer for holding the aluminum foil*

The voltage was adjusted at 10V for the beginning of electropolishing. Dark oxide layer was formed on the surface of aluminum in initial seconds of the reaction. This layer

was felt down and the voltage decreased to 7 V to continue the electropolishing. The whole procedure time changed between 15 to 20 minutes till obtaining the bright surface.

### ***3.1.3 First anodization step***

After surface cleaning, the aluminum piece was ready for the next step; i.e first anodization step. The aluminum piece was placed at the bottom of the cell and 0.3 M oxalic acid was placed inside the cell. After connecting the wires the voltage of 40 V was applied through the electrolyte while the electrolyte was agitated and the temperature was kept at 10 °C by peltier. The distance between two electrodes was 3 cm and the surface area of the sample exposed to the electrolyte was about 0.8 cm<sup>2</sup>. The first anodization was done for different period of time of about 30 min and 2 hours.

### ***3.1.4 Etching***

To have the perfect template, two-step anodization is highly recommended. Usually the oxide layer formed on aluminum surface in the first step, is removed in etching process. During this process, the undesired and disordered oxide layer was etched and just the pores traces are remained which are considered as a pattern or sites for the pore growth in second anodization process.

This layer was etched in solution of 1.8wt% chromic acid and 5wt% phosphoric acid. The sample was drawn in this solution and the temperature was kept at 65 °C. The etching time was variable and was dependent on first anodization time. After etching, the sample was rinsed several times with distilled water and dried in air.

### ***3.1.5 Second anodization step***

The sample from etching step again was placed at the bottom of the cell. The experimental conditions for second anodization step were the same as first anodization step i.e. oxalic acid electrolyte (0.3 M) with vigorous agitation, distance between electrodes of 3 cm, temperature of 10 °C and voltage of 40 V. Dependent on the thickness of the final template, the time of this step varied from 120 seconds to 2 hours. This is the advantage of electrochemistry that makes it possible to control the thickness of the



materials by control the amount of current density passing through the material and the deposition time. Ultrafine templates with thickness of 100 nm can be obtained. After this process the sample was taken out from the cell and it was rinsed with distilled water and dried in ambient temperature. In figure 3.5 the AAO fabrication step is shown. As it can be seen the first anodization results in non-uniform and distorted channels. Removing this distorted oxide layer by etching leaves a highly ordered concave pattern on the aluminum surface (figure 3.5 d). In second anodization step, the highly ordered and regular channels are obtained.

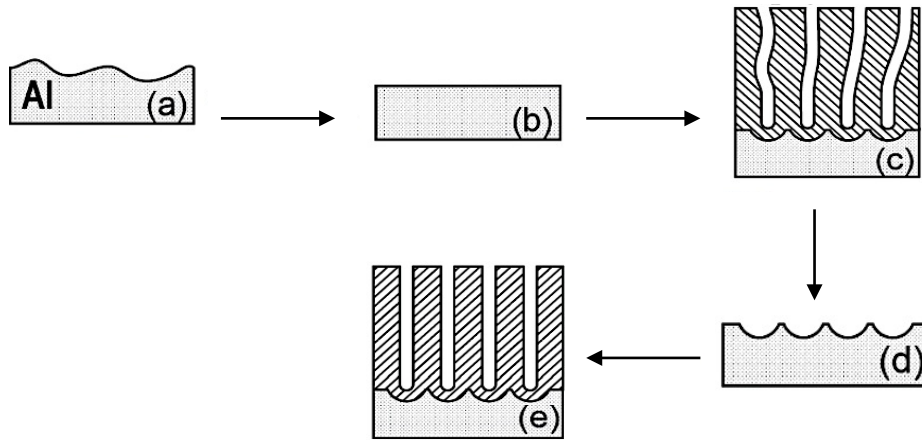


*Fig 3.5 Schematic view of AAO template fabricated steps: (a) untreated aluminum, (b) electropolished aluminum, (c) 1 st anodization, (d) Etching and (e) 2 nd anodization*

### **3.1.6 Pore-widening**

The pores diameter in AAO template can be extended by pore widening process in which the sample was placed in 6wt% solution of  $H_3PO_4$  at  $35\ ^\circ C$ . The phosphoric acid dissolved the template and the pores diameter was extended and the distance between pores was reduced. The dissolution rate of aluminum oxide layer depends on the time in this process. The control of time is so important to have desired diameter for pores. If the time exceeds the optimum time, the template is etched so fast by acid and the pores extend so much and they merge together resulting in disordered and undesired template. The final diameter can be adjusted depending on the application. It means that the morphology and nature of the deposited materials determine the pore diameter. For example for nanowire synthesis, the template with smaller pores is suitable and for nanorods the template with bigger pore diameter.

It should be taking into account that the nature of material is important in the matter of if their molecule size can be matched with pore diameter or not.

### ***3.1.7 Making the template conductive***

Because the method using in this project is electrochemical deposition of materials into the pores of AAO template, thus it is important to make the template conductive to serve as working electrode. Although the AAO is formed on electrically conductive aluminum metal, AAO itself is not conductive because of the presence of the barrier layer. Thus when the electrodeposition of materials is targeted, it cannot be used as working electrode especially when the electrodeposition voltage is too low.

This barrier layer usually has the thickness between 10 to 50 nm which does not allow the current pass through the channels. This layer must be removed and like this the electrons can reach to the bottom of the channels. It means the template must be separated from the aluminum substrate. According to figure 3.6 to reach this barrier layer, first the aluminum foil must be removed. Then the barrier layer must be dissolved in etching solution.

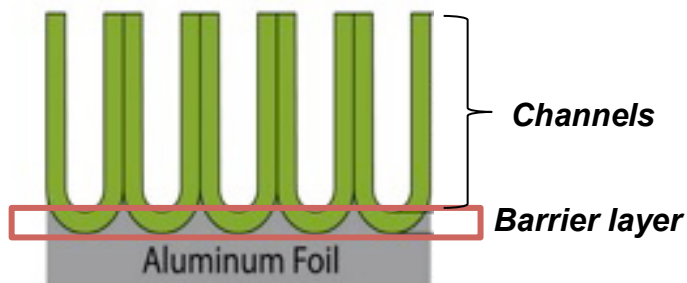


*Fig 3.6 Structure of the AAO template with pure aluminum substrate, barrier layer and channels*

To do so after pore widening the thin layer of Au was deposited on template. Then the template with Au layer was connected to the piece of aluminum with Ag exsposy paste. This piece of aluminum is like a support for the template. The AAO template is so brittle and fragile and after removing of aluminum foil, the template could be fractured easily. When the thickness of template is less than 5 micrometers this procedure will be so tricky especially for ultrathin templates (less than 200 nm of thickness).

Now the aluminum foil is faced up and can be removed by dissolution in solutions such as  $\text{HgCl}_2$ ,  $\text{CuCl}_2/\text{HCl}$ ,  $\text{SnCl}_4$ , and methanol/ $\text{I}_2$  [177, 178]. Mercury (II) chloride is toxic and environmentally dangerous solution. Copper (II) chloride and tin (IV) chloride are corrosive and may cause the damage of the AAO template without framing the template. According to Meng *et al* Methanol/ $\text{I}_2$  solution is not toxic and is considered as good choice because of its selectivity to etch aluminum metal rather than alumina [179].

In this work the diluted solution Copper (II) chloride was used. The aluminum foil was dissolved in 0.1M  $\text{CuCl}_2$ , 50 ml of distilled water and 25ml of HCl. After rinsing the sample several times with distilled water, the barrier layer was removed and the closed bottom of channels were opened in 5wt%  $\text{H}_3\text{PO}_4$ . The time of etching with acid is so important and depends on the template and barrier layer thickness. If the time exceeds from the optimum time, the template is over etched and the over pore opening results in damage of the template and distortion of the channels. This procedure is shown in figure 3.7.

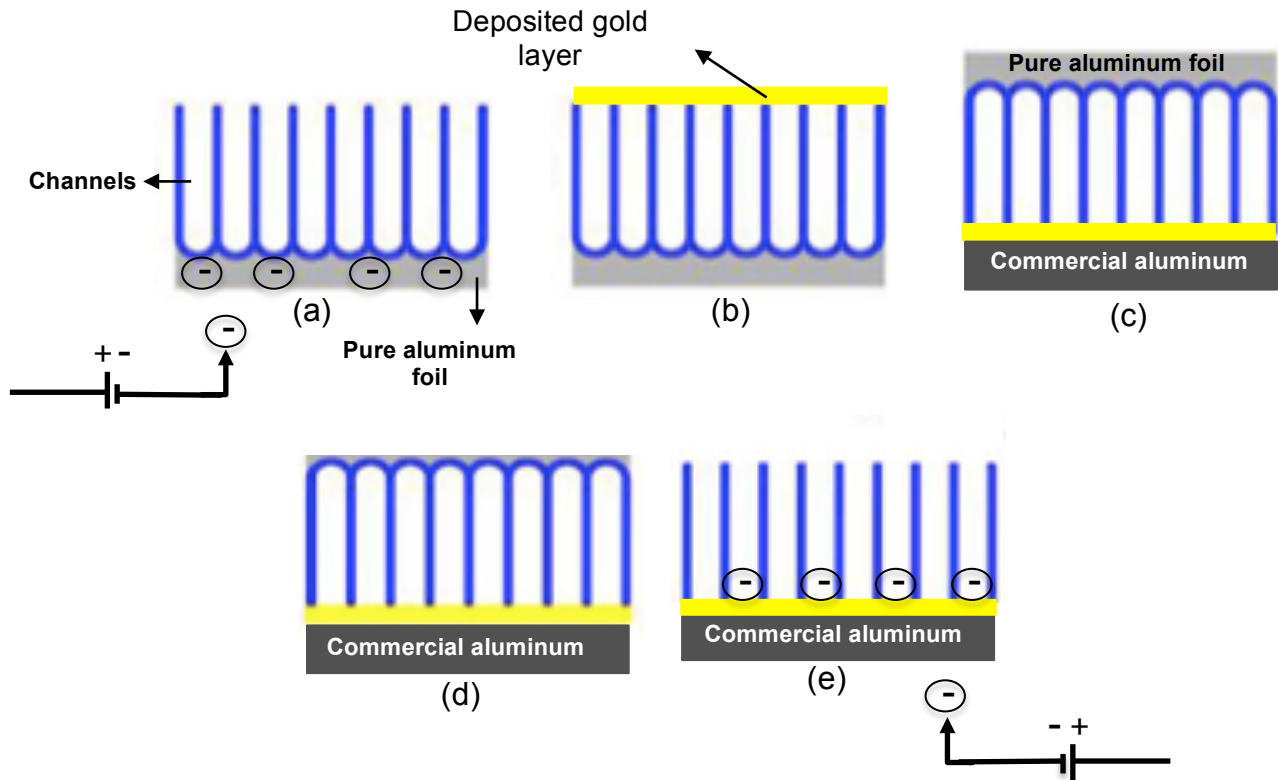


Fig 3.7 Steps involved in making conductive template: (a) template with barrier layer and channels, (b) sputtering Au thin film, (c) stick the template from Au face to the commercial aluminum by silver epoxy (d) dissolution of pure aluminum with mixed solution of  $\text{CuCl}_2$ ,  $\text{H}_2\text{O}$  and HCl, (e) barrier layer dissolution and pore opening in 5wt% $\text{H}_3\text{PO}_4$

After this treatment, the template was opened from the both side. One side was connected to the Au layer and conductive commercial aluminum sheet (which will be connected to the terminal of potentiostat for electrodeposition) without presence of barrier layer, thus the electrons can pass through the bottom of channels and electrodeposition was possible and the other side was ready for filling by the materials during electrodeposition process. At the end of these steps, transparent aluminum anodic oxide template was obtained.

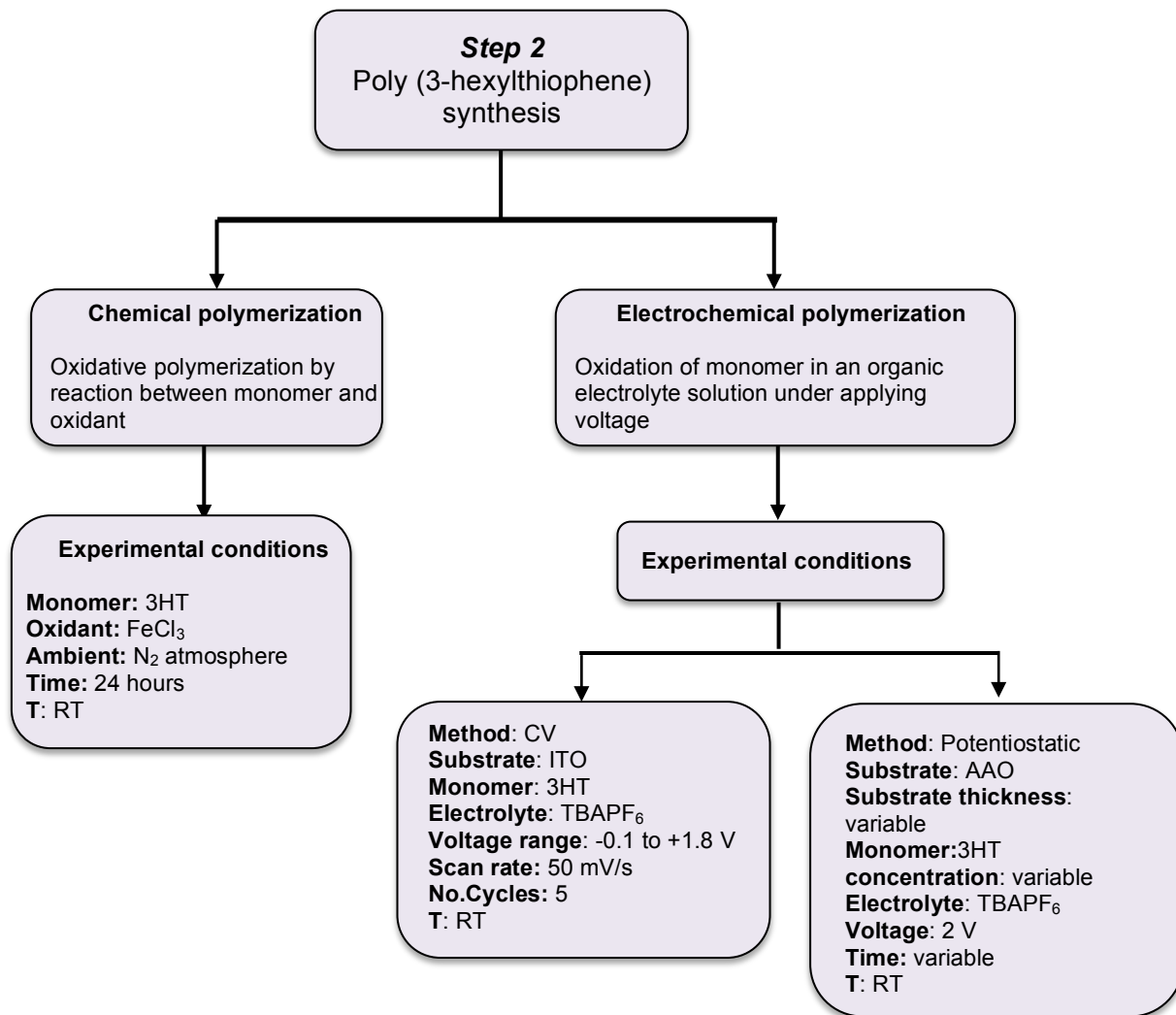
The experimental parameters which were involved in two-step anodization process are summarized in table below.

*Table 3.1 Experimental parameters involved in anodization process*

<b>Parameter</b>	<b>Material and conditions</b>		
<b>Electrolyte</b>	Oxalic acid 0.3 M		
<b>Cathode</b>	Al Sheet		
<b>Anode</b>	Pure Al (to be anodized)		
<b>Voltage</b>	40 V		
<b>Temperature</b>	10 °C		
<b>First anodization time</b>	30 min and 2 hours		
<b>Etching</b>	<b>Solution</b>	<b>Temperature</b>	<b>Time</b>
	1.8wt%H <sub>2</sub> CrO <sub>4</sub> and 5wt%H <sub>3</sub> PO <sub>4</sub>	65 °C	10 and 40 min
<b>Second anodization time</b>	5, 8, 10, 20 and 240 min		

### 3.2 Second step: Polymerization- Synthesis of poly (3-hexylthiophene) (P3HT)

Poly (3-hexylthiophene) was obtained by two different routes of chemical polymerization and electrochemical polymerization. The characteristics of polymer from each method will be explained in next chapter. Flowchart below shows this step.



Flowchart 2. Synthesis steps for polymerization of poly (3-hexylthiophene)

#### 3.2.1 Chemical polymerization

P3HT was synthesized by oxidative polymerization of 3-hexylthiophene (3HT) monomer and anhydrous  $\text{FeCl}_3$  as an oxidant. The materials were used without any further purification. The solution of  $\text{FeCl}_3$  (4mmol) in 50 mL chloroform was placed in 3-

necked flask. After stirring for 1 hour, the monomer (1mmol) in 10 mL of chloroform was added to this solution drop wise. The mixture was left under continuous magnetic stirring for 24 hours at room temperature and nitrogen atmosphere. The inert atmosphere was applied to prevent any side reactions. The black product was transferred to methanol and stirred for couple of minutes. The black precipitate was filtered with a vacuum filtration system and dried at room temperature before characterization [180, 181]

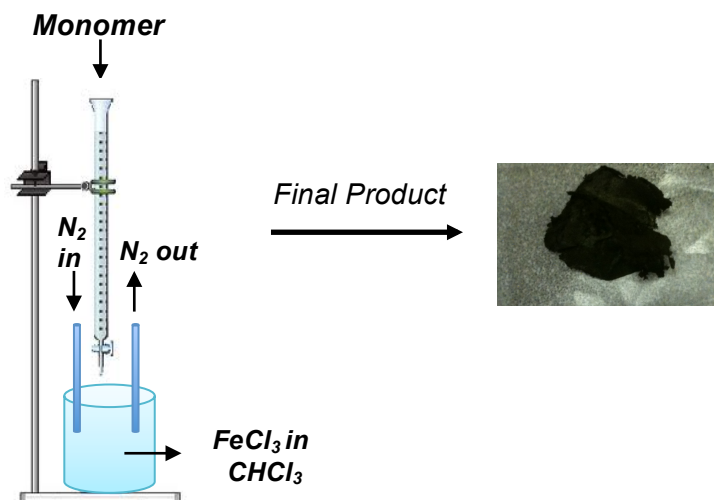


Fig 3.8 Left side: chemical polymerization procedure, Right side: obtained poly (3-hexylthiophene) by this method

According to the general mechanism of chemical oxidative polymerization, first the radical cations are formed by oxidation of 3-hexylthiophene monomer and reduction of Iron (III) chloride. Then two radical cations are combined to form a dimer following by re-oxidation of 3-hexylthiophene dimers and coupling with other radical cations. The oxidation and coupling process continue to produce the poly (3-hexylthiophene)[182].

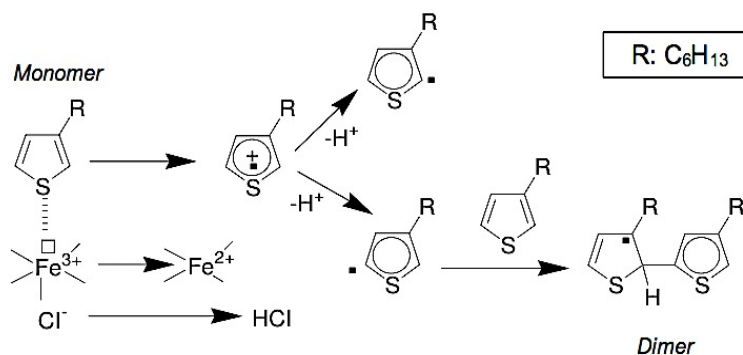


Fig 3.9 Schematic view of chemical oxidative polymerization mechanism for poly (3-hexylthiophene)[182]

### ***3.2.2 Electrochemical polymerization***

#### ***3.2.2.1 Electrochemical polymerization on ITO substrate***

Poly (3-hexylthiophene) was synthesized electrochemically in one component 3-electrode cell using Potentiostat. The reference electrode and counter electrode were Ag/AgCl and Pt wire respectively. The indium tin oxide (ITO) was used as working electrode. The substrate was cleaned by boiling in isopropyl alcohol and acetone for 30 minutes in each solvent following by sonication in 50:50 isopropyl alcohol: acetone for 15 minutes and finally rinsed several times in de-ionized water. The 0.1 M solution of tetrabutylammonium hexafluorophosphate (TBAPF<sub>6</sub>) in acetonitrile was placed in the cell as electrolyte. Then the monomer 3HT (5mM) was added to the solution. The Cyclic voltammetry was applied for 5 cycles by sweeping the voltage between -0.1 V to +1.8 V with the scan rate of 50 mV/s. The electropolymerization carried out at room temperature.

The black polymeric film on ITO was washed several times with acetonitrile and then dried at ambient temperature before characterization [135]. Figure 3.10 shows this procedure and the final product. The mechanism of polymer formation in electropolymerization is shown in figure 3.11. By applying the voltage, the monomer (3HT) oxidized to its radical cation. Since the electron transfer reaction is much faster than the diffusion of the monomer from the bulk solution, thus the high concentration of radicals maintain near the working electrode surface. The second step is the coupling of two radical cations to form a dihydro dimer which transform to a dimer after loss of two protons and rearomatization. This rearomatization makes the driving force of chemical step. The dimer is oxidized more easily than the monomer and under applied voltage dimeric radicals are generated. Then the dimeric radical couples with monomeric radical. Then electropolymerization continue through successive electrochemical and chemical steps until oligomer becomes insoluble in the electrolyte and precipitates on the electrode surface [135, 183].

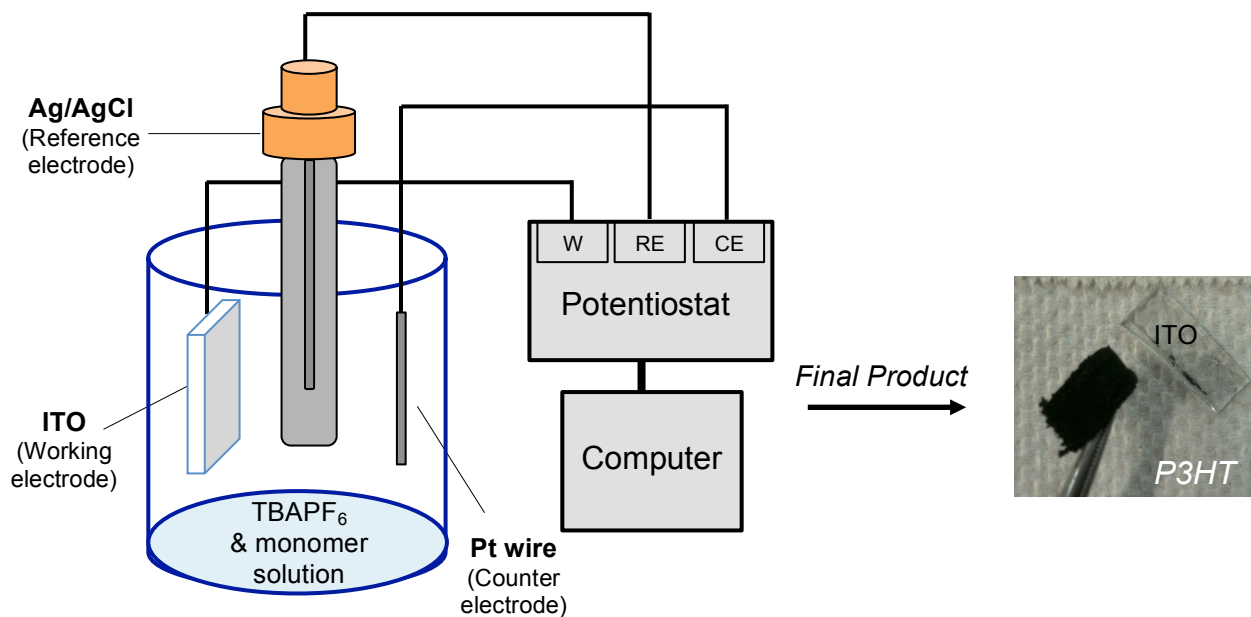


Fig 3.10 Left side: electrochemical polymerization procedure, Right side: obtained poly (3-hexylthiophene) by this method

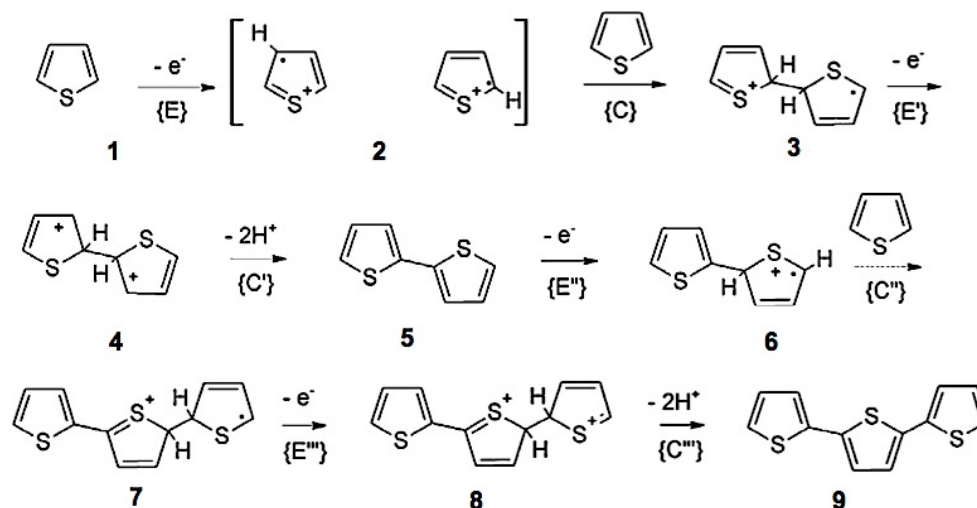


Fig 3.11 Schematic view of electropolymerization mechanism for poly (3-hexylthiophene). C: chemical step and E: electrochemical step[183]

### 3.2.2.2 Electrochemical polymerization on AAO template

After finding the oxidation/reduction information for P3HT from cyclic voltammetry method, the polymer was deposited with potentiostatic method into the channels of AAO.



To do this first the AAO converted to the conductive template with the procedure which was explained in part 3.1.7. Then the conductive AAO was connected to the working electrode of the potentiostat. The counter electrode and reference electrode were Pt wire and Ag/AgCl (saturated KCl) respectively. The polymer synthesis was done at room temperature with adjusting the applied voltage at 2 V. The electrolyte was 0.1 M solution of TBAPF<sub>6</sub> in acetonitrile (AN). In this case the effect of three parameters were investigated; thickness of the AAO template, monomer concentration and deposition time to find the optimum condition for free- standing polymers. The polymer with different length were obtained.

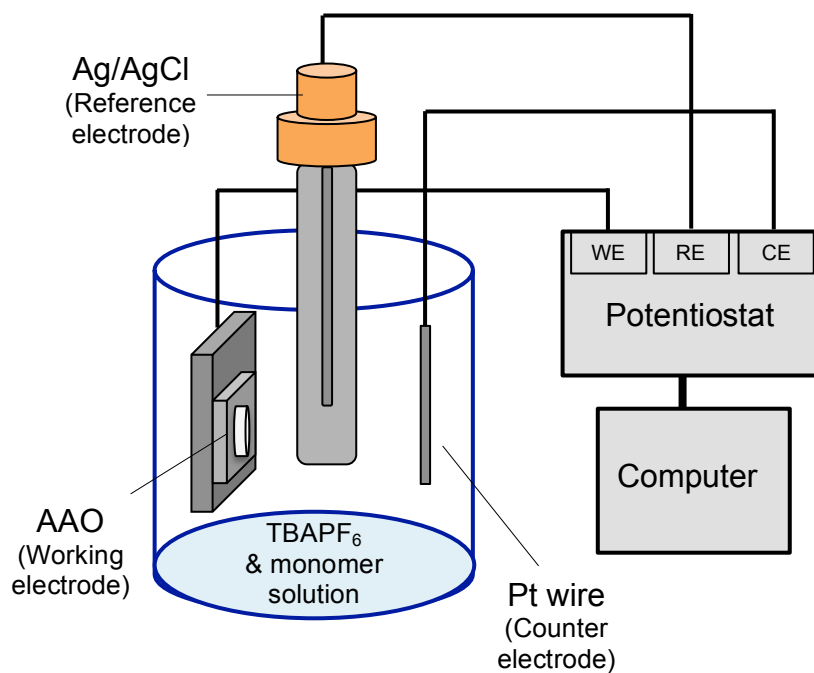
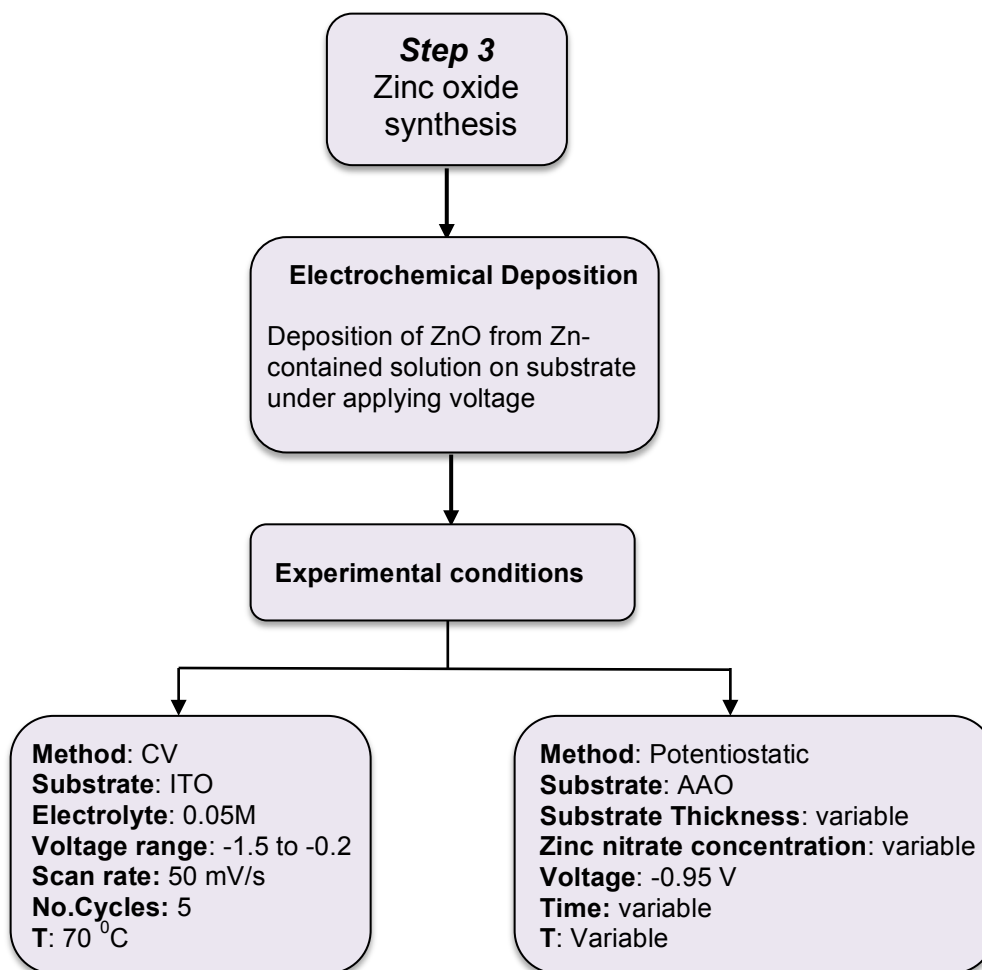


*Fig 3.12 Schematic view of set up for electropolymerization of P3HT onto the channels of AAO template*

### **3.3 Third step: Electrodeposition of Zinc oxide**

Zinc oxide was electrodeposited on two substrates from the zinc-contained solution. The flowchart below shows the steps of this procedure.



*Flowchart 3. Synthesis steps for electrochemically deposition of ZnO*

### **3.3.1 Electrochemical deposition of ZnO on ITO**

First the cyclic voltammetry was applied to find out the deposition conditions like voltage and time. In this method the working electrode, reference electrode and counter electrode were ITO, Ag/AgCl (saturated KCl) and Pt wire respectively. The substrate was cleaned by boiling in isopropyl alcohol and acetone for 30 minutes in each solvent following by sonication in 50:50 isopropyl alcohol: acetone for 15 minutes and finally rinsed several times in de-ionized water.

The electrolyte was zinc nitrate 0.05M and the bath temperature adjusted at 70 °C according to literature. The voltage swept between -1.5 V to -0.2 V with the scan rate of

50 mV/s for 5 cycles. After formation of the zinc oxide on ITO, the film was washed several times with distilled water. Figure 3.13 shows this procedure and final zinc oxide film formed on ITO substrate.

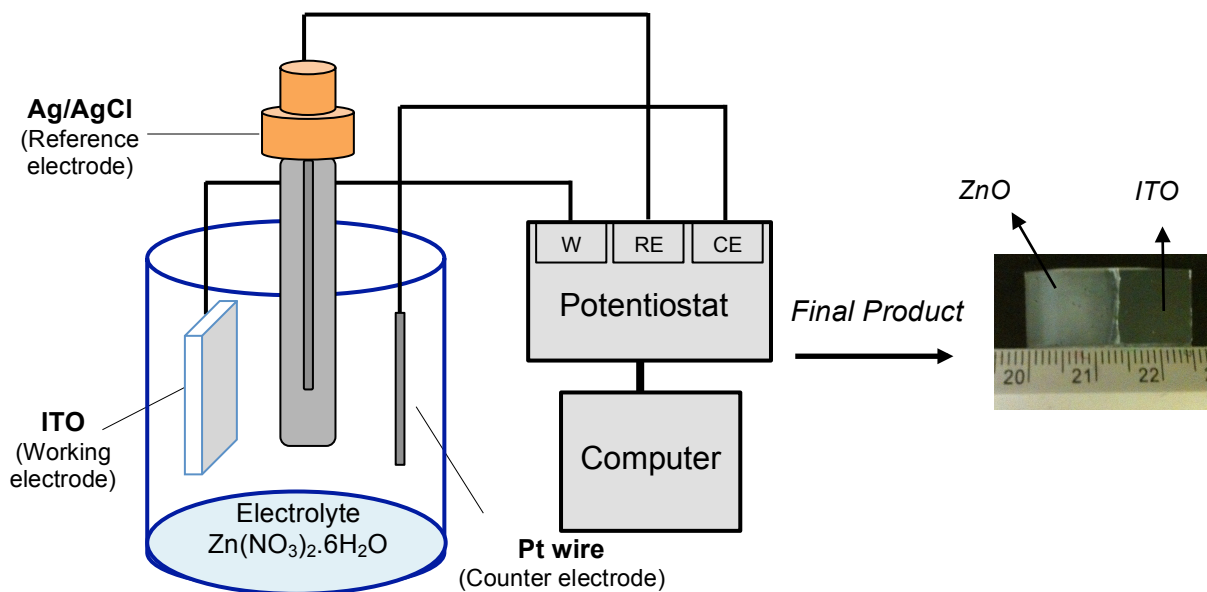
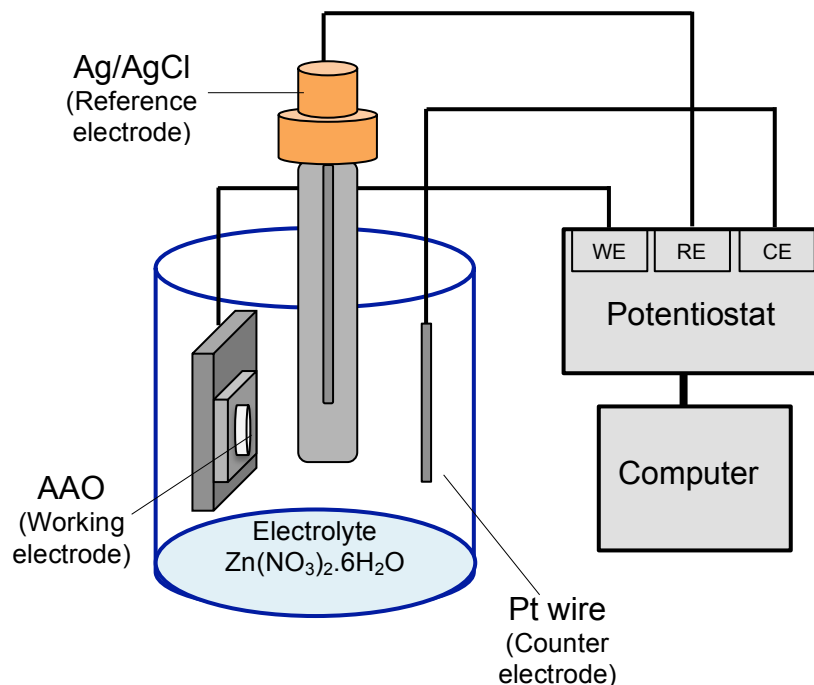


Fig 3.13 Schematic view of set up for electrodeposition of ZnO on ITO substrate

### 3.3.2 Electrochemical deposition of ZnO on AAO template

Cyclic voltammetry gave us the information on oxidation/reduction of zinc oxide which helped us to deposit it onto the channels of AAO template.

To do this first the AAO converted to the conductive template with the procedure which was explained in part 3.6.1. Then the conductive AAO was connected to the working electrode of the potentiostat. The counter electrode and reference electrode were Pt wire and Ag/AgCl (saturated KCl) respectively. The electrolyte was the aqueous solution of  $Zn(NO_3)_2 \cdot 6H_2O$  and the voltage was adjusted at -0.95 V. The concentrations of electrolyte, temperature of the bath and deposition time were varied to find the optimum experimental parameters in our case. The zinc oxide electrodeposition was carried at concentration of 0.05M and 0.005M, temperature of 70 and 80 °C and deposition time of 1800, 900 and 300 seconds. Figure 3.14 shows the set up for this procedure.



*Fig 3.14 Schematic view of set up for electrodeposition of ZnO on AAO substrate*

### ***3.4 Devices and the characterization methods (used in this project)***

#### ***3.4.1 Power source:***

A power supply is a device that supplies electric power to an electrical load. The term is most commonly applied to electric power converters that convert one form of electrical energy to another, though it may also refer to devices that convert another form of energy such as mechanical, chemical and solar to electrical energy. In this project Leader regulated DC power supply (LPS-164A) was used to fabricate the template by anodization process.

#### ***3.4.2 Sputtering:***

Sputtering is a technique used to deposit thin films of a material onto a surface by creating a gaseous plasma and then accelerating the ions from this plasma into some source material. In this project the Rotary-Pumped Sputter Coater/Carbon Coater (Q150R ES) was used to deposit the Au layer on the template surface. This device belongs to

belongs to Centro de Investigación e Innovación en Ingeniería Aeronáutica (CIIIA)-FIME-UANL.

### **3.4.3 Microstructural analysis**

To see the morphology of the sample two techniques were used:

- Atomic Force Microscopy (AFM) is ideal for the quantitatively measuring the nanometer scale surface roughness and visualizing the surface nano-texture on many types of material. This method was used to observe the surface roughness of original aluminum and its surface after mechanical and electrical polishing. This device - Scanning probe microscope (Angstrom Advanced Inc. AA3000)- belongs to Materials Laboratory I, FCQ-UANL

- Scanning Electron Microscopy (SEM): shows very detailed three-dimensional image at very high magnification (up to  $\times 300000$ ) of the materials. With SEM it is possible to obtain secondary electron images of many organic and inorganic materials with nanoscale resolution, allowing topographical and morphological studies. Also it is possible to know about the chemical composition of material by EDS (electron dispersed spectroscopy). In this project the structure and template thickness, morphology of P3HT and ZnO were observed by SEM JEOL JSM6701F located in LACMIMAV, FCQ-UANL.

### **3.4.4 Optical characterization**

To analyze the optical properties of the samples the following methods were applied:

- Ultraviolet-Visible (Uv-vis) spectroscopy: is widely utilized to quantitatively characterize organic and inorganic nanomaterials. A sample is irradiated with electromagnetic waves in the ultraviolet and visible ranges and the absorbed light is analyzed through the resulting spectrum. It can be employed to identify the constituents of a substance, determine their concentrations and to identify functional groups in molecules. Wide range of materials can be analyzed with this technique. The samples can be either organic or inorganic and may exist in gaseous, liquid or solid form. As the device operates on the principle of absorption of photons that promotes the molecule to

an excited state, it is an ideal technique for determining the electronic properties of nanomaterials. UV-vis spectroscopy not only is used for characterization, but also for sensing applications. In this project this technique was used to determine the adsorption band and band gap of materials. The device- UV spectrophotometer (UV-1800 SHIMADZU)- belongs to laboratory Materials I, FCQ-UANL.

- Fourier Transform Infrared Spectroscopy (FTIR): identifies the unknown materials and determines the quality or consistency of a sample and amount of component in the mixture. In this project FTIR used to determine the functional groups in synthesized polymer structure. The device can be found in the Materials Laboratory I, FCQ-UANL.

- Photoluminescence (PL):

Photoluminescence is the emission of optical radiation (ultraviolet, visible or infrared) characteristic of a material as a result of optical excitation. These measurements carried out with PL spectrometer Exemplar BWTEK placed in Thermoscience laboratory in Instituto de energía renovable- UNAM, Temixco, Morleos.

#### **3.4.5 Electrical characterization**

- Cyclic voltammetry: is the most widely used technique for obtaining qualitative information about electrochemical reactions by the study of redox systems. In this project the information on peak potential and current and HOMO/LUMO energy level electrodeposited poly (3-hexylthiophene) as well as peak potential and current of electrodeposited zinc oxide was obtained by this method using the Potentiostat Solartron SI 1278 belongs to Laboratory of Corrosion, FIME-UANL.

- Conductivity measurements: Ohm's law defines the relation between potential (V) and current (I). The resistance (R) is the ratio between V and I and depends on the thickness of the film. In this project the conductivity of polymer was calculated by applying the voltage on the polymeric film. From the slope of V-I curve, resistance is obtained and by knowing the thickness of the film, the conductivity is calculated. The Picoammeter/

voltage source Keithley 6487 located in FIME-UANL was used to measure the conductivity of the polymeric films.

#### ***3.4.6 Surface and structural characterization***

- Profilometer: is a measuring instrument used to measure a surface's profile, in order to quantify its roughness. This technique allows us to measure the thickness of the thin film deposited on substrate. To determine the thickness of the polymer and zinc oxide films on ITO, this technique was used with Tencor Alpha-Step 100 Profilometer/Surface Profiler located in Photovoltaics lab I in Instituto de energía renovable, UNAM, Temixco.

- XRD (X-ray diffraction): The atomic planes of a crystal cause an incident beam of X-rays to interfere with one another as they leave the crystal. This phenomenon is called X-ray diffraction. This technique determines the orientation of a single crystal or grain, the crystal structure of an unknown material and measures the size, shape and average spacing between layers or rows of atoms. In current thesis the X-Ray diffractometer model Rigaku Miniflex Desktop Diffractometer was used to analyze the crystallinity of the polymer.

*Chapter 4*  
*Results & Discussions*



In this chapter the results of our experiments will be introduced in three parts; template fabrication, polymer synthesis and zinc oxide synthesis and the characterization of the samples by different characterization methods and analysis will be discussed.

#### 4.1 Pre-treatment on pure aluminum surface

The AFM image of pure aluminum in its original state, after mechanical polishing and after electropolishing is shown in figure 4.1(a), (b) and (c) respectively.

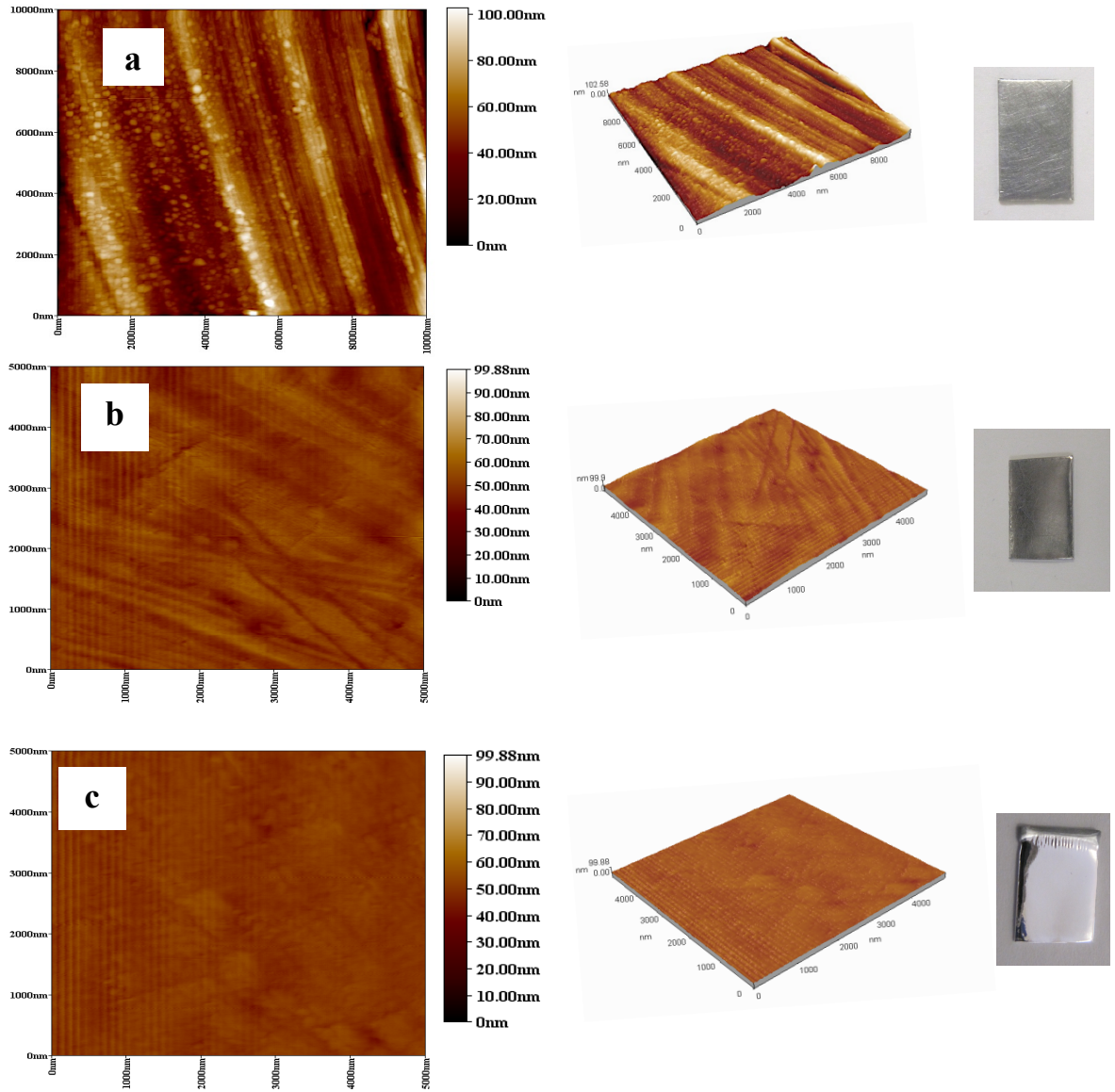


Fig 4.1 AFM images of pure aluminum surface: (a) original surface, (b) after mechanical polishing and (c) after electrochemical polishing

According to the images, original surface of pure aluminum had many scratches and dirt and it was not uniform. After mechanical polishing, the surface was more clean and gained more uniformity but still with some scratches. To remove completely the scratch, electrochemical polishing was done which presents in figure 4.1(c). After electropolishing, the Al surface was shiny, uniform and free of scratches and ready to be anodized.

Figure 4.2 is a current-voltage curve obtained by potentiostat during electropolishing of pure aluminum. As it can be seen from the curve, by increasing the voltage, the current density also increases and in this stage the thin layer of aluminum oxide was formed on aluminum surface which could be seen by necked eyes. The voltage continues to increase but because of non-conductive and highly resistive nature of this layer, the current cannot pass through this layer and decreases. By more increase in voltage, the breakdown of this layer happened. With no resistive layer against the current, the voltage reached the plateau and in this stage electropolishing took place. By passing the time, the aluminum surface was etched more and the process was continued until the mirror-like surface was observed.

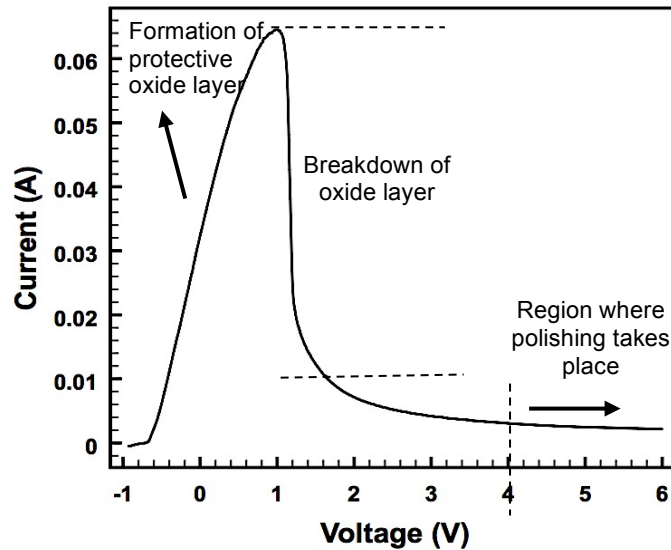


Fig 4.2 I-V curve during electropolishing on pure aluminum obtained by potentiostat

#### 4.2 Anodization of aluminum and fabrication of AAO template

As it was explained in previous chapter, before doing experiments on pure aluminum, anodization steps were done on aluminum alloy (Al1100) to modify the

experimental conditions which had effect on the quality of the final template such as pore diameter, inter-pore distance and template thickness. Although there is extensive information in literature on optimum conditions for fabrication of AAO template with desire pore diameter, inter-pore distance and thickness [ 184 , 185 , 186 , 187 , 188,189,190,191,192,193] the experimental conditions were optimized in our case to obtain the optimum template. After determination of experimental parameters with Al1100, the anodization steps applied on pure aluminum.

Figure shows the template which taken out from the cell after second anodization step. The shiny surface is pure aluminum and the dark circle is the aluminum oxide template formed on the aluminum metal. Two pieces of the templates fabricated on Al1100 and pure aluminum were cut and taken to the SEM to observe the morphology as shown in figure 4.4 (a) and 4.4 (b) respectively.

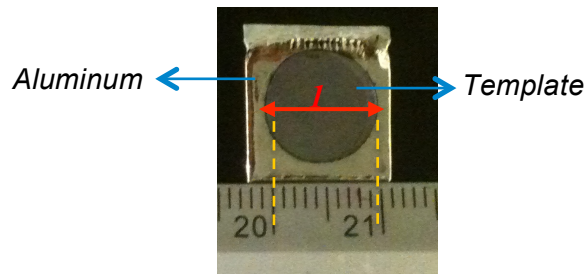


*Fig 4.3 Fabricated template on aluminum substrate with diameter of 1 cm*

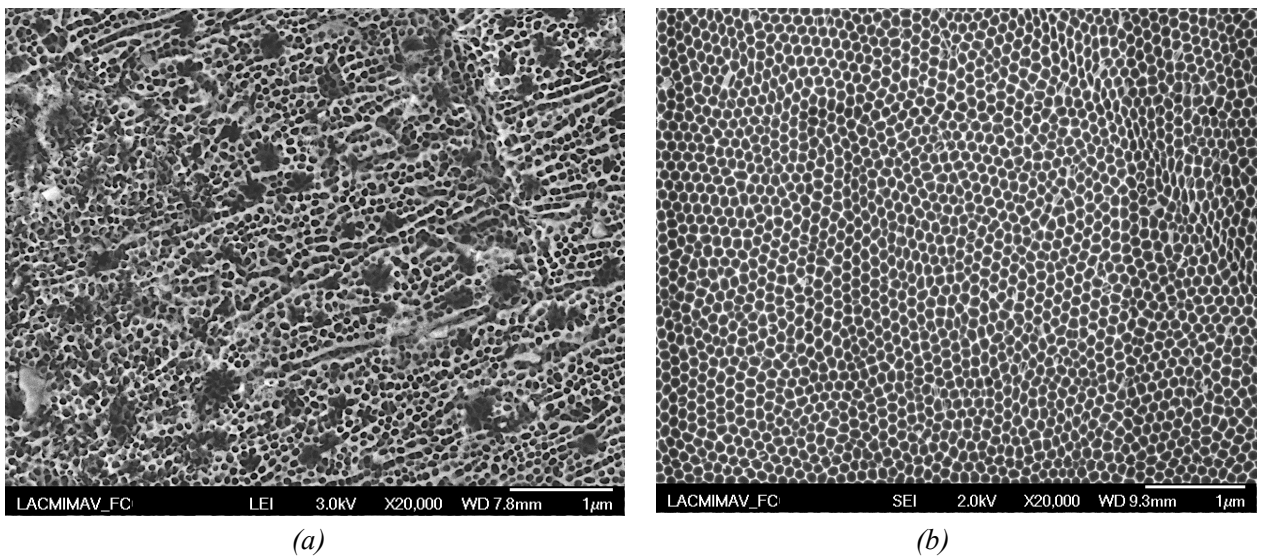


*Fig 4.4 SEM image of AAO template on (a) Al1100 and (b) pure aluminum both after second anodization in oxalic acid 0.3 M at 40 V for 120 min, the image scale is 1 µm*

As it can be seen in image (a) the pores that were formed on the surface of impure aluminum were not ordered. They had different diameter as well as not uniform distribution.

In some parts of the sample merging of various pores and formation of one big pore was observed. This non-uniformity of pore distribution is due to the defect and microstructure of impure aluminum. The regularity and distribution of pores which are forming in anodic film, are strongly influenced by the surface structure of aluminum. The microstructure of pure aluminum and Al1100 are different in average grain size and boundaries because of presence of different elements in the case of Al1100. The Al1100 has more surface defects, smaller grain size and more grain boundaries which resulted in less quality of final template. Table 4.1 shows the elemental composition for Al1100 and pure aluminum which obtained by optical emission spectroscopy and from the handbook of aluminum respectively [194].

*Table 4.1 Elemental comparison between Al1100 and pure aluminum obtained by optical emission spectroscopy and handbook of aluminum*

Elements (%)	Pure aluminum	Al1100
Al	99.999	97.20
Mn	-	1.26
Fe	0.002	0.607
Si	0.001	0.27
Cu	0.001	0.204
Mg	-	0.202
Zn	0.001	0.172
Ti	0.001	0.0189
Cr	-	0.0109

#### **4.2.1 Control the first anodization and etching time**

The first anodization is important step in template fabrication because it is considered as pre-patterning on aluminum surface. Hence the time of this step should be controlled. The etching time usually is 2/3 of the first anodization time.

There are different reports in literature on time of first anodization [184, 185,190, 197]. These reports suggested that the time of second anodization is more important in ordering of pores. In our experiments this time adjusted in 30 minutes and 2 hours.

However in our case the SEM images showed that the template with longer first anodization time and etching were more uniform and ordered. Two templates (figure 4.5) were anodized both of them in oxalic acid (0.3 M), at room temperature and 40 V. The etching carried out in the mixture solution of chromic acid (1.8wt%) phosphoric acid (6wt%) in both cases.

For template (a) the first anodization time and etching were 30 minutes and 20 minutes respectively. Template (b) was fabricated during 2 hours of first anodization and 80 minutes of etching. The second anodization for both templates was 2 hours. According to the SEM image, the template (b) with longer first anodization time had better quality. Hence longer first anodization provides the better quality of final template since in first anodization step by increasing the time, the pores get more ordered and they can grow uniformly.

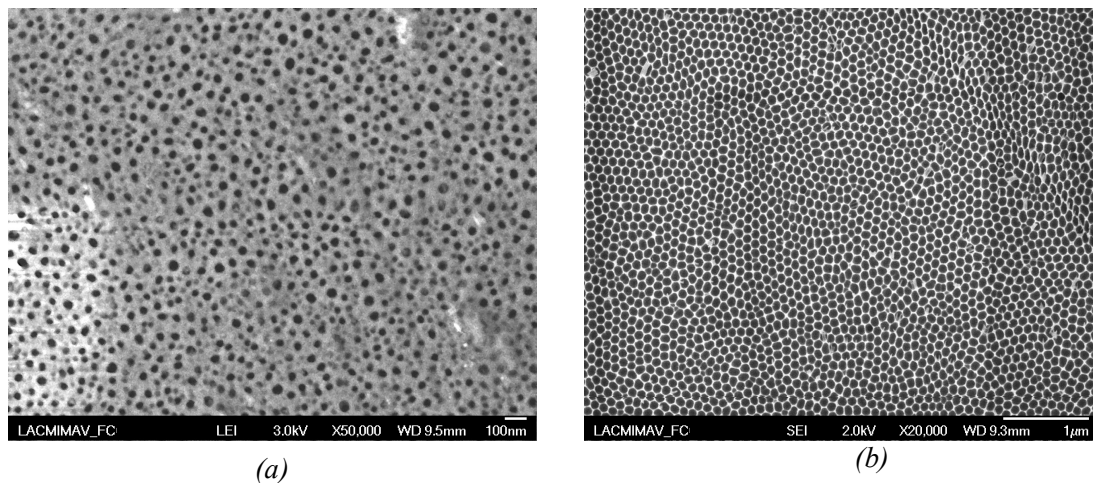
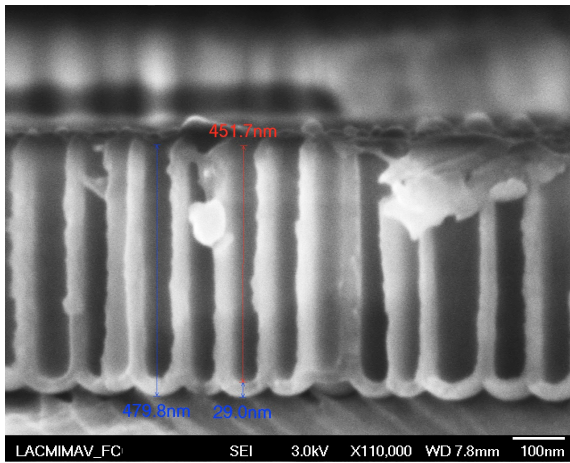


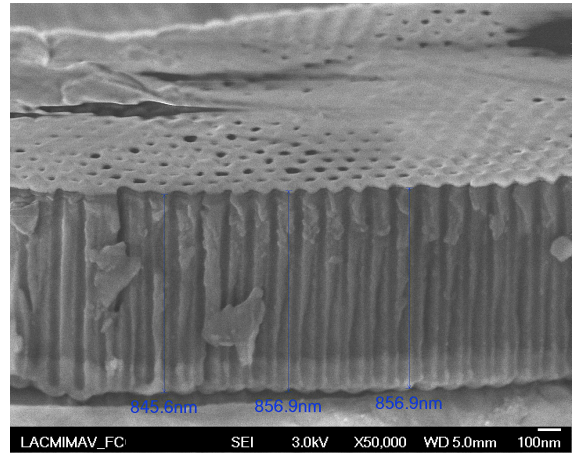
*Fig 4.5 SEM image of AAO template (a) First anodization of 30 minutes, etching of 10 min and second anodization of 2 hours (b) First anodization of 2hours, etching of 40 min and second anodization of 2 hours, the image scale is 1  $\mu$ m*

#### **4.2.2 Control the second anodization time**

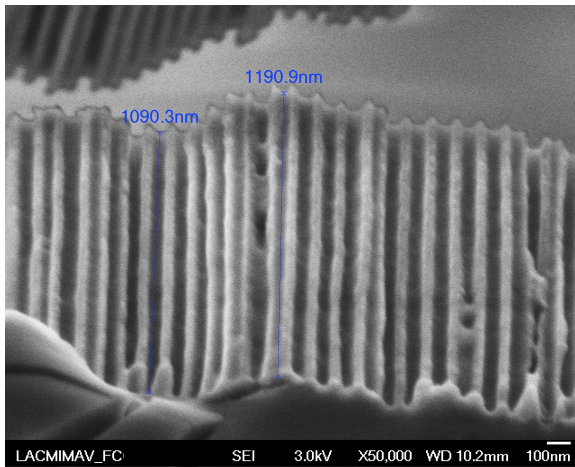
After finding the optimum conditions which were 2 hours of first anodization and 40 minutes of etching, the time of second anodization was varied to find the relationship between the time and thickness of the template. Figure 4.6 shows the obtained templates with different thickness. For all experiments the second anodization was carried out in oxalic acid (0.3 M), at room temperature and 40 V. The thickness of the template increased linearly with the second anodization time as it is shown in figure 4.7.



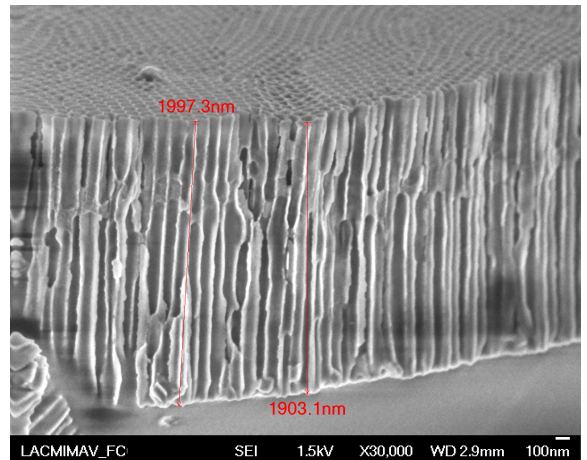
(a) First anodization: 2 hr, Etching 40 min, second anodization: 5 min



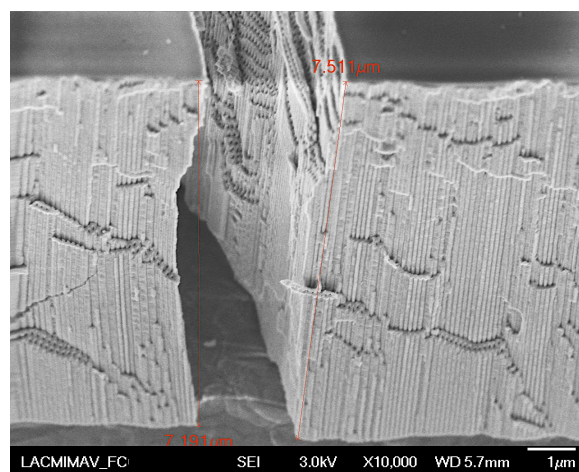
(b) First anodization: 2 hr, Etching 40 min, second anodization: 8 min



(c) First anodization: 2 hr, Etching 40 min, second anodization: 10 min



(d) First anodization: 2 hr, Etching 40 min, second anodization: 20 min



(e) First anodization: 2 hr, Etching 40 min, second anodization: 2 hrs

Fig 4.6 SEM images of different templates obtained by changing the etching and second anodization time

In figure 4.7 the triangles are the experimental data which showed an excellent fit with the trend line. The second anodization carried out during different time period of 5, 8, 10, 20 and 120 minutes resulting in the templates thickness of 450, 850, 1000, 2000 and 7000 nanometers respectively. The direct line passing from the experimental data has a slope of 1.08. This indicates that the thickness of the template increased around 1.1 nm per second. With this information it is possible to fabricate the template with the desired thickness for any application by adjusting the time for second anodization.

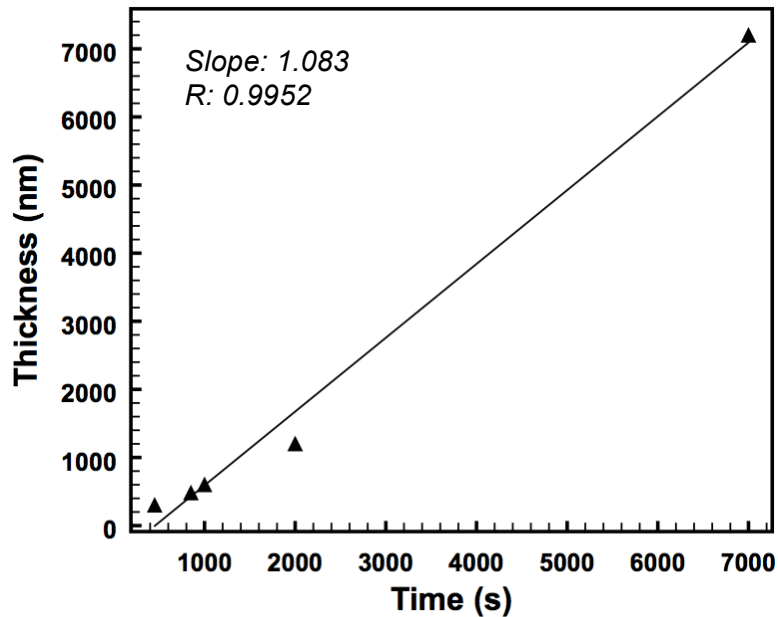


*Fig 4.7 Relationship between the template thickness and the second anodization time (The slope indicates that every second the thickness of the oxide layer increased around 1 nm)*

#### **4.2.3 Control the pore widening time**

After the second anodization, the diameter of pores was in the range of 40-50 nm. Depending on the application that one is searching, the size of pores can increase by etching or dissolution of the oxide layer in H<sub>3</sub>PO<sub>4</sub> 5%wt at 35 °C. In our experiments the etching was carried out for 5 and 10 minutes and in some cases this step was not applied. With pore widening the diameters of the pores can reach to 70-90 nm. If the nanomaterials with large diameter are targeted, the time is increased and if the materials with small diameters are targeted the pore widening is applied for short period of time or this step is not applied. If the template is left in the etching solution for large period of time, it will be destroyed since the over dissolution of the oxide layer results in distortion

of the channels. Figure 4.8 shows SEM images of the template fabricated in 0.3 M oxalic acid, at room temperature and 40 V voltage. The first anodization, etching and second anodization was done for 120 min, 80 min and 120 min respectively. The pore widening was done for 10 minutes. As it can be observed from the images the average pore size before the pore widening was 45 nm and after the pore widening was 67 nm. By increasing the time of this step, the pores with larger diameters can be obtained.

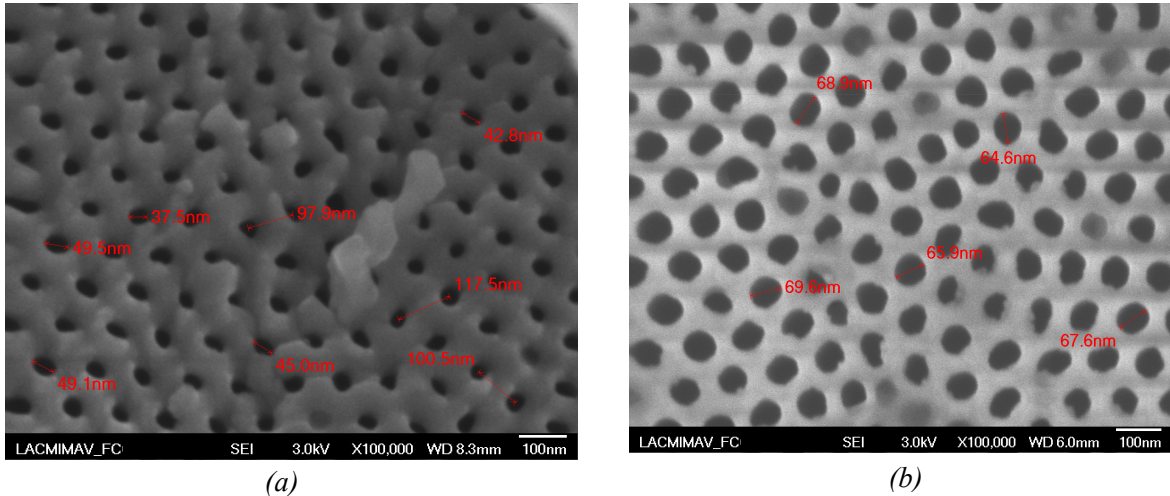


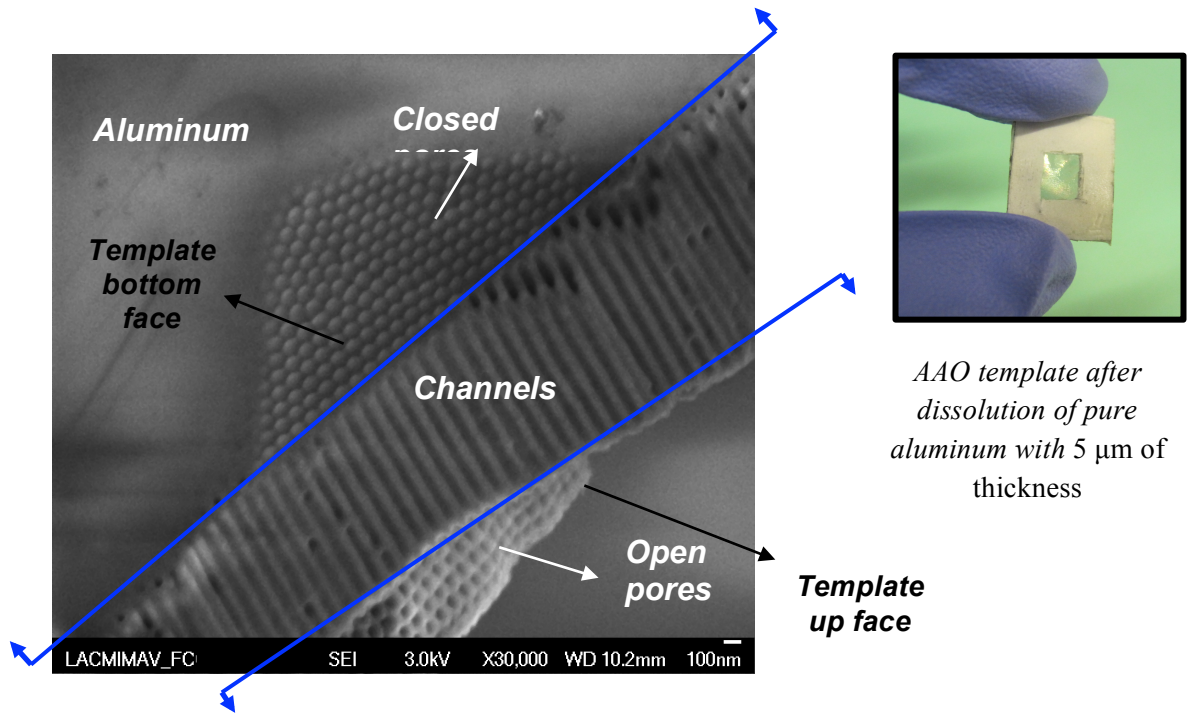
Fig 4.8 The template (a) before pore widening with average pore diameter of 45 nm and (b) after 10 min of pore widening with average pore diameter of 67 nm; the image scale is 1  $\mu$ m

#### 4.2.4 Al substrate removal to obtain conductive template

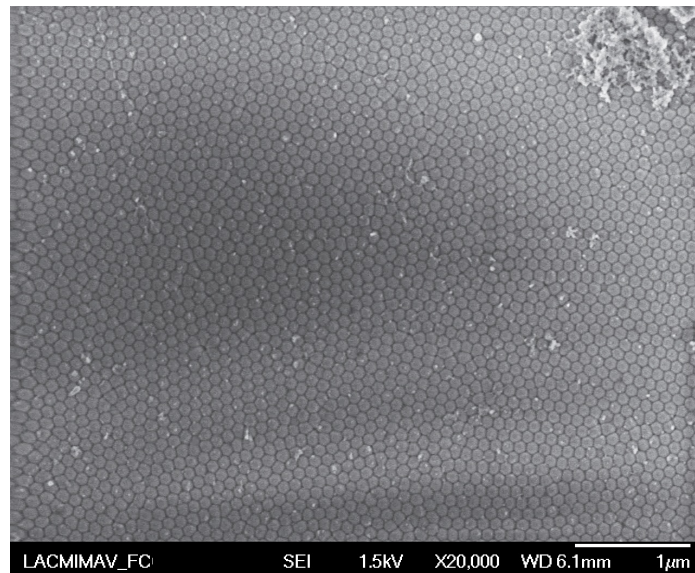
As mentioned in chapter 3 for electrodeposition of the materials inside the pores of template, the barrier layer must be removed with the procedure which explained in part 3.1.7.

In the insert of figure 4.9 the transparent template after aluminum removing is shown. A layer of Au sputtered on the face of the template with open pores. Then the aluminum metal was dissolved completely in 0.1 M  $\text{CuCl}_2$  in HCl and  $\text{H}_2\text{O}$  (1:2 volume ratio). The SEM images 4.9 (a) and (b) shows the results of this procedure.





(a)



(b)

Fig 4.9 (a) SEM image of template structure after partial removing of aluminum metal, (b) the bottom of pores after complete removing of aluminum metal; the image scale is 1  $\mu$ m

The barrier layer was dissolved and the pores were opened from the bottom side in solution of 5wt% phosphoric acid at room temperature. The time of pore opening was controlled for a template with 2 hours of second anodization. For this template the pores

were opened completely after 40 minutes of etching in acidic solution which is shown in figure 4.10 (a) to (d). After this procedure, from one side the barrier layer was dissolved and the pores were opened and from the other side the channels were in direct contact with Au layer and hence the template was conductive and ready to electrodeposit the materials.

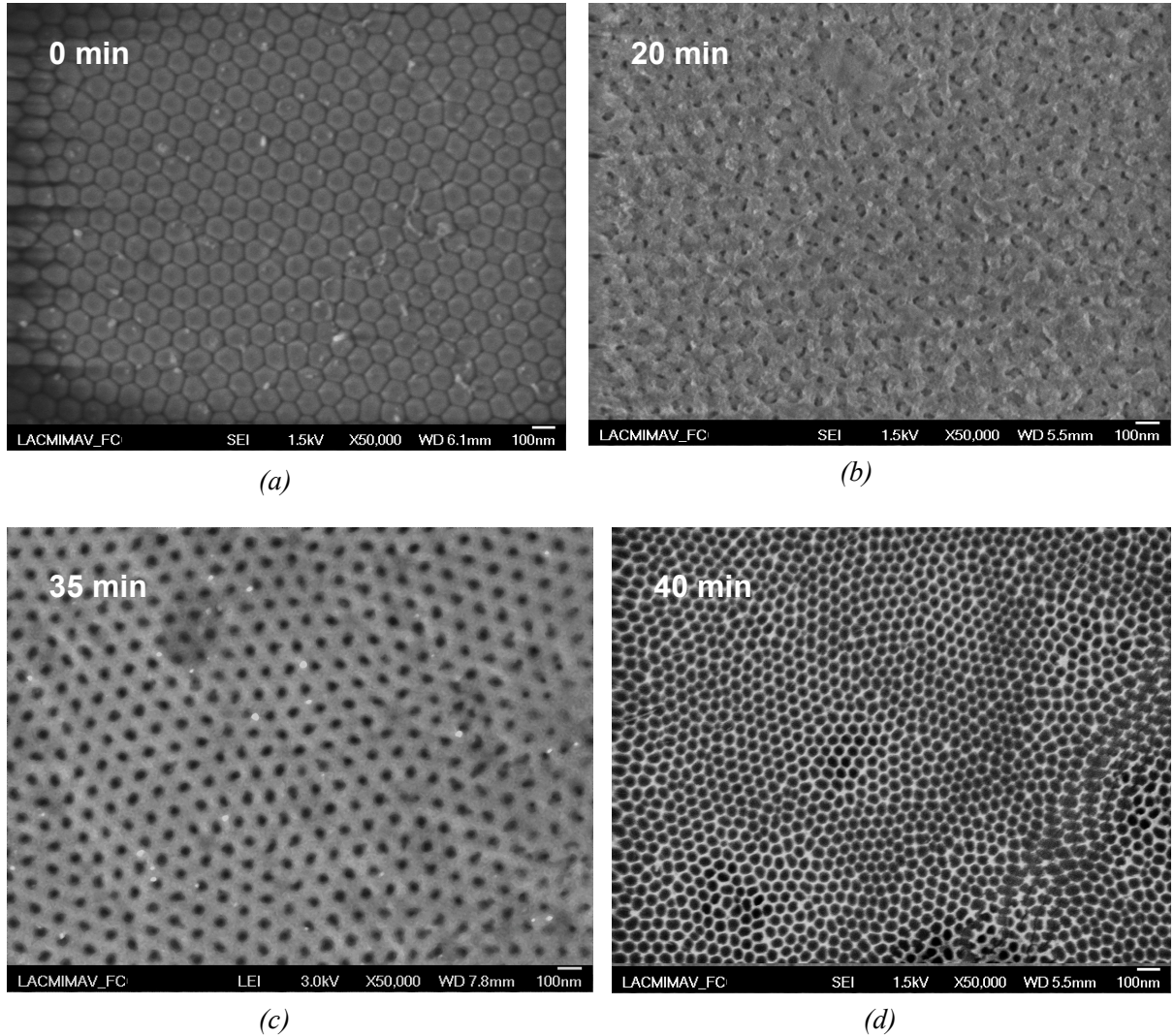


*Fig 4.10 The SEM image showing the bottom of pores; (a) with out pore opening, (b) after 20 min of pore opening, (c) after 35 min of pore opening and (d) after 40 min of pore opening, all in 5wt% phosphoric acid and room temperature. the image scale is 1  $\mu$ m*

#### 4.2.5 Comparison between the experimental data and the theoretical formula for template parameters

Many research groups have proposed the relationship between the template parameters such as pore diameter, inter-pore distance, wall thickness, barrier layer thickness, porosity and template thickness with voltage, current density and anodization time. These formulas are listed below [195,196,197,198,199,200, 201].

$$\text{Pore diameter: } D_p = 1.29 V \quad \text{in which } V: \text{Applied voltage} \quad (4.1)$$

$$\text{Inter – pore distance: } D_{int} = 2.5 V \quad \text{in which } V: \text{Applied voltage} \quad (4.2)$$

$$\text{Wall thickness: } \frac{1}{2} (D_{int} - D_p) \quad (4.3)$$

$$\text{Cell diameter: } 2 \times \text{Wall thickness} + D_p \quad (4.4)$$

$$\text{Barrier layer thickness: } \frac{D_{int}}{2} \quad (4.5)$$

$$\text{Porosity: } \frac{\pi}{2 \times \sqrt{3}} \left( \frac{D_p}{D_{int}} \right)^2 \quad (4.6)$$

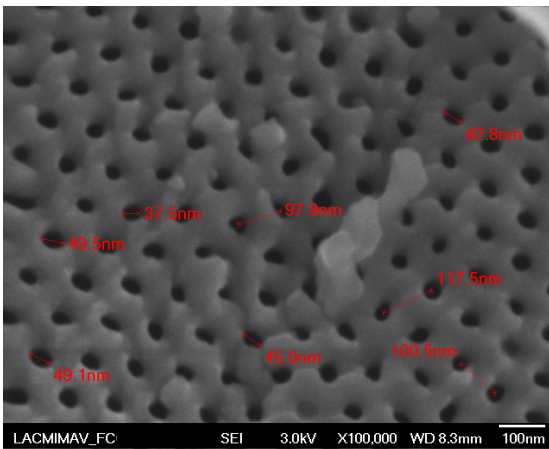
$$\text{Pore density: } \rho_p = \frac{2}{\sqrt{3}} \times \frac{1}{D_{int}^2} \times 10^{14} \quad \text{in cm}^{-2} \quad (4.7)$$

Table 4.2 shows the comparison between theoretical and experimental parameters obtained from our measurements.

Table 4.2 Comparison between experimental and theoretical parameters

<b>Template parameters</b>	<b>Experimental parameters</b> <i>(Observed from SEM)</i>	<b>Theoretical parameters</b> <i>(Obtained from formula)</i>
<i>Experimental conditions:</i> V=40V Sample surface area= 0.785 cm <sup>2</sup> Density of =3.95 gr/cm <sup>3</sup> Molar weight of metal = 26.98 gr/mol		
<b>D<sub>p</sub>: pore diameter (nm)</b>	45.0	51.6
<b>D<sub>int</sub>: inter-pore distance (nm)</b>	105.3	100.0
<b>t<sub>w</sub>: wall thickness (nm)</b>	30.15	24.20
<b>D<sub>c</sub>: cell diameter (nm)</b>	138.0	148.4
<b>t<sub>b</sub>: barrier layer thickness (nm)</b>	34	50
<b>Porosity (%)</b>	16	24
<b>ρ<sub>p</sub>: Pore density (μm<sup>-2</sup>)</b>	96	115

The experimental results are in good agreements with the theoretical calculations. According to the formulas, the pore diameter and inter-pore distance depend on applying voltage. These parameters are shown in figure 4.11 in which the average pore diameter of 45 nm and the average inter-pore distance of 105.3 nm was obtained from our experiment. These values were 51.6 and 100 nm calculated from formulas respectively. These results indicate that the diameter of pores and the distances between the neighboring pores seem to be highly uniform and near the values calculated from formulas.



*Fig 4.11 AAO template fabricated during 2 hours of anodization at 40 V with average pore diameter of 45 nm and the average inter-pore distance of 105 nm*

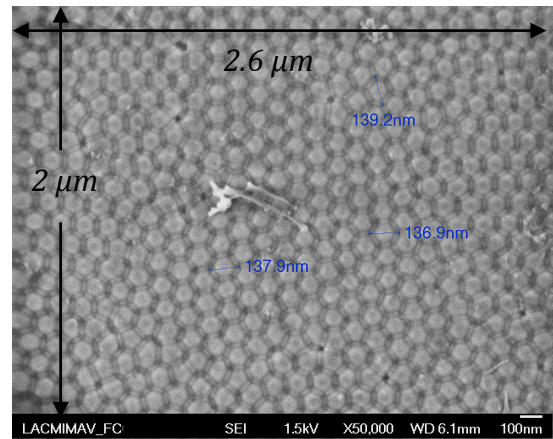


*Fig 4.12 AAO template fabricated during 2 hours of anodization at 40 V with average cell diameter of 138 nm*

Figure 4.12 shows the backside or bottom of the pores after removal of aluminum. In this image the closed-packed hexagonal structure of the cells can be seen clearly with 138 nm average diameter of cell, this value was equal to 148.4 nm in theoretical case. Also the pore distribution was obtained from figure 4.12. In  $2.6 \mu\text{m} \times 2 \mu\text{m}$  area of the sample there are almost 500 pores. Thus the pore distribution is 96 pores in  $1 \mu\text{m}^2$  which equals to 115 pores in  $1 \mu\text{m}^2$  in theoretical case. Figure 4.13 shows the thickness of the barrier layer which was almost 34 nm in our case and was 50 nm obtained theoretically.

The good agreements between our results and calculated values from the reported formulas, show that we could control well the experimental conditions like voltage and temperature. However one can change the parameters by changing the experimental conditions. For example at the same applied voltage but at higher bath temperature, the

dissolution of the oxide layer is faster compared to the anodization at 10 °C. This leads to increase in pore diameter and decrease in pore wall when the experimental data do not follow the theoretical formulas.

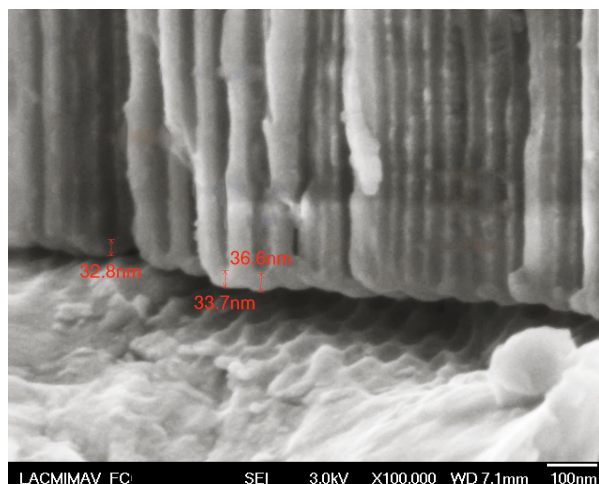


*Fig 4.13 AAO template fabricated during 2 hours of anodization at 40 V with average barrier layer thickness of 34 nm*

### **4.3 Polymer synthesis**

#### **4.3.1 Optical and structural comparison between Chemical and electrochemical polymerization**

After polymerization of P3HT by two methods of chemical oxidative polymerization and electrochemical polymerization which was explained in chapter 3 in part 3.2.1 and 3.2.2 respectively, the samples were characterized by different methods to compare their structure and optoelectrical properties. FTIR was applied to see the functional groups of polymeric chain and confirming that the obtained products were poly (3-hexylthiophene). X-ray analysis was done to obtain the information on crystallinity of the products and Uv-vis was applied to determine the optical properties of polymers. At the end the conductivity of polymers was measured and compared. From now on for facility, the polymer synthesized chemically is named as polymer C and the polymer synthesized electrochemically is named as polymer E.

### 4.3.1.1 Fourier transform infrared spectroscopy (FTIR)

The FTIR spectra for polymer C and E is shown in figure 4.14.

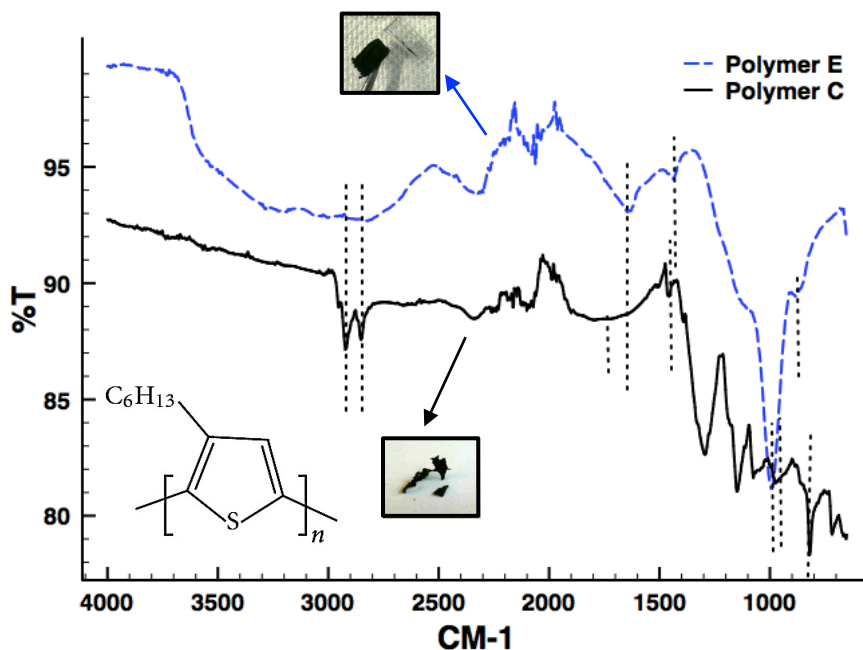


Fig 4.14 FTIR Spectra for the P3HT synthesized by two methods of chemical polymerization (black curve) and electropolymerization (blue dashed curve)

The polymeric films synthesized from two methods, were clearly different as seen by eye and they are demonstrated in figure 4.14. The polymeric film C was a bit brittle and had a rough surface while the polymeric film E had a smooth surface and could be easily peeled off the ITO in one piece. In table 4.3 the bonds and their corresponding peaks for both polymers are listed. The results are in a good agreement with other references [182, 202, 203] indicating that the synthesized polymer from both methods is P3HT.

Table 4.3 Comparison of FTIR spectra of the polymers synthesized from different method

Band assignment	Polymer C Wave number ( $\text{cm}^{-1}$ )	Polymer E Wave number ( $\text{cm}^{-1}$ )
CH <sub>2</sub> stretched vibration bond	2931 and 2852	2885
C=C stretching	1736	1645
C-C stretching	1458	1445
C-H out of plane (Deformation vibration mode)	966	991
C-S bending	821	875

#### 4.3.1.2 X-ray diffraction analysis

Figure 4.15 (a) and (b) shows the x-ray diffraction patterns for polymer C and polymer E respectively. X-ray studies on polymers showed more ordered structure for polymer E rather than polymer C and this can be seen from the sharp peaks at  $16^{\circ}$ ,  $19^{\circ}$  and  $31^{\circ}$ . For polymer C (fig 4.15 a) the single wide-angle peak located at  $2\theta=23.96^{\circ}$  with less intensity represented the side chains disorder. According to the McGehee *et al* the chain packing of the polymers is important factor for charge mobility since a charge must hop to a neighbor molecule to travel through the polymer chain [112].

By using the electrochemical method, regioregular and semi-crystalline P3HT was synthesized while chemical polymerization method resulted in regiorandom and amorphous P3HT. In the case of polymer C, there were more overlaps between the side chains in neighboring stack and these overlaps cause the twisting or distortion of the chains and hence the defect in the polymer structure. The amorphous regions in polymer C act as barrier for the charge transfer and leads to the less conductivity of the polymer. In inset of the figure 4.15 (a), the undesirable coupling of the polymer chain with  $\text{Fe}^{+3}$  was presented. This coupling caused the overlaps between side chains because of the steric repulsion between two adjacent thiophene rings caused by undesirable dopant molecule. The structural difference and hence the polymer properties are dependent on the type of the dopant as well as the polymerization method [204, 205, 206]. Hence according to the figure 4.15 polymer E has shown more crystalline phase and polymer C more amorphous phase.

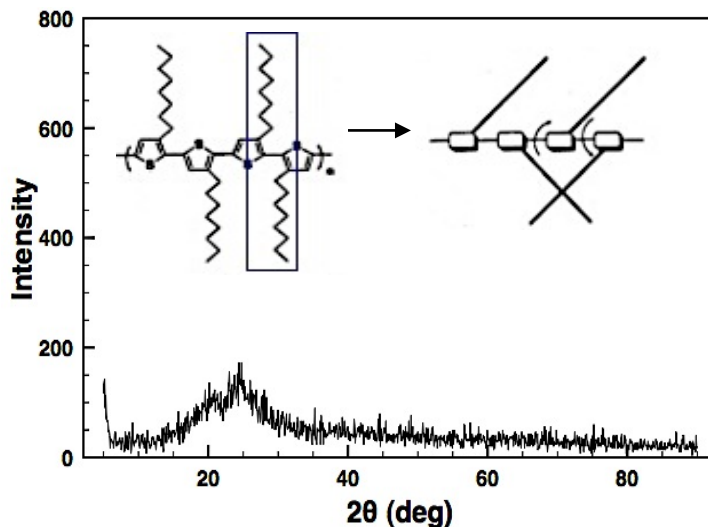


Fig 4.15 (a)

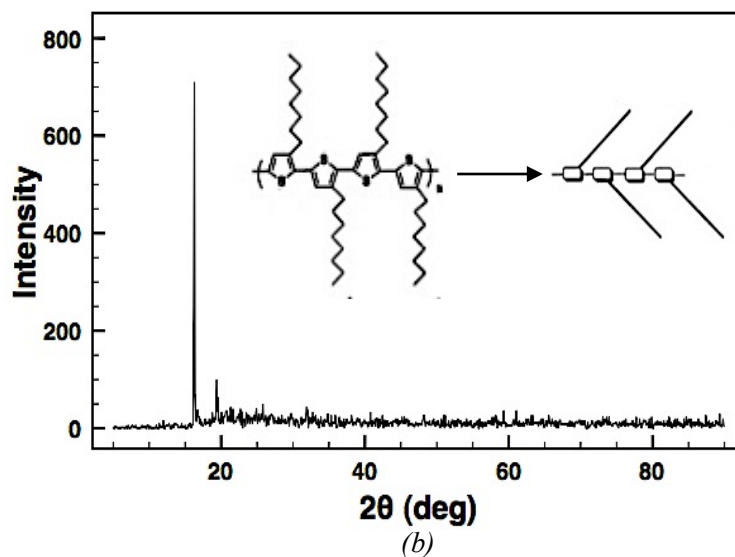


Fig 4.15 X-ray diffraction pattern for (a) polymer C and (b) polymer E. (Insets from [207])

#### 4.3.1.3 Ultraviolet-Visible spectroscopy (UV-Vis)

Figure 4.16 shows the Uv-vis spectra for the polymers. The Uv-vis was performed from 300 to 1000 nm at room temperature. The polymers were dispersed in chloroform. The blue dashed curve corresponds to the polymer E and the black curve shows the Uv-vis spectra of the polymer C. In the blue dashed curve two peaks were observed; one at 589 nm and the other one at 350 nm. The absorption band at 589 nm corresponds to the vibronic structure originated from  $\pi$ -electron orbital overlap between the adjacent thiophene rings. This peak blue shifted to the value of 498 nm for the polymer C which also corresponds to the  $\pi$ - $\pi^*$  transition of the conjugated segments between the adjacent rings causing by moving an electron from a bonding  $\pi$  orbital to an antibonding  $\pi^*$  orbital [208]. In conjugated polymers, the peak at maximum absorption represents the extent of the conjugated length. Therefore the polymer E with longer wavelength adsorption at 589 nm, has higher conjugated length which means less structural defects and disordering for this polymer which also observed in the X-ray diffraction pattern [204]. The peaks at 350 and 365 nm correspond to the  $n$ - $\pi^*$  transition for the polymer E and polymer C respectively which comes from moving an electron from a nonbonding electron pair to an antibonding  $\pi^*$  orbital [208].



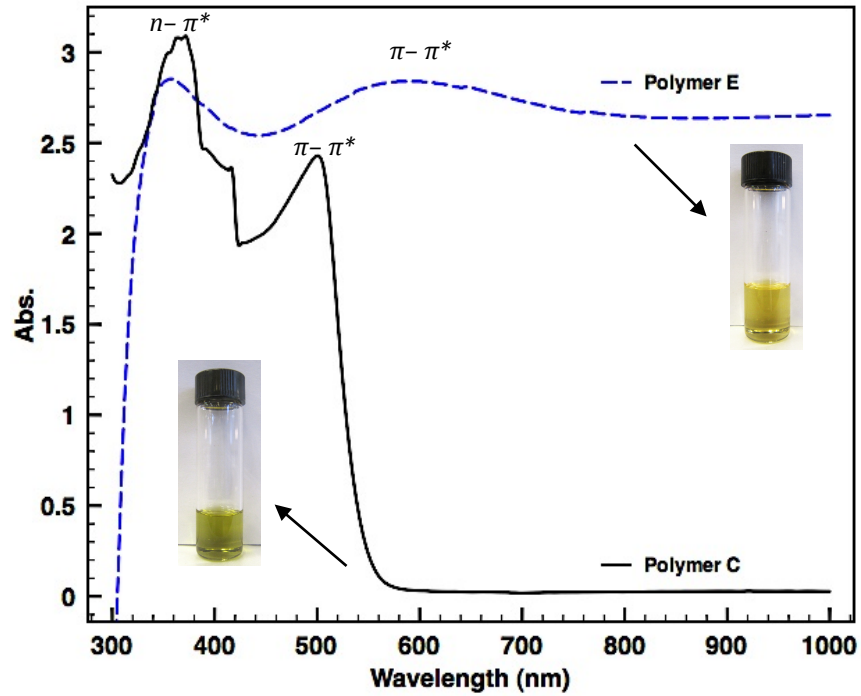


Fig 4.16 Uv-vis spectra for the P3HT synthesized; electrochemical method (blue dashed curve) and chemical polymerization (black curve)

#### 4.3.1.4 Conductivity measurements

Figures 4.17 and 4.18 show the I-V curves for polymer C and polymer E respectively. The curves obtained in voltage range of 0 to 5 V and at room temperature. The conductivity was calculated from the slope of I-V curve which indicates the resistivity according to the Ohm's law ( $V=IR$ ) and by using the following formula:

$$R = \rho \frac{L}{t \cdot w} = \frac{1}{G} \quad (4.8)$$

Where R is resistance,  $\rho$  is resistivity, L is the length of contact, t is the thickness of the deposited materials, w is the contact width and G is the conductance. Hence:

$$G = \frac{t \cdot w}{\rho \cdot L} \text{ and } \rho = \frac{1}{\sigma} \quad (4.9)$$

Therefore:

$$\sigma = \frac{1}{R} \cdot \frac{L}{t \cdot w} \quad (4.10)$$

Where  $\sigma$  is the conductivity. In table 4.4 these parameters are listed. To calculate the conductivity of polymer C, first the powder of polymer which obtained from the synthesis, was compacted by hydraulic press machine resulting in polymeric film with the thickness of 600  $\mu\text{m}$ . Two contacts were painted by carbon paint and the electrodes were placed on contacts then the voltage from zero to 5 was applied by 0.5 V intervals to the polymeric film. At voltage 5V the current reached a value of  $2.8 \times 10^{-4}$  A. The curve perfectly obeyed the ohm's law since all the measurement data (triangles) were matched completely with the trend line.

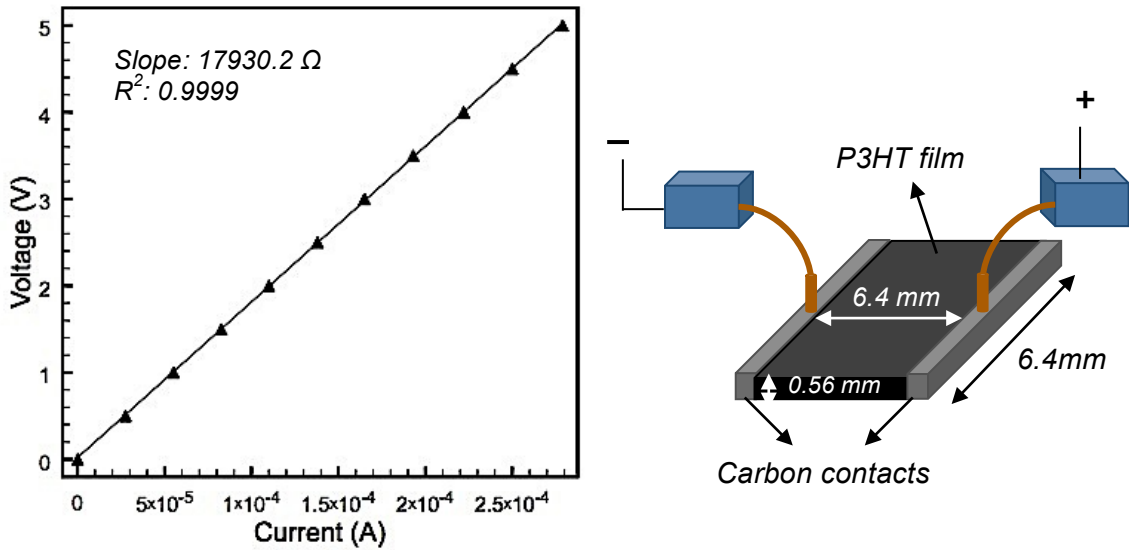


Fig 4. 17 Left side: I-V curve for chemically synthesized P3HT and right side: schematic view of contacts to measure conductivity

To calculate the conductivity of polymer E, there was no need of compressed the polymer since the polymer was deposited on ITO as thin film. A 1.8 mm $\times$ 2.70 mm square with carbon paint was painted on polymeric film and one electrode was placed on the carbon contact and the other one on ITO surface. The voltage from 0 to 5 was applied by 1 V intervals. At voltage 5V the current reached a value of  $2.8 \times 10^{-3}$ A which was 10 times higher than the current reached by polymer C which means less resistivity and higher conductivity of polymer E. The curve obeyed the ohm's law with a good match of experimental data (triangles) with the trend line.

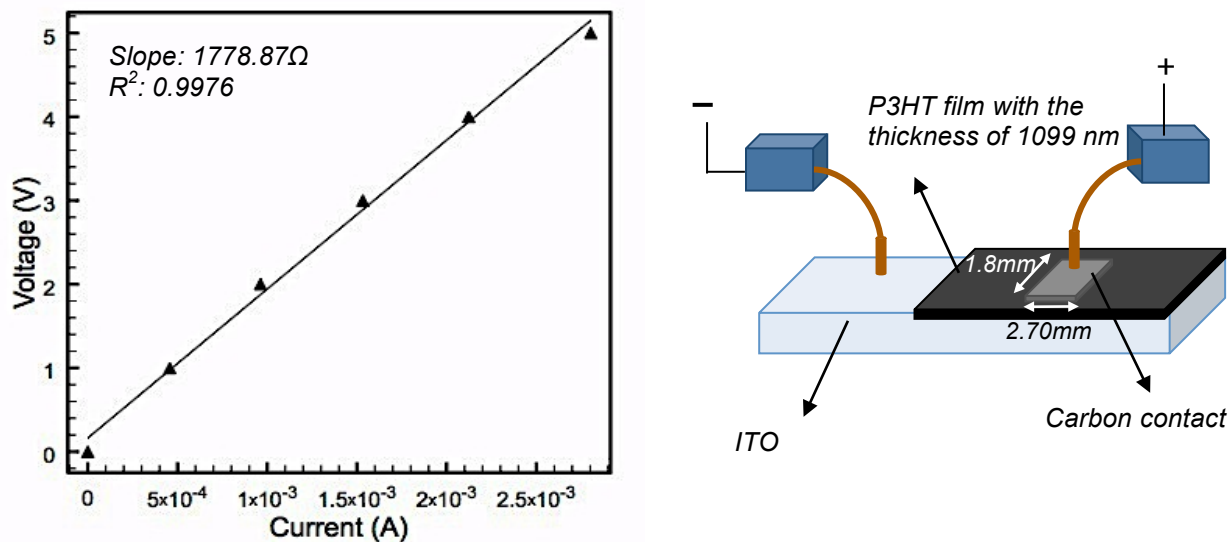


Fig 4.18 Left side: I-V curve for electrochemically synthesized P3HT and right side: the schematic view of the contacts to measure conductivity

Table below shows the parameters for conductivity measurements and the final conductivity obtained for each polymer.

Table 4.4 Parameters for conductivity measurements

<i>Polymer</i>	<i>(t)</i> <i>Thickness</i> <i>(m)</i>	<i>(R)</i> <i>Resistance</i> <i>(<math>\Omega</math>)</i>	<i>(G)</i> <i>Conductance</i> <i>(<math>\Omega^{-1}</math>)</i>	<i>(<math>\rho</math>)</i> <i>Resistivity</i> <i>(<math>\Omega.cm</math>)</i>	<i>(<math>\sigma</math>)</i> <i>Conductivity</i> <i>(<math>S.cm^{-1}</math>)</i>
<i>Polymer C</i>	560 $\mu m$ (0.056 cm)	17930.2	0.00005577	1000	0.001
<i>Polymer E</i>	1099 nm ( $1099 \times 10^{-7}$ cm)	1778.87	0.00056	0.293	3.44

The higher conductivity for the polymer E is because of its higher crystallinity and chain ordering that was discussed in the previous sections.

The comparison between two methods of polymerization showed that the electrochemical method resulted in the better optical behavior and conductivity of the product. Hence this method was selected for depositions of the polymer into the pores of AAO. In the next

part the optoelectrical properties of the electrochemical synthesized P3HT will be introduced.

#### 4.3.2 Optoelectrical properties of the polymer E

The HOMO-LUMO energy levels and the band gap of organic materials can be calculated from two methods of cyclic voltammetry and optical spectroscopy.

##### 4.3.2.1 Cyclic voltammetry for polymer E

Figure 4.19 shows the voltammogram of P3HT. The voltage increased from -0.1 to reach the anodic peak at +1.12 V in which the polymer was in its doped state.

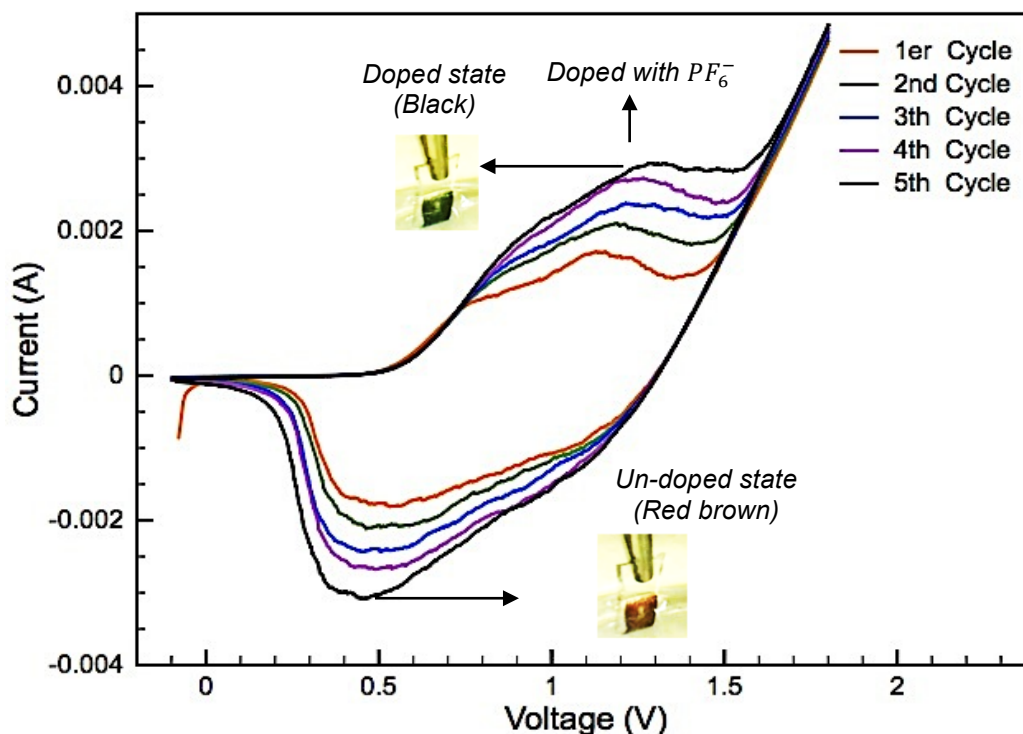


Fig 4.19 Cyclic voltammetry of poly (3-hexylthiophene) in 0.1M TBAPF<sub>6</sub> by applying voltage between -0.1 and +1.8 V, scan rate of 50 mV/s and for 5 cycles

Then the voltage arrived to the final value of +1.8 V and the process followed by sweeping back the voltage from this point to the initial point passing from the cathodic peak at +0.47 V in which polymer was in its un-doped state. The increase of the current peak after each cycle shows the formation and deposition of the polymeric layer on ITO.

The oxidation / reduction process was observed by changing the polymer color from black in oxidation state and red brown in reduction state. The oxidation/reduction process was accompanied with the expansion / contraction of the polymeric film as well as changing the color.

#### 4.3.2.2 HOMO energy level calculation

The HOMO and LUMO energy levels for organic materials can be calculated from the value of oxidation and reduction peaks of voltammogram. According to Bredas *et al* HOMO, LUMO energy levels and the  $E_g$  (band gap) are calculated from the formulas below [209]:

$$E_{\text{HOMO}} = -e [E_{\text{ox}}(\text{onset}) + 4.44] \quad (4.11)$$

$$E_{\text{LUMO}} = -e [E_{\text{red}}(\text{onset}) + 4.44] \quad (4.12)$$

$$E_g = E_{\text{HOMO}} - E_{\text{LUMO}} \quad (4.13)$$

Figure 4.20 shows how to obtain the onset of oxidation peak. This value was equal to 0.6 V. By replacing this value in the formula (4.11) the HOMO energy level was obtained.

$$E_{\text{HOMO}} = -e [E_{\text{ox}}(\text{onset}) + 4.66] = -[0.6 + 4.44] = -5.04 \text{ eV}$$

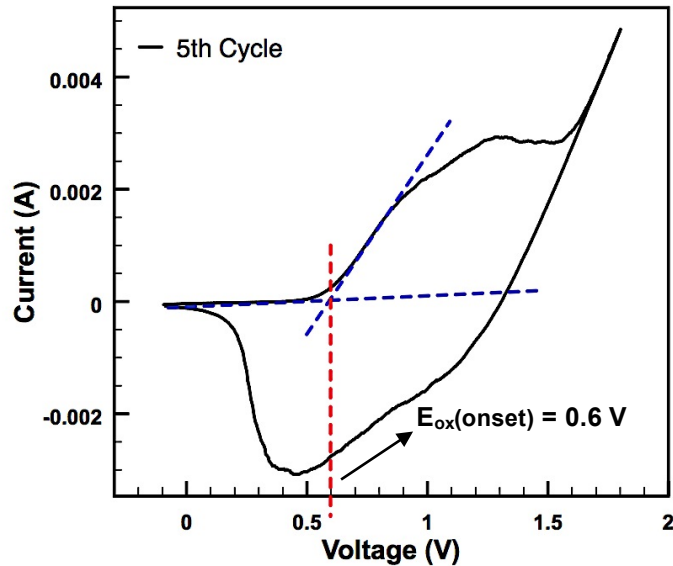


Fig 4.20 Onset of oxidation peak from the 5th cycle of electropolymerization of P3HT

### 4.3.2.3 Band gap and LUMO energy level calculations from Optical spectroscopy- Transmittance spectra

The most direct and perhaps the simplest method for probing the band structure of semiconductors is to measure the absorption spectrum. This spectrum is the result of interaction of an electromagnetic wave with an electron in the valence band which jumps to the conduction band [210]. In order to determine the optical band gap of the polymeric film, the transmittance spectra of the film was recorded at room temperature. The absorption coefficient ( $\alpha$ ) was calculated from the spectrums using the Tauc formula as following:

$$\alpha hv = (hv - E_g)^n \quad (4.14)$$

where  $\alpha$  is the adsorption coefficient,  $hv$  is the photon energy,  $E_g$  is the optical band gap and  $n$  is a constant of 1/2 for allowed direct, 3/2 for forbidden direct, 2 for allowed indirect and 3 for forbidden indirect transitions in the materials. The direct optical band gap of polymer obtained from extrapolation of the straight line in  $(\alpha hv)^2$  vs.  $hv$  plot with the x axis [209] which shows in figure 4.21.

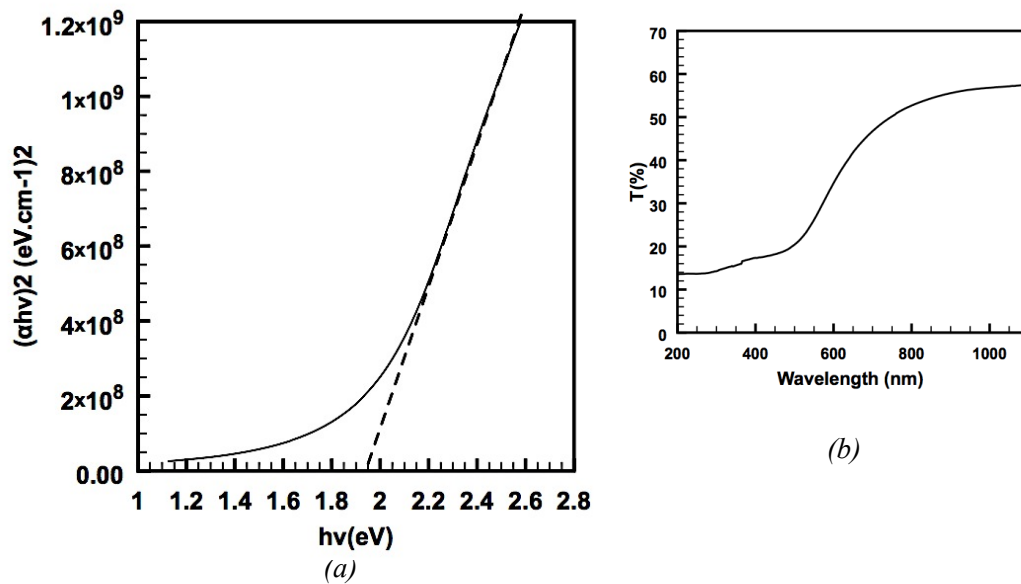


Fig 4.21 (a) Tauc plot:  $(\alpha hv)^2$  vs.  $hv$  extrapolated to zero absorbance for P3HT, the data was collected from the transmittance vs. wavelength (b)

Since the adsorption coefficient depends on the thickness of the thin film, the polymer E thickness was obtained from Profilometer and it was 1099 nm. By knowing this data and the transmittance spectrum, the  $E_g$  of electrosynthesized P3HT was calculated 1.9 eV from the figure 4.21. Now by knowing the value of band gap and HOMO energy level, the LUMO can be obtained and is equal to:

$$E_{\text{LUMO}} = E_{\text{HOMO}} - E_g = 5.04 - 1.9 = 3.14 \text{ eV}$$

#### ***4.4 Polymer deposition into the pores of AAO template***

The poly (3-hexylthiophene) electrochemically deposited into the channels of anodic aluminum oxide template. This procedure was done in 3-electrode cell in which AAO with sputtered Au layer on one side and different thickness served as working electrode with Ag/AgCl and platinum wire as reference and counter electrode respectively. To study the growth mechanism and rate of polymer the electropolymerization was carried at 2 V, room temperature and in different monomer concentrations and deposition time. The electrolyte was 0.1 M tetrabutylamunium hexafluorophosphate (TBAPF<sub>6</sub>) in acetonitrile (AN) containing the dopant agent which is PF<sub>6</sub><sup>-</sup>.

- ★ Note: The applied voltage was selected 2 volts by studding the cyclic voltammetry of P3HT. According to the figure 4.19, monomer oxidation happens at +1.12 V. By increasing the number of cycles, this values increase due to the formation of polymeric layer on substrate surface and reaches at +1.3 V at the end of 5<sup>th</sup> cycle. It means that at voltages higher than +1.12 the oxidation of 3HT monomer is possible. However when the potentiostatic electropolymerization was applied on ITO substrate, at constant voltage of +1.12 V, no polymeric film was formed on ITO surface. The voltage was increased gradually and it was observed that at 2 V the, the P3HT was formed on ITO. There another CV measurement for electropolymerization of P3HT carried out in range of -0.1 V to 3 V. In this CV curve an oxidation peak was observed at 2.5 V and the inset of oxidation was at 2 V. It was concluded that at constant potential, the polymer is deposited between 2 and 2.5 V. Polymer deposited higher than 2.5 V had not good adhesion to ITO surface.

##### ***4.4.1 Control of polymeric nanorods length***

To see the growth rate of polymer inside the nanochannels of AAO template, the monomer concentration was fixed and the electropolymerization time was changed.

Electrochemical polymerization was conducted at 2V vs. Ag/AgCl, monomer concentration of 50 mM (most reported concentration for other conductive polymers and thiophene derivatives) and time of 300 s, 100 s, 30 s and 15 s. In all cases the counter electrode and the working electrode were Pt wire and AAO template with the thickness of 7  $\mu\text{m}$  respectively. Figure 4.22 (a) shows the electropolymerization of 50 mM 3HT during 300 seconds without dissolving the template. As it can be seen from the image, the growth rate of polymer was so fast and the polymer rods came out from the AAO channels and joining together.

As mentioned before, the thickness of the template was 7  $\mu\text{m}$ , however the obtained polymeric rods had a length higher than 7  $\mu\text{m}$  due to the long electropolymerization time. When the polymers go out from the pores, they tend to join together because of their high surface tension. Figure 4.22 (b) shows how the polymers grew out of the channels and laying down on the template surface. Figure 4.22 (c) shows the longitude of the rods after template removing which was about 14  $\mu\text{m}$ . According to the figure 4.22 not only the polymer was formed inside the pores but also out of the pores which leading to cover the surface of the template and formation of the compact and dense layer of polymer.

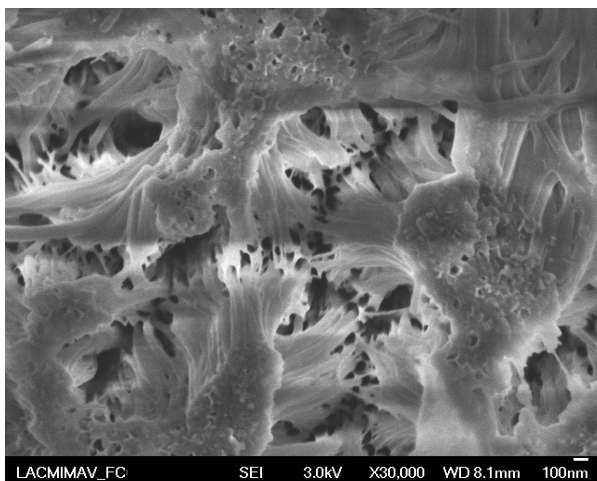


*Fig 4.22(a)*

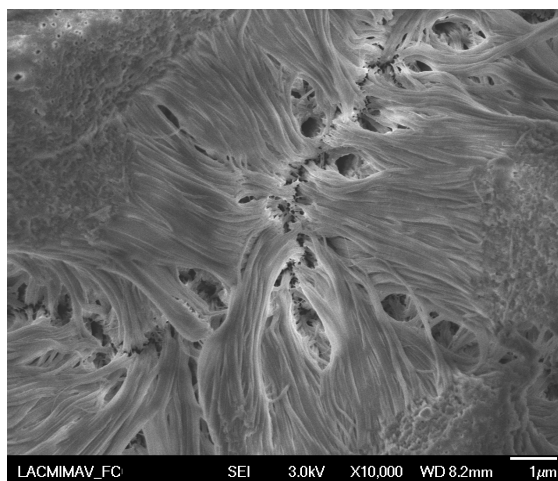


*Fig 4.22(b)*



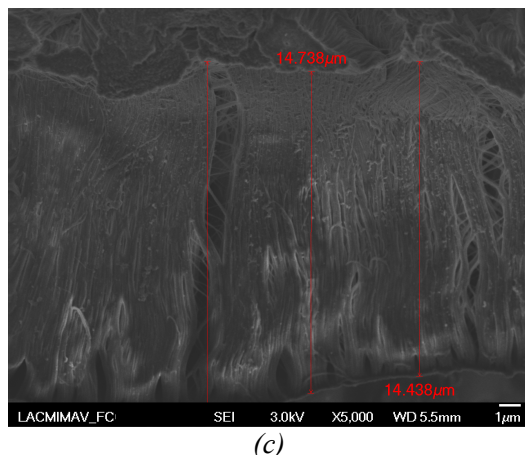


Fig 4.22 Electropolymerization of P3HT from 50 mM 3HT monomer in 0.1 M TBAPF<sub>6</sub>, at 2 V for 300 seconds. Pt wire, Ag/AgCl and 7 µm AAO template were CE, RE and WE respectively. (a) the polymers inside and out of the channels without template removing, (b) how large the polymers are by going out from the channels and laying down on AAO surface, (c) side view of the polymeric rods after template removing in 1 M NaOH solution

For the next experiment, the time was shortened to 100 seconds. The same experimental conditions i.e. 50 mM of 3HT monomer in 0.1 M TBAPF<sub>6</sub>, Ag/AgCl, Pt wire and 7 µm AAO template were electrolyte, reference electrode, counter electrode and working electrode respectively. Like the previous case the applied voltage was fixed at 2 V. As it can be seen from the image 4.23 the polymeric rods were formed inside the AAO pores. Compared to the previous case, the rods are shorter and they reached the longitude of approximately 6 µm.

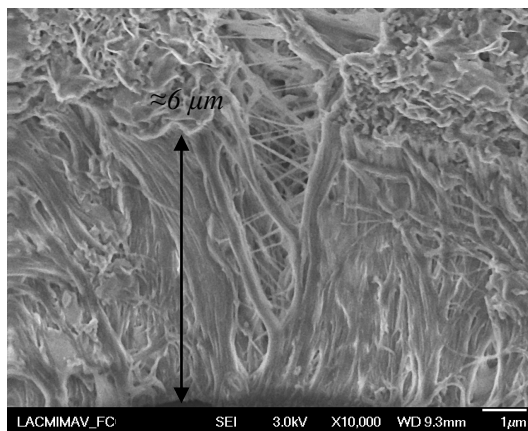
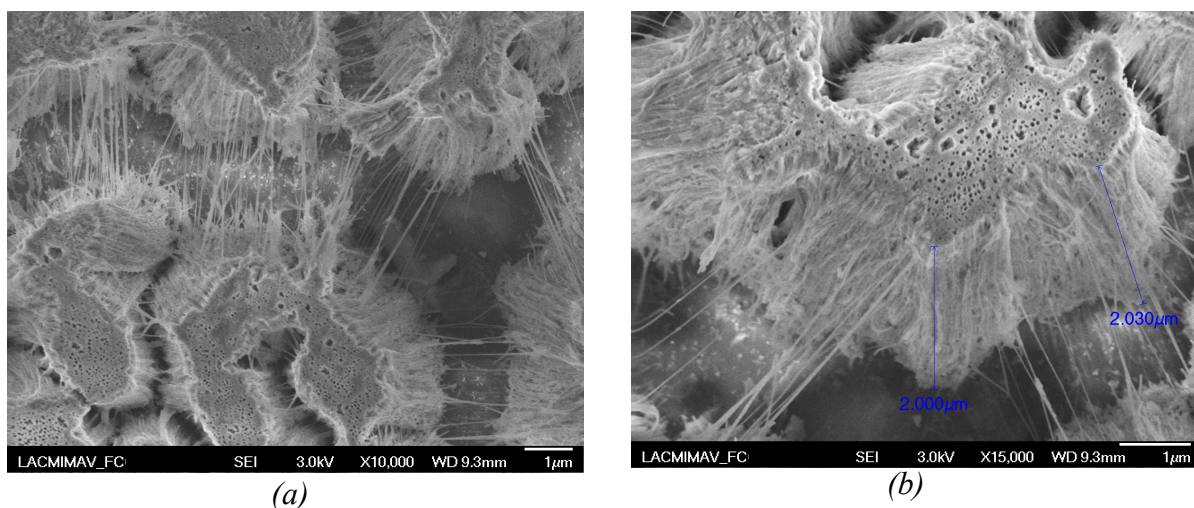


Fig 4.23 Electropolymerization of P3HT from 50 mM 3HT monomer in 0.1 M TBAPF<sub>6</sub>, at 2 V for 100 seconds. Pt wire, Ag/AgCl and 7 µm AAO template were CE, RE and WE respectively. The image is after removal of the template in 1M NaOH solution

However as it can be concluded from the image 4.23 the real longitude is more than 6  $\mu\text{m}$  because the rods are not well aligned and perpendicular to the substrate and there is a polymeric layer on the surface. Due to their inclination, the longitude is more than the template thickness and it indicates that still the rate of polymer growth is fast even if the time was decreased 3 times.

Again the electropolymerization time reduced to 30 seconds under the same experimental conditions. Figure 4.24 (a) shows the SEM image of the polymeric rods after removing the template. In this case also the template thickness was 7 micrometers. As it can be seen from the SEM image, the polymeric rods were formed just inside the channels of AAO template without the polymeric layer formation on the surface and out of the template channels. It means that the electropolymerization time could be controlled. In this case it was not possible to measure the longitude of the rods since the image 4.24 (a) is the up view of the polymer. From the figure 4.24 (b), the thickness measured to be 2  $\mu\text{m}$ , but it is not the real value due to the view of the image. The longitude of rods may be estimated between 4 -5 micrometers.

As mentioned before, the manipulating of the template with the thickness less than 5  $\mu\text{m}$  is so hard due to the brittle and fragile ceramic nature of the template. That's why in previous cases the template with 7 micrometers was fabricated.



*Fig 4.24 Electropolymerization of P3HT from 50 mM 3HT monomer in 0.1 M TBAPF<sub>6</sub>, at 2 V for 30 seconds. Pt wire, Ag/AgCl and 7  $\mu\text{m}$  AAO template were CE, RE and WE respectively. (a) and (b) both up views, (b) showing the longitude of the polymer rods. The image is after removal of the template in 1M NaOH solution*

To see how successful was the study of the polymerization time and template thickness, the template with thickness of approximately 3 micrometers was fabricated and after making it conductive (part 3.1.7), it was connected to the working electrode in three-electrode cell with Pt wire and Ag/AgCl as counter and reference electrodes. The 0.1 M TBAPF<sub>6</sub> in acetonitrile containing 50 mM of monomer (3HT) was placed inside the cell. The voltage of 2 V was applied and the electropolymerization time was adjusted for 15 seconds.

Figure 4.25 corresponds to SEM image of P3HT nanorods inside the AAO channels after partially dissolution of the template in 1 M NaOH solution. Figure 4.25 (a) shows the large-scale production of P3HT rods. After partial removing of the template, the polymer can be seen inside the pores of the template. Figure 4.25 (b) is the higher magnification of image 4.25 (a) and showing the polymer inside the channels and forming from the pore bottom not pore wall.

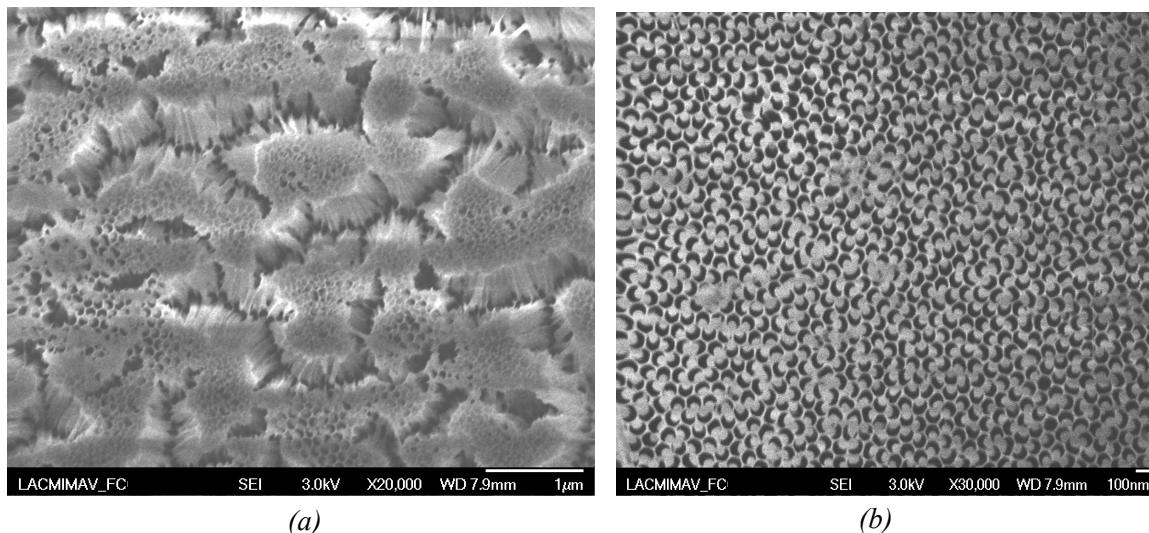


*Fig 4.25 Electropolymerization of P3HT from 50 mM 3HT monomer in 0.1 M TBAPF<sub>6</sub>, at 2 V for 15 seconds. Pt wire, Ag/AgCl and 3 µm AAO template were CE, RE and WE respectively. (a) large-scale image and (b) higher magnification. The image is after partially removal of the template in 1M NaOH solution*

#### **4.4.2 Morphology of P3HT nanostructures**

To observe the morphology of polymer nanostructures, the monomer concentration was changed at fixed electropolymerization time. In previous part the polymer rods were formed in 50 mM of monomer concentration.

To see the effect of monomer concentration the electrochemical polymerization was conducted at 2V vs. Ag/AgCl and Pt wire as counter electrode. The working electrode was AAO template with approximately 3 micrometer of thickness. The monomer (3HT) concentrations were changed in 5 mM, 15 mM and 30 mM during 15 seconds. Figure 4.26 shows the current-time curve for each experiment. At the beginning of the reaction, the current density was in its higher value for all cases. As time passes, the current density decreased due to the formation of the thicker polymeric layer. When the current density reached the plateau, it means that the AAO channels were filled by polymer. For more concentration of monomer, the current density was lower due to the more resistivity of the monomer-contained solution. The morphology of the polymer with different monomer concentration is shown in figure 4.27 (a) to (c).

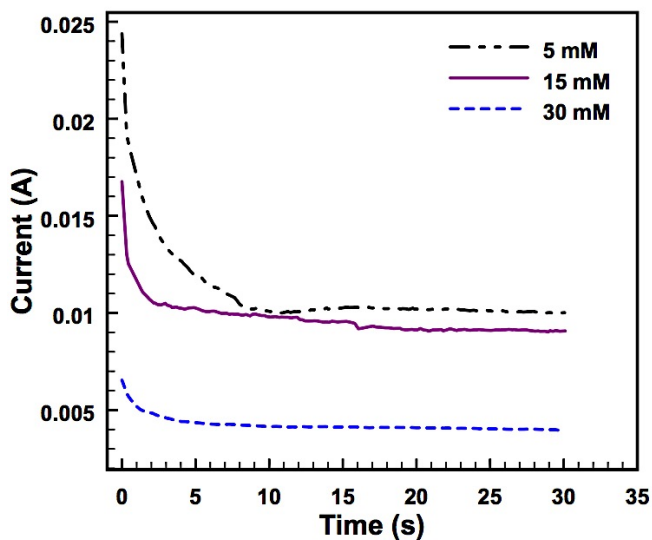


Fig 4.26 Current vs. time for electropolymerization of P3HT in different monomer concentrations of 5 mM, 15 mM and 30 mM during 100 seconds of deposition

After the electropolymerization the AAO template was dissolved partially in 1M NaOH solution. The monomer concentration is an important parameter in the synthesis of the polymer. When the monomer concentration was low (figure 4.27 (a)), the completely hollow nanotubes were obtained. Low monomer concentration implies the filling of AAO channels from the wall. As mentioned before in figure 3.11, during the electropolymerization process, the cationic radicals are obtained through the oxidation of monomer. According to the report of Martin *et al* on electropolymerization of polypyrrole, the pore walls of AAO template are anionic in nature [211]. Thus when the

monomer concentration is low, the electrostatic interaction between the template pore wall and polymeric chains results in the formation of the polymer nanotubes from the walls of the template. The pores of the template can be filled partially by increasing the monomer concentration (figure 4.27 (b)), and formation of polymer nanotubes with thicker walls. As it can be seen from images 4.27 (a) and (b), the nanotubes of polymer tend to be pushed towards together and collapse.

Unlike the metal, the polymer is not rigid and due to the high surface tension between the P3HT thin walls, they tend to join together. The walls of nanotubes are too thin to maintain the upright structure.

When a higher monomer concentration is used (figure 4.27 (c)), the nanorods of P3HT were obtained. In this case because of sufficient monomer concentration, the polymer nucleation and growth take place at the pore bottom and filling the channels from the bottom to the top of the pores resulting in rods formation.

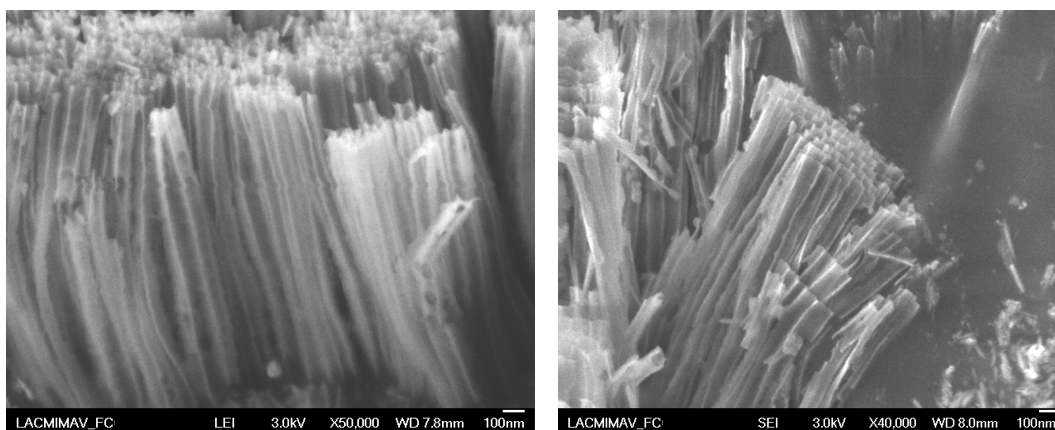


*Fig 4.27 (a) SEM image of P3HT nanotubes, electropolymerization: at 2V, 15 seconds and 5mM of monomer in 0.1 M solution of TBAPF<sub>6</sub> in acetonitrile*

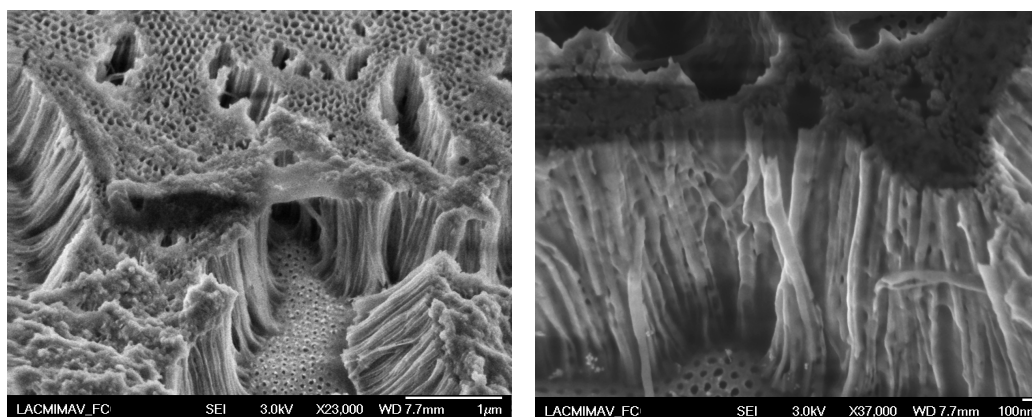


*Fig 4.27 (b) SEM image of P3HT partially filled nanotubes, electropolymerization: at 2V, 15 seconds and 15mM of monomer in 0.1 M solution of TBAPF<sub>6</sub> in acetonitrile*

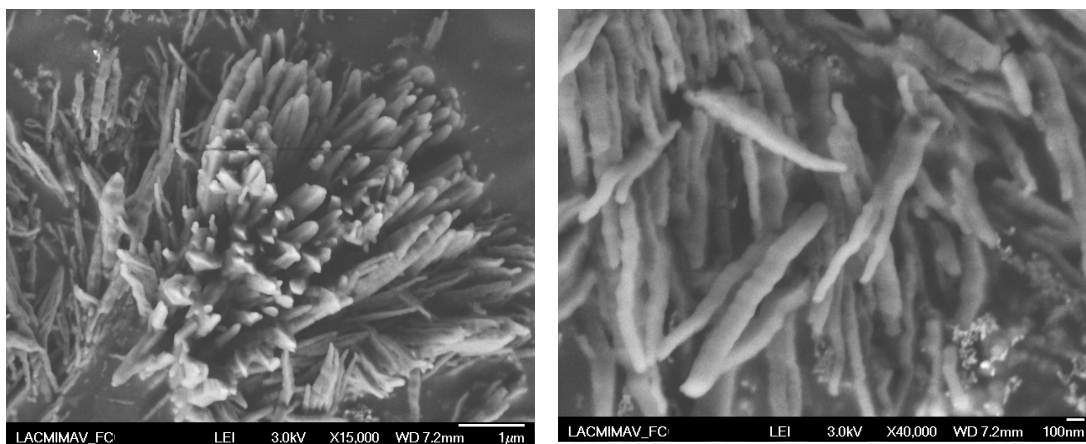


Fig 4.27 (c) SEM image of P3HT nanotubes, electropolymerization: at 2V, 15 seconds and 30mM of monomer in 0.1 M solution of TBAPF<sub>6</sub> in acetonitrile

Figure 4.28 shows the growth mechanism of polymer inside the pores of AAO template which explained above that how by changing the concentration the growth mechanism for polymer and its morphology was changed.

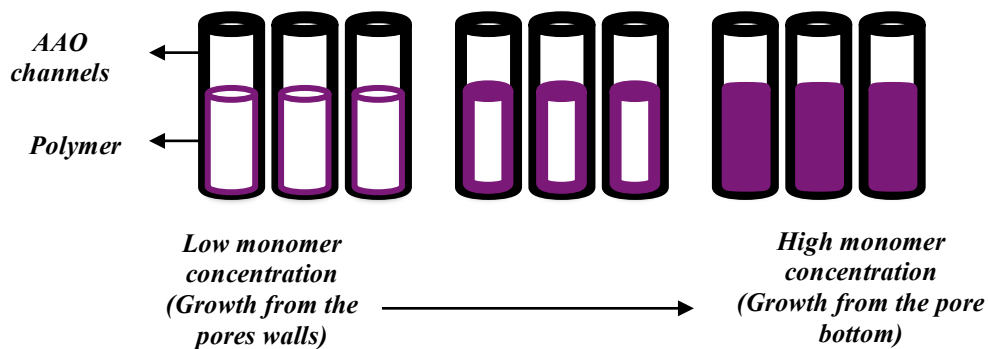


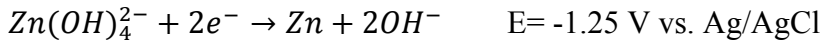
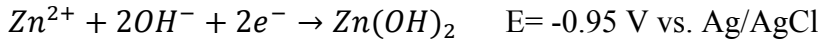
Fig 4.28 Schematic view of polymer growth mechanism inside of AAO channels

#### 4.5 Zinc oxide synthesis

In part 3.3 the electrodeposition of zinc oxide was explained in details. Here the results for ZnO film on ITO and AAO template will be discussed.

##### 4.5.1 Electrochemical study of ZnO deposition

To determine the oxidation/ reduction potential for ZnO in zinc nitrate solution, the CV was carried out from -1.5 V to -0.2 V with 50 mV/s scan rate and for 5 cycles. Figure 4.29 shows the cyclic voltammogram for zinc oxide deposition on ITO. According to the current-voltage curve, the cathodic sweep exhibited two cathodic peaks, one around -1.25 and the other in -0.95 V versus Ag/AgCl. These peaks were corresponded to following reaction during the formation of zinc oxide:



The formation of zinc hydroxide at -0.95 V was due to the reaction of  $\text{Zn}^{2+}$  cations from nitrate solution with  $\text{OH}^-$ . Conversion of  $\text{Zn}(\text{OH})_2$  to ZnO took place under heat treatment at  $70^\circ\text{C}$ . If the reaction takes place at -0.95V, the product is zinc hydroxide which converts to zinc oxide under temperature. IF the -1.25 V applies, the product will be metallic zinc. For this reason in deposition of zinc oxide under constant voltage, the voltage of -0.95 was selected.

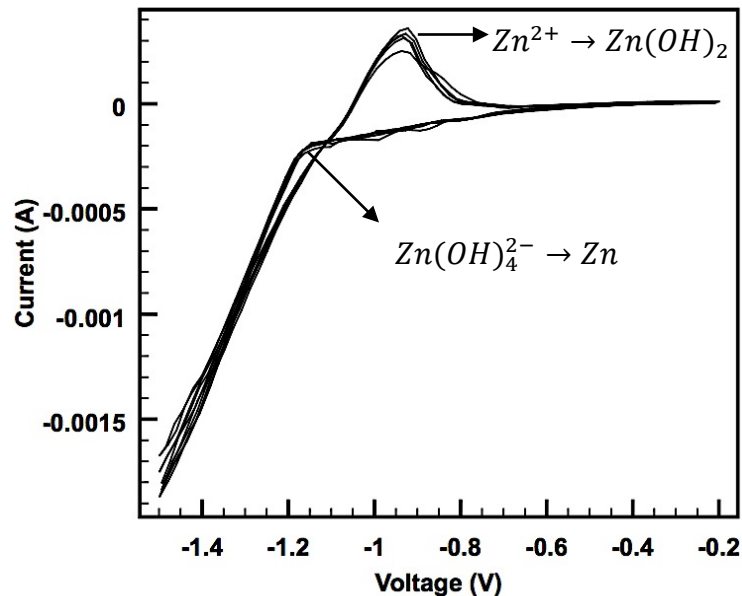


Figure 4.29 Cyclic voltammetry for ZnO deposition on ITO from 0.05M zinc nitrate solution at  $70^\circ\text{C}$ ; voltage range -1.5 to -0.2 V vs Ag/AgCl, counter electrode: Pt wire, scan rate: 50 mV/s, 5 cycles

#### 4.5.2 Bandgap calculation for electrodeposited Zinc oxide on ITO

The zinc oxide was synthesized in three-electrode cell consisting of Ag/AgCl, Pt wire and ITO substrate as RE, CE and WE respectively. The solution of zinc nitrate with 0.05M of concentration was placed inside the cell. The temperature was kept at 70 °C and the voltage at -0.95 V vs. Ag/AgCl. The experiment was done during 300 s.

The ZnO film on ITO was replaced in Uv-vis spectrometer and the transmittance vs. wavelength spectra was obtained. By profilometer the thickness of the zinc oxide layer was measured which was 770 nm approximately. With this information the direct optical band gap of zinc oxide obtained from extrapolation of the straight line in  $(\alpha hv)^2$  vs.  $hv$  plot with the x axis which was 3.1 eV and in a good agreement with other references. Figure 4.30 (a) shows the Tauc plot for electrodeposited ZnO and figure 4.30 (b) represents the transmittance vs. wavelength in which the data was collected.

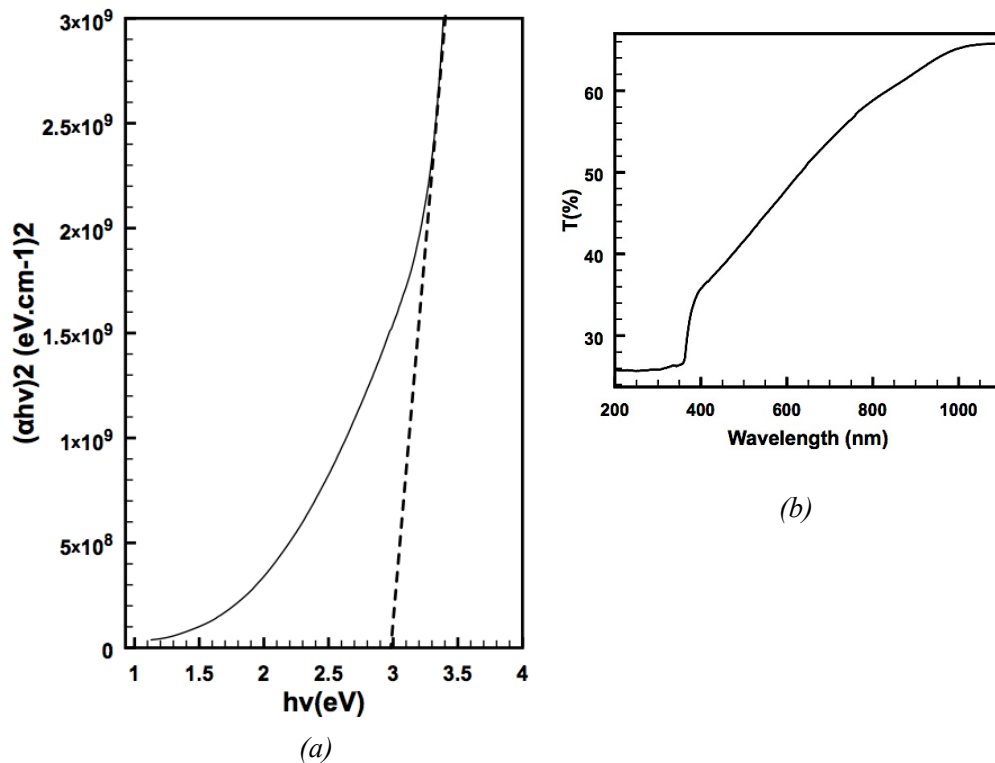


Fig 4.30 (a) Tauc plot:  $(\alpha hv)^2$  vs.  $hv$  extrapolated to zero absorbance for electrodeposited ZnO, the data was collected from (b) transmittance vs. wavelength



### 4.5.3 Zinc oxide deposition into the pores of AAO template

For deposition of zinc oxide the concentration of zinc nitrate solution and the bath temperature are important factors. There are many reports on zinc oxide electrodeposition at different temperature in the range of 65 to 90 °C and the bath concentration between  $5 \times 10^{-4}$  to  $5 \times 10^{-1}$ . In our case by changing the temperature and concentration different morphology of ZnO nanostructures were obtained till finding the conditions for growth of zinc oxide nanorods. The solution temperature of 70 and 80 °C and the concentration of 0.05 M and 0.005 M were examined.

First the  $\text{Zn}(\text{NO}_3)_2 \cdot 6\text{H}_2\text{O}$  solution with the concentration of 0.05 was replaced in three-electrode cell with AAO template, Pt wire and Ag/AgCl as working, counter and reference electrodes. The temperature was kept at 70 °C. The voltage of -0.95 V vs. RE was applied and the electrodeposition carried out for 1800 seconds. The SEM image 4.31 shows the formation of zinc oxide in form of plates. The zinc oxide was not formed inside the template pores and these plates of zinc oxide were formed on the surface of the AAO template.

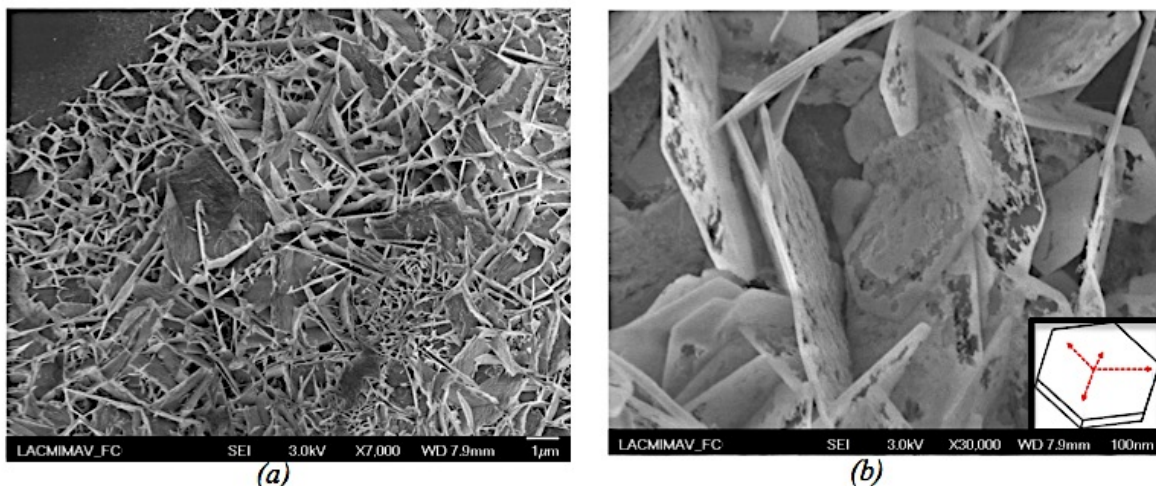
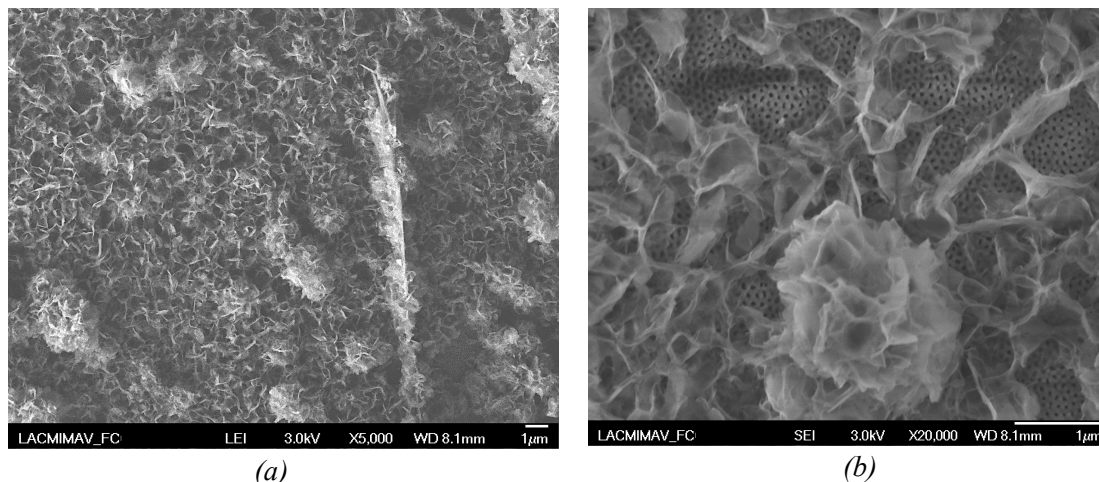


Fig 4.31 SEM image of electrodeposited ZnO from 0.05 M  $\text{Zn}(\text{NO}_3)_2 \cdot 6\text{H}_2\text{O}$  solution, at -0.95 V and 70 °C and for 1800 seconds.

Perhaps the formation of hexagonal plates is due to high concentration of zinc-contained solution. Thus in next experiment the concentration was decrease to 0.005 M. The same experimental conditions were applied. The zinc oxide obtained in these experimental conditions was shown in figure 4.32 In this case also the ZnO was not

formed inside the AAO channels and the flower-like zinc oxide was observed. Image (b) is the higher magnification of image (a). As it can be seen from image (a) the zinc oxide was formed on the surface of the template. It seems that by decreasing the solution concentration and without changing other parameters the morphology of ZnO was changed. For less concentration the electrodeposited zinc oxide was thinner (figure 4.32 (b)) than when using more concentrated solution (figure 4.31 (b)).



*Fig 4.32 SEM image of electrodeposited ZnO from 0.005 M  $Zn(NO_3)_2 \cdot 6H_2O$  solution, at -0.95 V and 70 °C and for 1800 seconds.*

Thus for the next experiment the concentration was fixed at 0.005 M and the solution temperature raised to 80 °C. Other experimental parameters were as following; the applied voltage of -0.95 V, the counter, reference and working electrodes were Pt wire, Ag/AgCl and AAO template respectively. In this case the depositions carried out for 900 seconds. The result is shown in figure 4.33. From the figure 4.31, it can be understood that by increasing the temperature from 70 to 80 °C at fixed monomer concentration, the vertical ZnO nanostructures were obtained and contrary to the previous experiments the plates or the film of zinc oxide on the template surface were not formed. Figure 4.33 (b) is the higher magnification of figure 4.33 (a) where the morphology of the obtained zinc oxide can be seen clearly. The diameter of rod-shape zinc oxide was not uniform and was higher than diameter of the template pores which was between 50-60 nm.

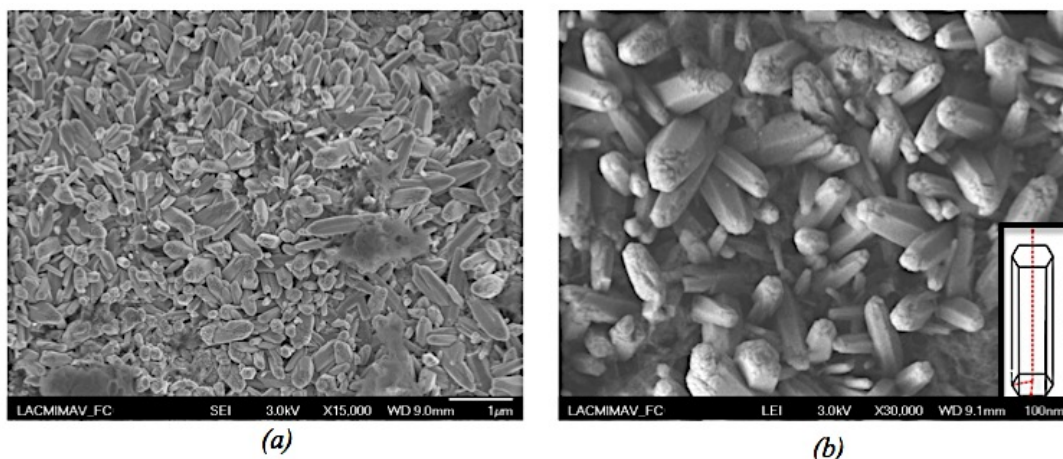


Fig 4.33 SEM image of electrodeposited ZnO from 0.005M  $Zn(NO_3)_2 \cdot 6H_2O$  solution at -0.95V, 80 °C and for 900 seconds

We did another experiments by decreasing the deposition time to 300 seconds. The solution concentration and temperature were 0.005 M and 80 °C and other experimental parameters were not changed. Figure 4.34 shows the ZnO nanostructures obtaining under these experimental conditions.

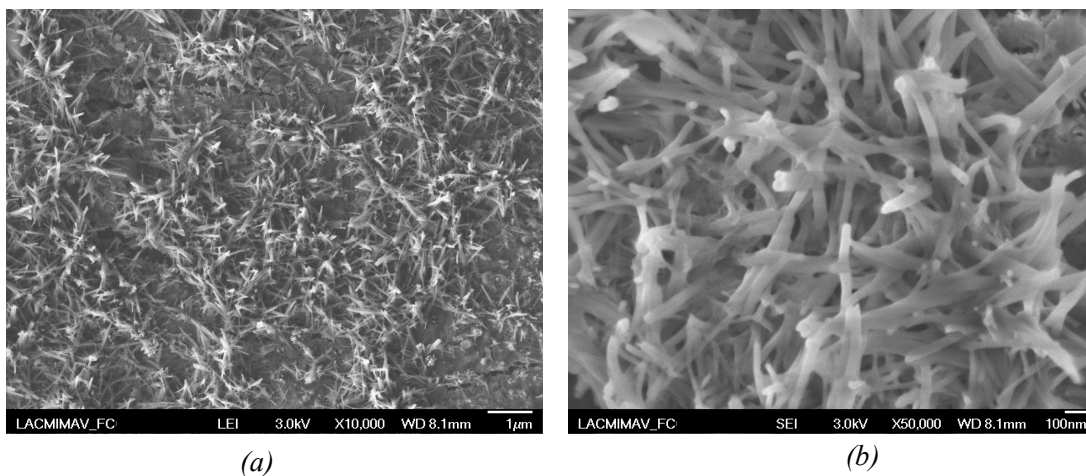


Fig 4. 34 SEM image of electrodeposited ZnO from 0.005 M  $Zn(NO_3)_2 \cdot 6H_2O$  solution, at -0.95 V and 80 °C and for 300 seconds after template removal in NaOH 1 M

#### ***4.6 Combination of P3HT and ZnO to fabricate hybrid active material***

After optimization the experimental conditions for template, polymer and ZnO synthesis, the active layer for hybrid solar cell was fabricated in a template with 2  $\mu\text{m}$  of thickness and average pore size of 50 nm. The polymer was electrodeposited inside the channels of template from the solution containing 30 mM of monomer and 0.1M tetrabutylammonium hexafluorophosphate in acetonitrile at 2 V vs. Ag/AgCl for 15 seconds. The sample was washed several times with acetonitrile and dried at ambient temperature. Then this composite contacting template and polymeric rods was immersed in solution of NaOH (0.5M) to dissolve the template and releasing the polymeric rods which were vertically aligned on the aluminum substrate. The next step was electrodeposition of zinc oxide from the solution containing 0.005M zinc nitrate, at -1 V vs. Ag/AgCl and 80  $^{\circ}\text{C}$  for 10 minutes. The sample after this step was rinsed several times in distilled water and dried at ambient temperature for future characterization.

##### ***4.6.1 Hybrid materials - Reflectance***

Since the hybrid active layer (P3HT+ZnO) were synthesized on aluminum substrate, to see the absorption of the material, reflectance spectra was reported for this mixture in the range of 1100 to 200 nm of wavelength.

Radiant flux incident upon a surface or medium undergoes transmission, reflection and absorption. Application of conservation of energy leads to the statement that the sum of the transmission, reflection and absorption of the incident flux is equal to unity or [212]:

$$\alpha(\lambda) + \tau(\lambda) + \rho(\lambda) = 1 \quad (4.15)$$

in which  $\alpha$  is absorption,  $\tau$  is transmission,  $\rho$  is reflection and  $\lambda$  in wavelength.

In our case because the aluminum metal support cannot transmit the light therefore the absorption mas reflection equals to unity as below:

$$\alpha(\lambda) = 1 - \rho(\lambda) \quad (4.16)$$

Figure 4.35 shows the reflectance spectra for template, ZnO, P3HT and mixture of P3HT and ZnO. As it can be observed from the figure, the hybrid material reached to the

less reflectance compared to ZnO and template separately, which indicated the higher absorption of light by hybrid materials according to formula 4.16.

In addition for hybrid materials, the materials showed a decrease in reflection at almost 800 nm of wavelength which indicated that the hybrid material could absorb the light at higher wavelength compared to each material separately.

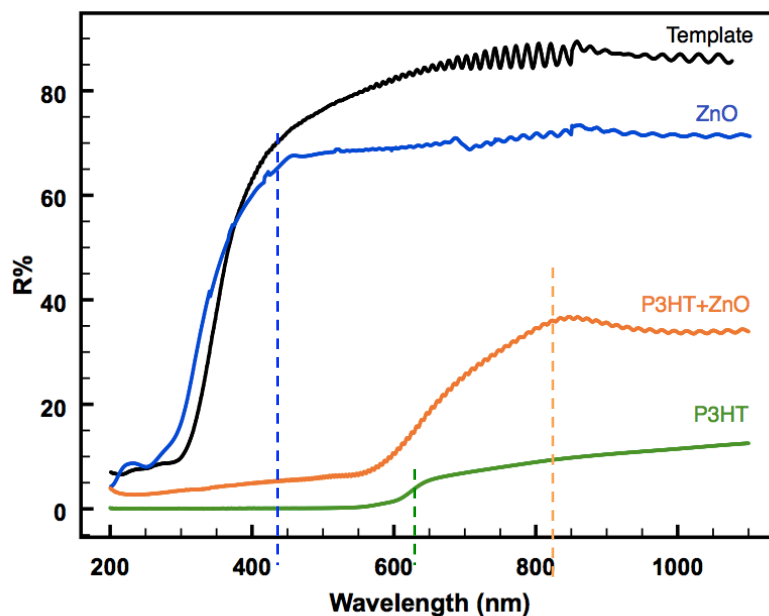


Fig 4.35 Reflectance spectra for template, ZnO, P3HT and mixture of P3HT and ZnO

The reflectance spectra showed approximately 40% of reflection at high wavelength. The reflection decreased by decreasing the wavelength following by reaching to almost zero reflection in the wavelength range of visible light.

#### 4.6.2 Hybrid materials - Photoluminescence

Figure 4.36 shows the PL spectra for polymer, zinc oxide, template and mixture of P3HT and zinc oxide, all performed with excitation wavelength centered at 375 nm.

As it can be observed from the figure, hybrid materials showed light emission at 536 nm of wavelength at the same wavelength value for P3HT itself and higher wavelength value for zinc oxide itself.

It is clear the influence of the combination of both materials in the luminescent properties of each material separately, where the signal for hybrid materials appears at the

same wavelength than the polymer itself by remarkable increase in the PL intensity. This suggested that the interaction between the polymer matrix and zinc oxide nanorods allows the charge transport along the hybrid film that is important for solar cell application.

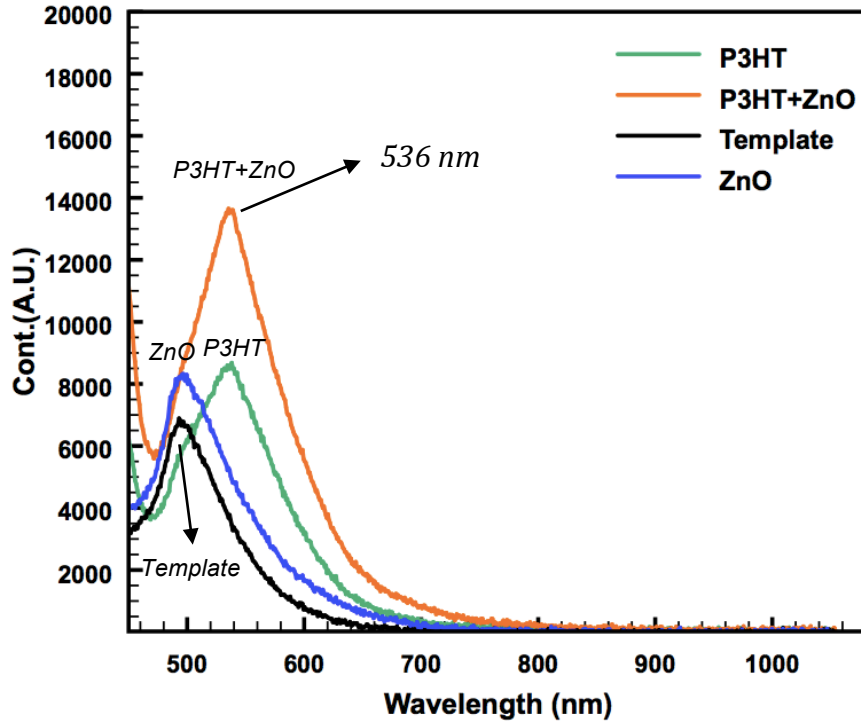


Fig 4.36 PL spectra for template, ZnO, P3HT and mixture of P3HT and ZnO

#### 4.7 Summary

Anodization, a self-ordering technique for creating nano-channels in alumina, is a simple and cheap method for creating highly ordered nanoporous film. The dimensions of the nanochannels, including pore diameter and pore depth can be controlled accurately through appropriate anodization conditions.

In this thesis we discussed the fabrication of anodic aluminum oxide with controlling the experimental conditions to reach the optimum parameters and suitable template in our case. By carrying out many experiments with different experimental conditions, we could reach the fixed procedure to fabricate this kind of template. We examined the suitability of porous alumina as a supporting substrate for creating a

textured polymer and metal oxide semiconducting nanofilm to be used as a hybrid material in solar cell application.

We discussed different experimental conditions such as monomer concentration and time of deposition for polymer growth inside the nano-channels of AAO. Also we investigated on morphology and growth of zinc oxide inside the pores of anodic aluminum oxide template by varying the parameters such as bath concentration, bath temperature and time of deposition.

We fabricated the hybrid materials by using the optimum experimental conditions in each step and we showed the potential application of this hybrid film in solar cell application.

Chapter 5  
*Conclusions*



In this chapter the conclusion of our experiments, and the future work will be introduced.

## 5.1 Conclusions

- 1- Suitable anodic oxide template was obtained under changing different experimental conditions. In our case the template with pore diameter of 40-50 nm, inter-pore distance of 100 nm, pore density of 96 pore/ $\mu\text{m}^2$  and thickness of 2 $\mu\text{m}$  was fabricated by first anodization for 2 hours, etching for 40 min and second anodization of 10 min. Under our experiments the growth rate of alumina layer was 1.1 nm per second. Knowing this value allowed us to control the thickness of the template by changing the second anodization time.
- 2- Poly (3-hexylthiophene) film was synthesized by two methods of chemical oxidative polymerization and electropolymerization on ITO substrate. FT-IR spectra confirmed the existence of polymer functional group such as C=C, C-C and C-S in polymeric chain for both cases. The product of chemically synthesis polymer was a mixture of a black powder and dense layer of the polymer which was brittle. The product of electrochemical synthesis was a uniform film on ITO which could be separated easily and without damage from the substrate.
- 3- By comparing the structural and optoelectrical properties of the P3HT obtained from two mentioned methods, we concluded that P3HT obtained from electrochemical polymerization has showed better crystallinity in its structure, adsorption in higher wavelength and higher electrical conductivity almost 3000 times more.
- 4- These better properties were due to the more crystallinity of the electrochemical synthesized polymer. In general the polymer is amorphous but the type of dopant can effect on steric repulsion between two thiophene adjacent rings and makes it more ordered or disordered. In the case of electrochemically synthesized polymer,

the dopant was  $\text{PF}_6^-$  and for the chemically synthesized polymer was  $\text{Fe}^{+3}$  which caused the repulsion between the thiophene rings and the distortion in its structure.

- 5- Besides of better structural and optoelectrical properties for electrochemically synthesized polymer, it must say that the electropolymerization method is more fast and time consuming method. Generally chemically synthesis of the polymer carries out for one day however by this method large-scale production of polymer is possible. In addition, electropolymerization presents several distinct advantages such as catalyst free synthesis, direct grafting of the doped conductive polymer onto the electrode surface, control of the film thickness by the deposition charge and the possibility of in-situ electrochemical characterization during the growth process.
- 6- The HOMO-LUMO and band gap levels of energy were calculated for the electrochemically synthesized polymer which was -5.04, 3.14 and 1.95 eV respectively from the cyclic voltammetry and Tauc plot. These values could help us to sketch the energy levels for our materials.
- 7- By studying the cyclic voltammetry curve for P3HT, the potential of 2V vs. Ag/AgCl was selected for potentiostatic deposition of polymer. CV measurement for electropolymerization of P3HT carried out in wider range of potential from -0.1 V to 3 V. In this CV curve an oxidation peak was observed at 2.5 V and the inset of oxidation was at 2V. It was concluded that at constant potential, the polymer is deposited between 2 and 2.5 V. Polymer deposited higher than 2.5V had not good adhesion to ITO surface.
- 8- P3HT was synthesized electrochemically from its monomer (3HT) inside the pores of fabricated AAO template. By changing the monomer concentration, the morphology of vertically-aligned polymers was changed. At lower monomer concentration the growth mechanism was from the pore walls, by increasing the monomer concentration, the pores were filled from the bottom. Depending on

desired morphology, i.e nanotubes or nanorods of the polymer, the monomer concentration can be changed. This information helped us to choose the proper monomer concentration to have the P3HT nanorods.

- 9- By changing the deposition time, the length of the polymeric tubes or rods was changed. The growth rate of electropolymerization was high enough that with 300 seconds of electropolymerization, the rods with longitude of 14  $\mu\text{m}$  were obtained. Decreasing the deposition time to 15 second resulted in obtaining the P3HT rods with approximately 2  $\mu\text{m}$  of longitude.
- 10- Zinc oxide was electrodeposited on ITO by cyclic voltammetry method to study its deposition potential. From the oxidation peak in CV curve, it was concluded that ZnO could be electrodeposited at -0.95V vs. Ag/AgCl reference electrode.
- 11- By measuring the adsorption spectra for the zinc oxide film and from the Tauc plot, the band gap of 3.1 eV was calculated for the ZnO films which was in good agreement with the reported values [213, 214].
- 12- Zinc oxide was electrodeposited into the channels of AAO template. The experiments carried out at different concentration of zinc nitrate solution, temperature and deposition time. When the solution concentration was high, obtained zinc oxide had the morphology of plates laying on the surface of the template. These hexagonal plates were thick and dense. By decreasing the solution concentration, the flower-like ZnO was obtained still on the surface of the template not inside the channels. This flower-like zinc oxide was less dense and thick compared to the zinc plates. Thus we did not change the concentration and we increased the temperature to 80  $^{\circ}\text{C}$ . This time the hexagonal pillar of zinc oxide were obtained. However they reached the diameter of approximately 200 nm. Thus we decreased the deposition time to obtain the ZnO rods with the proper diameter and longitude.

- 13- From the previous experiments the concluded optimum conditions were applied to synthesis the hybrid materials P3HT and ZnO inside the channels of AAO 2  $\mu\text{m}$ -template with average pore diameter of 50 nm. P3HT from 30 mM monomer solution, at 2V vs. Ag/AgCl and for 15 seconds and ZnO from 0.005 M zinc nitrate solution, at 80  $^{\circ}\text{C}$  and -0.95V vs. Ag/AgCl.
- 14- The reflectance spectra showed more than 40 % of reflectance for mixture of two materials compared with each materials separately. This indicates the higher adsorption of light for the mixture of polymer and zinc oxide. Also in the case of both materials together, the reflectance reduced at higher wavelength comparing with the spectra of AAO or ZnO, showing more absorption by the hybrid materials at higher wavelength.
- 15- The photoluminescence spectra showed a peak for hybrid materials at higher wavelength showing the higher luminescence by hybrid materials compared to each materials showing its potential application as hybrid materials for hybrid solar cells.

## REFERENCES

- 
- [1] A. Zuttel, & A. Borgschulte, A (2008). “*Hydrogen as a Future Energy Carrier*”. WILEY-VCH Verlag GmbH & Co. KGaA, Weinheim
- [2] <http://www.eia.gov/forecasts/ieo/index.cfm>
- [3] Natural Resources and the Environment-Dot Earth Blog:  
<http://dotearth.blogs.nytimes.com/2009/04/21/atmospheric-co2-and-methane-still-building/>
- [4] M.F.Ashby, P.G.Ferreira and D.L. Schodek. “*Nanomaterials, Nanotechnologies and Design: An Introduction for Engineers and architects*” (2009)
- [5] G.Cao, Y.Wang. “*Nanostructures and Nanomaterials: Synthesis, Properties, and Applications*”, (2004)
- [6] P. Schmuki, S.Virtanen, “*Electrochemistry at the Nanoscale*”. Springer science (2011).
- [7] M. K. Sanyal, A. Datta, and S. Hazra. “*Morphology of nanostructure materials*”. *Pure Appl. Chem* (2002) 74:1553–1570
- [8] H. Weller, A. Angew. “*Colloidal Semiconductor Q-Particles: Chemistry in the Transition Region Between Solid State and Molecules*”. *chem.Int. Engl* (1993) 32:41-53
- [9] M. L. Steigerwald, L. E. Brus.” *Semiconductor crystallites: a class of large molecules*”. *Acc. Chem. Res* (1990) 23 (6): 183–188
- [10] A.P. Alivisatos. “Semiconductor clusters, nanocrystals, and quantum dots”. *Science* (1996) 271(5251):933-937
- [11] S. Empedocles, M. Bawendi.”Spectroscopy of single CdSe nanocrystallites”. *Acc. Chem. Res* (1999) 32 (5):389-396
- [12] J. Murphy, J. Coffey, L. Jeffery. “*Quantum Dots: A Primer*”. *Applied Spectroscopy* (2002) 56: 9A-36A
- [13] A.Tiwari, A.Mishra, H.Kobayashi and A.P.F.Turner.”*Intelligent Nanomaterials*”. Wiley & Scrivener (2012).
- [14] D. Vollath. “*Nanomaterials: an introduction to synthesis, properties and applications*”. WILEY-VCH (2008)
- [15] <http://www.ecosolarly.com/products/lotus-series>
- [16] I. Chung, B. Lee, J. He, R.P. H. Chang, M. G. Kanatzidis. ”All-solid-state dye-sensitized solar cells with high efficiency”. *Nature* (2012) 485:4886-489
- [17] S.J.Fonash. “*Solar cell device physics*”. 2<sup>nd</sup> ed. USA: Academic Press (2010)
- [18] S.M. Sez, K.N. Kwok.” *Physics of semiconductor devices*”. Third edition. Wiley (2006)
- [19] T.Soga. “ *Nanostructured materials for solar cell conversion*”. 1th ed. NL: Elsevier (2006)
- [20] B. G. Yacobi.”*Semiconductor materials, an introduction to basic principles*”. Kluwer academic publisher (2003)
- [21] <http://www.astm.org/Standard/>
- [22] A. Luque, S. Hegedus.” *Handbook of Photovoltaic Science and Engineering*”. Wiley (2003)
- [23] B.R. Saunders, M.L. Turner. “*Nanoparticle-polymer photovoltaic cells*”. *Adv in Colloid & Interface Science* (2008) 138: 1-23
- [24] B. P. Nguyen, T. Kim, C. R. Park.” *Nanocomposite-based bulk heterojunction hybrid solar cells*”. *Journal of nanomaterials* (2014) 2014: 243041-243061
- [25] W. U. Huynh, J. J. Dittmer, N. Tecler, D. J. Milliron, A. P. Alivisatos.” *Charge transport in hybrid nanorod-polymer composite photovoltaic cells*”. *Physical Review B* (2003) 67:115326-12
- [26] A. McEvoy, T. Markvart, L. Castañer. “*Solar cells: materials, manufacture and operation*”. Elsevier. Second edition (2013)
- [27] A.Goetzberger, J.Luther, G.Willeke. “*Solar cells: past, present, future*”. *solar energy materials & solar cells* (2002) 74:1-11
- [28] A.Goetzberger, Ch.Hebling.” *Photovoltaic Materials & Solar Cells*”. *Solar energy materials & solar cells* (2000) 26: 1-19

- [29] R. Rhodes, Sh. Asghar, R. Krakow, M. Horie, Z. Wang, M.L. Turner, B. R. Saunders.” *Hybrid polymer solar cells: From the role colloid science could play in bringing deployment closer to a study of factors affecting the stability of non-aqueous ZnO dispersions*”. *Colloids and Surfaces A: Physicochemical and Engineering Aspects* (2009) 343:50-56
- [30] M. Wright, A.Uddin.” *Organic—inorganic hybrid solar cells: A comparative review*”. *Solar Energy Materials & Solar Cells* (2012) 107: 87–111
- [31] M.Wang, X.Wang. “P3HT/ZnO bulk-heterojunction solar cell sensitized by a perylene derivative”. *Solar Energy Materials & Solar Cells* (2008) 92: 766–771
- [32] N.Ch. Das, P. E. Sokol.” *Hybrid photovoltaic devices from regioregular polythiophene and ZnO nanoparticles composites*”. *Renewable Energy* (2010) 35: 2683-2688
- [33] Sh. Lu, S.Sh. Sun, X. Jiang, J. Mao, T.Li, K. Wan.” *In situ 3-hexylthiophene polymerization onto surface of TiO<sub>2</sub> based hybrid solar cells*”. *J Mater Sci: Mater Electron* (2010) 21:682–686
- [34] K. Cheng, G. Cheng, Sh. Wang, D. Fu, B. Zou, Z. Du.” *Electron transport properties in ZnO nanowires/poly (3-hexylthiophene) hybrid nanostructure*”. *Materials Chemistry and Physics* (2010) 124:1239–1242
- [35] B. Conings, L. Baeten, H.G. Boyen, D. Spoltore, J. D’Haen, M. K. Van Bael, J. V. Manca.” *Generalized approach to the description of recombination kinetics in bulk heterojunction solar cells-extending from fully organic to hybrid solar cells*”. *Appl. Phys. Lett* (2012) 100: 203905 - 203905-5
- [36] K.Yuan, F. Li, L. Chen, Y. Chen.” *Approach to a block polymer precursor from poly(3-hexylthiophene) nitroxide-mediated in situ polymerization for stabilization of poly(3-hexylthiophene)/ZnO hybrid solar cells*”. *Thin Solid Films* (2012) 520: 6299–6306
- [37] J.Hagen, W. Schaffrath, P. Otschik, R.Fink, A.Bacher, H.W. Schmidt, D. Haarer.” *Novel hybrid solar cells consisting of inorganic nanoparticles and an organic hole transport material*”. *Synthetic metals* (1997) 89: 215-220
- [38] W. J. E. Beek, M.M. Wienk, R. A. J. Janssen.” *Efficient hybrid solar cells from zinc oxide nanoparticles and a conjugated polymer*”. *Adv. Mater* (2004) 16: 1009-1013
- [39] W. J. E. Beek, L. H. Slooff, M. M. Wienk, J. M. Kroon, R. A. J. Janssen.” *Hybrid solar cells using a zinc oxide precursor and a conjugated polymer*”. *Adv. Funct. Mater* (2005) 15:1703-1707
- [40] Y. Zhou, M. Ech, M. Kruger. “*Organic-Inorganic Hybrid Solar Cells: State of the Art, Challenges and Perspectives*”. *Solar cells- new aspects and solutions*. Intech chapter 5: 95-120
- [41] F.Krebs. “*Fabrication and processing of polymer solar cells: A review of printing and coating techniques*”. *Solar Energy Materials & Solar Cells* (2009) 93:394–412
- [42] I.Gonzalez-Valls, M. Lira-Cantu. “*Vertically-aligned nanostructures of ZnO for excitonic solar cells: a review*”. *Energy & Environmental Science*, (2008) 2:19-34
- [ 43 ] T.Zeng, H. Lo, Ch.Chang,Yu. Lin,Ch.Chen,W. FangSu.” *Hybrid poly (3-hexylthiophene)/tita-nium dioxide nanorods material for solar cell applications*”. *Solar Energy Materials & Solar Cells*. (2009) 93:952–957
- [44] J. Chandrasekaran, D. Nithyaprakash, K.B. Ajjan , S. Maruthamuthu, D. Manoharan, S. Kumar.” *Hybrid solar cell based on blending of organic and inorganic materials- An overview*”. *Renewable and Sustainable Energy Reviews* (2011) 15: 1228–1238
- [45] Z. Han, J. Zhang, X. Yang, H. Zhu, W.Cao.” *Synthesis and photoelectric property of poly (3-octylthiophene)/zinc oxide complexes*”. *Solar Energy Materials & Solar Cells* (2010) 94:194–200
- [46] C. Yu Chou, J. Sh Huang, Ch. H Wu, Ch. Lee, Ch. F Lin.” *Lengthening the polymer solidification time to improve the performance of polymer/ZnO nanorod hybrid solar cells*”. *Solar Energy Materials & Solar Cells* (2009) 93: 1608–1612
- [ 47 ] E.Arici, N.S. Sariciftci.”*Hybrid solar cells*”. *Encyclopedia of Nanoscience and Nanotechnology* (2004) 3: 29-944
- [48] W. J. E. Beek, M. M. Wienk, R. A. J. Janssen.” *Hybrid solar cells from regioregular polythiophene and ZnO nanoparticles*”. *Adv. Funct. Mater* (2006) 16: 1112–1116

- 
- [42] M. Skompska.” *Hybrid conjugated polymer/semiconductor photovoltaic cells*”. Synthetic Metals (2010) 160:1-15
- [50] M.A Green, K. Emery, Y. Hishikawa, W. Warta, E. D. Dunlop. “*Solar cell efficiency tables (version 42)*”. Progress in Photovoltaics (2013) 21: 827-837
- [51] M.C. Lechmann, D. Koll, D.Kessler, P. Theato, W. Tremel, J.S. Gutmann.” *Comparison of hybrid blends for solar cell application*”. Energies (2010) 3:301-312
- [52] M. Lira-Cantua, F.C. Krebs. “*Hybrid solar cells based on MEH-PPV and thin film semiconductor oxides (TiO<sub>2</sub>, Nb<sub>2</sub>O<sub>5</sub>, ZnO, CeO<sub>2</sub> and CeO<sub>2</sub>-TiO<sub>2</sub>): Performance improvement during long-time irradiation*”. Solar Energy Materials & Solar Cells (2006) 90: 2076–2086
- [53] J.Boucle, P. Ravirajanac, J.Nelson.” *Hybrid polymer–metal oxide thin films for photovoltaic applications*”. J. Mater. Chem (2007) 17: 3141–3153
- [54] I. Gur, N. A. Fromer, Ch. Chen, A. G. Kanaras, A. P. “*Hybrid Solar Cells with Prescribed Morphologies Based on Hyperbranched semiconductor nanocrystals*”. Nano Lett (2007) 7: 409-414
- [55] B. Conings, L. Baeten, H. Boyen, D.Spoltore, J. D’Haen, L. Grieten, P. Wagner, M.Van Bael *Influence of interface morphology onto the photovoltaic properties of nanopatterned ZnO/poly(3-hexylthiophene) hybrid solar cells. An impedance spectroscopy study*”. J.Manca. J. Phys. Chem (2011) 115: 16695–16700
- [56] H. Borchert.” *Elementary processes and limiting factors in hybrid polymer/nanoparticle solar cells*”. Energy Environ. Sci (2010) 3: 1682–1694
- [57] O. P. Dimitriev, N.A. Ogurtsov, Y. Li, A. A. Pud, G. Gigli, P. S. Smertenko, Y. P. Piryatinski, Y.V. Noskov, A. S. Kutsenko. “*Tuning of the charge and energy transfer in ternary CdSe/poly(3-methylthiophene)/poly(3-hexylthiophene) nanocomposite system*”. Colloid Polym Sci (2012) 290:1145–1156
- [58] Ti. Xu, Q. Qiao.” *Conjugated polymer–inorganic semiconductor hybrid solar cells*”. Energy & Environmental Science (2011) 4: 2700-2720
- [59] M. C. Scharber, D. Mühlbacher, M. Koppe, P. Denk, Ch. Waldauf, A.J. Heeger, Ch. J. Brabec.” *Design rules for donors in bulk-heterojunction solar cells—towards 10 % energy-conversion efficiency*”. Adv. Mater (2006) 18:789–794
- [60] X. Yang, J. Loos, S. C. Veenstra, W. J. H. Verhees, M. M. Wienk, J. M. Kroon, M. A. J. Michels, R. A. J. Janssen.” *Nanoscale morphology of high-performance polymer solar cells*”. Nano Lett. (2005) 5:579-583
- [61] Y. Zhou, M. Eck, C. Veit, B. Zimmermann, F. Rauscher, P. Niyamakom, S.Yilmaz, I.Dumsch, S.Allard, U.Scherf, M.Kruger.” *Efficiency enhancement for bulk-heterojunction hybrid solar cells based on acid treated CdSe quantum dots and low Bandgap polymer PCPDTBT*”. Solar Energy Materials and Solar Cells (2011) 95:1232–1237
- [62] Y. Liang, Z. Xu, J. Xia, S.-T. Tsai, Y. Wu, G. Li, C. Ray, L. Yu.” *For the bright future—bulk heterojunction polymer solar cells with power conversion efficiency of 7.4%*”. Advanced Materials (2010) 22:E135–E138
- [63] H. Xiang, S.H. Wei.” *Identifying optimal inorganic nanomaterials for hybrid solar cells*”. J. Phys. Chem. C (2009) 113: 18968–18972
- [64] Y. Zhou, M. Ech, M. Kruger. “*Organic-Inorganic Hybrid Solar Cells: State of the Art, Challenges and Perspectives*”. Solar cells- new aspects and solutions. Intech chapter 5: 95-120
- [65] J. Xue, B.P. Rand, Soichi Uchida, and Stephen R. Forrest.” *A hybrid planar-mixed molecular heterojunction photovoltaic cell*”. Adv. Mater (2005) 17:66-71
- [66] B. R. Saunders.” *Hybrid polymer/nanoparticle solar cells: Preparation, principles and challenges*”. Journal of Colloid and Interface Science (2012) 369: 1–15
- [67] K. Yu, J. Chen.” *Enhancing solar cell efficiencies through 1-D nanostructures*”. Nanoscale Res Lett (2009) 4:1–10

- 
- [68] G. Ca, D. Liu. “*Template-based synthesis of nanorod, nanowire, and nanotube arrays*“. *Advances in Colloid and Interface Science* (2008) 136: 45–64
- [69] S.I. Na, S. S Kim, W.K. Hong, J.W. Park, J.Jo, Y.Ch. Nah, T.Lee, D.Yu. Kim. “*Fabrication of TiO<sub>2</sub> nanotubes by using electrodeposited ZnO nanorod template and their application to hybrid solar cells*“. *Electrochimica Acta* (2008) 53: 2560–2566
- [70] R. Fathi, S. Sanjabi, N. Bayat. “*Synthesis and characterization of NiMn alloy nanowires via electrodeposition in AAO template*“. *Materials Letters* (2012) 66: 346–348
- [71] V. K. Varadan, L.Chen, J. Xi. “*Nanomedicine: Design and Applications of Magnetic Nanomaterials, Nanosensors and nanosystems*“. WILEY (2008)
- [72] M. Saka. “*Metallic micro and nano materiales: fabrication with atomic diffusion*“. Springer (2011)
- [73] Wesley V. Prescott, Arnold I. Schwartz. “*Nanorods, Nanotubes, and Nanomaterials Research Progress*“. Nova science (2008)
- [74] R. Xiao.” *Controlled electrochemical synthesis of conductive polymer nanostructures*“. *Journal of American chemical society* (2007) 129:4483-4489
- [75] A.Thomas, F. Goettmann, M. Antonietti. “*Hard Templates for soft materials: Creating nanostructured organic materials*“. *Chem. Mater* (2008) 20: 738-755
- [76] R. Xu, W. Pang, Q. Huo. “*Modern Inorganic Synthetic Chemistry*“. Elsevier (2011)
- [77] Y.Zhao, M.Chen, Y. Zhang, T.Xu, W. Liu. “*A facile approach to formation of through-hole porous anodic aluminum oxide film*“. *Materials Letters* (2005) 59: 40–43
- [78] A. Santos, L. Vojkuvka, J. Pallarés, J. Ferré-Borrull, L.F. Marsal. “*Nanoporous anodic alumina obtained without protective oxide layer by hard anodization*“. *Materials Letters*. (2012) 67:296–299
- [79] F. Li, L. Zhang, R. M. Metzger.” *On the Growth of Highly Ordered Pores in Anodized Aluminum Oxide*“. *Chem. Mater* (1998) 10: 2470-2480
- [80] J.H. Fendle. “*Nanoparticles and Nanostructured Films: Preparation, Characterization and applications*“. WILEY-VCH (1998)
- [81] J Wang. “*Analytical electrochemistry*“. Wiley –VCH third edition (2006)
- [82] P.H. Rieger.” *Electrochemistry*“. Chapman & Hall, ink. Second edition (1994)
- [83] C.G.Zoski. “*Handbook of electrochemistry*“. Elsevier (2007)
- [84] D. H. Evans, K.M. O’connelle, A.R. Petersen, M. J. Kelly.” *Cyclic Voltammetry*“. *Journal of chemical education*. (1983) 60(4): 290-293
- [85] E. P. Randviir, C. E. Banks.” *Electrochemical impedance spectroscopy: an overview of bioanalytical applications*“. *Analitical Methods* (2013) 5:1098-1115
- [86] Salaneck W R, Friend R H, Bredas “*Electronic structure of conjugated polymers: consequence of electron-lattice coupling*“. *Physics Reports* (1999) 319: 231-251
- [87] A.O. Patil, A.J. Heeger, F. Wudl.” *Optical properties of conducting polymers*.” *Chem. Rev* (1988) 88: 183-200
- [88] C. Pratt. “*Effect of metal ions on the synthesis and properties of conducting polymers*.” Kingston University (2003)
- [89] E. Salatelli, L. Angiolini, L. Brazzi, M. Lanzi, E. Scavetta, D. Tonelli.”*Synthesis, characterization and electrochemical properties of new functional polythiophenes*“. *Synthetic Metals* (2010) 160: 2681-2686
- [90] A. Dadras Marani, A. Entezami.”*New Synthesis Method of Polythiophene*.” *Plymer science and technology* (1994) 3: 2-12
- [91] C. Lai, W. Guo, X. Tang, G. Zhang, Q. Pan, M. Pei.”*Cross-linking conducting polythiophene with yellow-green light-emitting properties and good thermal stability via free radical polymerization and electropolymerization*“. *Synthetic Metals* (2011) 16: 1886-1891
- [92] B. Senthilkumar, P. Thenamirtham, R. Selvan.” *Structural and electrochemical properties of polythiophene*.” *Applied Surface Science* (2011) 257: 9063-9067



- 
- [93] V. Cocchi, L. Guadagnini, A. Mignani, E. Salatelli, D. Tonelli. "Electrosynthesis and characterization of a conductive polythiophene deriving from a terthiophene monomer." *Electrochimica Acta* (2011) 56: 6976-6981
- [94] J. C. Nolasco, R. Cabré, J. Ferré-Borrull, L. F. Marsal, M. Estrada, J. Pallarès. "Extraction of poly(3-hexylthiophene)(P3HT) properties from dark current voltage characteristics in a P3HT/n-crystalline-silicon solar cell". *J. Appl. Phys.* (2010) 107: 044505(1)-044505(4)
- [95] M. J. Panzer, C. D. Frisbie. "High carrier density and metallic conductivity in poly(3-hexylthiophene) achieved by electrostatic charge injection." *Adv. Funct. Mater* (2006) 16:1051–1056
- [96] B. Oregan, M. Grätzel. "A low-cost, high-efficiency solar cells based on dye-sensitized colloidal TiO<sub>2</sub> films." *Nature* (1991) 353 (6346) 737-740
- [97] F. Cao, G. Oskam, P. C. Searson. "A solid-state, dye-sensitized photoelectrochemical solar cells". *J. Phys. Chem* (1995) 99:17071- 17073
- [98] J. Hagen, W. Schaffrath, P. Otschik, R. Fink, A. Bacher, H. W. Schmidt, D. Haarer. "Novel hybrid solar cells consisting of inorganic nanoparticles and an organic hole transport material". *Synthetic Metals* (1997) 89:215-220
- [99] U. Bach, D. Lupo, P. Comte, J. E. Moser, F. Weissörtel, J. Salbeck, H. Spreitzer, M. Grätzel. "Solid-state dye-sensitized mesoporous TiO<sub>2</sub> solar cells with high photon-to-electron conversion efficiencies". *Nature* (1998) 395, 583-585
- [100] J. J. Dittmer, E. A. Marseglia, R. H. Friend. "Electron trapping in dye/polymer blend photovoltaic cells". *Adv. Mater* (2000) 12:1270-1274
- [101] K. Petritsch, J. J. Dittmer, E. A. Marseglia, R. H. Friend, A. Lux, G. G. Rozenberg, S. C. Moratti, A. B. Holmes. "Dye-based donor/acceptor solar cells". *Solar Energy Materials & Solar Cells* (2000) 61: 63-72
- [102] R. Plass, S. Pelet, J. Krueger, M. Grätzel. "Quantum dot sensitization of organic-inorganic hybrid solar cells". *J. Phys. Chem. B* (2002) 106: 7578-7580
- [103] W. U. Huynh, J. J. Dittmer, A. P. Alivisatos. "Hybrid nanorod-polymer solar cells". *Science* (2002) 295: 2425-2427
- [104] W. U. Huynh, J. J. Dittmer, W. C. Libby, G. L. Whiting, A. P. Alivisatos. "Controlling the Morphology of Nanocrystal-Polymer Composites for Solar Cells". *Adv. Funct. Mater* (2003) 13:73-79
- [105] S. Dayal, N. Kopidakis, D. C. Olson, D. S. Ginley, G. Rumbles, "Photovoltaic devices with a low band gap polymer and CdSe nanostructures exceeding 3% efficiency," *Nano Letters* (2010) 10: 239–242
- [106] L. Han, D. X. Jiang, "Synthesis of high quality zinc-blende CdSe nanocrystals and their application in hybrid solar cells," *Nanotechnology* (2006) 17:4736–4742
- [107] J. D. Olson, G. P. Gray, and S. A. Carter, "Optimizing hybrid photovoltaics through annealing and ligand choice," *Solar Energy Materials and Solar Cells* (2009) 93: 519–523
- [108] N. Radychev, I. Lokteva, F. Witt, J. K. Olesiak, H. Borchert, and J. Parisi, "Physical origin of the impact of different nano-crystal surface modifications on the performance of CdSe/ P3HT hybrid solar cells," *Journal of Physical Chemistry C* (2011) 115: 14111–14122
- [109] W. J. E. Beek, M. M. Wienk, M. Kemerink, X. Yang, R. A. J. Janssen. "Hybrid zinc oxide conjugated polymer bulk heterojunction solar cells". *J. Phys. Chem. B* (2005) 109: 9505-9516
- [110] D. C. Olson, J. Piris, R. T. Collins, S. E. Shaheen, D. S. Ginley. "Hybrid photovoltaic devices of polymer and ZnO nanofiber composites". *Thin Solid Films* (2006) 496: 26 – 29
- [111] D. C. Olson, Y. J. Lee, M. S. White, N. Kopidakis, S. E. Shaheen, D. S. Ginley, J. A. Voigt, J. W. P. Hsu. "Effect of polymer processing on the performance of poly(3-hexylthiophene)/ZnO nanorod photovoltaic devices." *J. Phys. Chem. C* (2007) 111:16640-16645
- [112] Kline R J, McGehee M D. "Morphology and charge transport in conjugated polymers". *Macromolecular Science C* (2006) 46:27-45

- 
- [113] J. S. Kim, Y. Park, D. Y. Lee, J. H. Lee, J. H. Park, J. K. Kim, K. Cho." *Poly(3-hexylthiophene) nanorods with aligned chain orientation for organic photovoltaics*". Adv. Funct. Mater. (2010) 20: 540–545
- [114] D. Chen, W. Zhao, T.P. Russell." *P3HT nanopillars for organic photovoltaic devices nanoimprinted by AAO templates*". ACS nano (2012) 6(2):1479-1485
- [115] F. Kadirgan, D. Mao, W. Song, T. Ohno, B. McC. Andless." *Properties of electrodeposited cadmium sulfide films for photovoltaic devices with comparison to CdS films prepared by other methods*". Turk J Chem (2000) 24:21 – 33
- [116] A.C. Rastogi, K.S. Balakrishnan, R.K. Sharma, Kiran Jain." *Growth phases during electrochemical selenization of vacuum deposited CuIn metal layers for the formation of semiconducting CuInSe<sub>2</sub> films*". Thin Solid Films (1999) 357: 179–188
- [117] A.C. Rastogi, K.S. Balakrishnan, Kiran Jain." *Growth and properties of CdSe thin films by a new process of electrochemical selenization of Cd metal layers*". Materials Research Bulletin (1999) 34:1319-1332
- [118] K.S. Balakrishnan, A.C. Rastogi." *Electrochemical deposition and characterization of phosphorous doped p-CdTe thin films*". Solar Energy Materials (1991) 23:61-73
- [119] T. Pauporte', D. Lincot." *Electrodeposition of semiconductors for optoelectronic devices: results on zinc oxide*". Electrochimica Acta (2000) 45: 3345–3353
- [120] C. D. Lokhande, M. S. Jadhav, S. H. Pawar." *Electrodeposition of ZnS films from an alkaline bath*". J. Electrochem. Soc. (1989) 136 (9): 2756-2758
- [121] S. Sawatani, T. Yoshida, T. Ohya, T. Ban, Y. Takahashi, H. Minoura." *Electrodeposition of TiO<sub>2</sub> thin film by anodic formation of titanate/benzoquinone hybrid*". Electrochem. Solid-State Lett (2005) 8(5):C69-C71
- [122] S. Glenis, G. Horowitz, G. Tourillon, F. Garnier." *Electrochemically grown polythiophene and poly(3-methylthiophene) organic photovoltaic cells*". Thin Solid Films (1984) 111:93-103
- [123] Y. Kang, N.G Park, D. Kim." *Hybrid solar cells with vertically aligned CdTe nanorods and a conjugated polymer*". Applied Physic letter (2005) 86: 113101(1)-113101(3)
- [124] Z. Yin, Sh. Wu, X. Zhou, X. Huang, Q. Zhang, F. Boey, H. Zhang." *Electrochemical deposition of ZnO nanorods on transparent reduced graphene oxide electrodes for hybrid solar cells*". Small (2010) 6(2): 307–312
- [125] C. Te. Hsieh, S. Y. Yang, J.Y. Lin." *Electrochemical deposition and superhydrophobic behavior of ZnO nanorod arrays*". Thin Solid Films (2010) 518: 4884–4889
- [126] A. F Diaz, K.K. Kanawaza." *Electrochemical polymerization of pyrrole*". J.C.S.Chem (1979) 373: 635-636
- [127] A . F. Diaz, J. I. Castillo." *A polymer electrode with variable conductivity: Polypyrrole*". J.C.S.Chem.Comm (1980) 397-398
- [128] J. Grimshaw, S. D. Perera." *Electrochemical behaviour of poly(thiophene-benzoquinone) films*". *J. Electroanal. Chem* (1990) 278: 287-294
- [129] S.K. Ritter, R.E. Npftle." *Synthesis, characterization and electropolymerization of thiophene derivatives of the group IV elements*". Chem. Mater (1992) 4: 872-879
- [130] B. Sari, M. Talu." *Electrochemical polymerization and analysis of some aniline derivatives*". Turk J Chem (1998) 22:301-307
- [131] B.Sari, M.Talu, F. Yildirim, E. K. Balci." *Synthesis and characterization of polyurethane/polythiophene conducting copolymer by electrochemical method*". Applied Surface Science (2003) 205:27–38
- [132] S. Y. Kim, K. H. Lee, B. D. Chin, J.W. Yu." *Network structure organic photovoltaic devices prepared by electrochemical copolymerization*". Solar Energy Materials & Solar Cells (2009) 93: 129–135

- 
- [133] E. Salatelli, L. Angiolini, A. Brazzi, M. Lanzi, E. Scavetta, D. Tonelli." *Synthesis, characterization and electrochemical properties of new functional polythiophenes.*" *Synthetic Metals* (2010) 160: 2681–2686
- [134] A. F. Monnin, C. C. Buron, L. Guyard, D. Charraut, R. Salut, C. Filiâtre." *Electrodeposition and characterisation of polythiophene films on gold substrates.*" *Synthetic Metals* (2012) 162:1–9
- [135] J. Roncali." *Conjugated poly (thiophene): synthesis, functionalization and applications.*" *Chem.Rev* (1992) *Chem. Rev* (1992) 92: 711-738
- [136] R.M. Penner, C. R. Martin." *Controlling the morphology of electronically conductive polymers*". *Journal of Electrochemical Society* (1986) 133(10) 2206-2207
- [137] Z.Cai, C.R. Martin." *Electronically conductive polymer fibers with mesoscopic diameters show enhanced electronic conductivities.*" *J.Am.Chem.Soc* (1989) 111:4138-4139
- [138] R. Schrebler, P. Grez, P. Cury, C. Veas, M. Merino, H. Gomez, R. Cordova, M.A. del Valle." *Nucleation and growth mechanisms of poly(thiophene) Part 1. Effect of electrolyte and monomer concentration in dichloromethane*". *Journal of Electroanalytical Chemistry* (1997) 430: 77-90
- [139] H.T. Santoso, V. Singh, K. Kalaitzidou, B. A. Cola." *Enhanced molecular order in polythiophene films electropolymerized in a mixed electrolyte of anionic surfactants and boron trifluoride diethyl etherate.*" *Appl. Mater. Interfaces* (2012) 4:1697–1703
- [140] E. Nasybulin, M. Cox, I. Kymissis, K. Levon." *Electrochemical codeposition of poly(thieno[3,2-b]thiophene) and fullerene: An approach to a bulk heterojunction organic photovoltaic device*". *Synthetic Metals* (2012) 162:10–17
- [141] F. B.Koyuncu, S. Koyuncu, E. Ozdemir ." *A new donor–acceptor carbazole derivative: Electrochemical polymerization and photo-induced charge transfer properties.*" *Synthetic Metals* (2011) 161:1005–1013
- [142] M. Kabasakaloglu, T. Kiyak, H. Toprak, M. L. Aksu." *Electrochemical properties of polythiophene depending on preparation conditions.*" *Applied Surface Science* (1999) 152:115–125
- [143] A.A. El-Maghraby, G.M. Abou-Elenien, G.M. El-Abdallah." *Electrochemical relaxation study of polythiophene as a conducting polymer (II).*" *Synthetic Metals* (2010) 160:1335–1342
- [144] F. Mammeri, E. Le Bourhis, L. Rozes, C.Sanchez." *Mechanical properties of hybrid organic–inorganic materials*". *J. Mater. Chem* (2005)15: 3787–3811
- [145] S. Ren, L.Y. Chang, S.K. Lim, J. Zhao, M. Smith, N. Zhao, V. Bulovic, M. Bawendi, S. Gradecak, " *Inorganic–Organic hybrid solar cell: bridging quantum dots to conjugated polymer nanowires*". *Nano Letters* (2011) 11: 3998–4002
- [146] W.C. Kwak, T.G. Kim, W. Lee, S.H. Han, Y.-M. Sung. " *Template-free liquid-phase synthesis of high-density CdS nanowire arrays on conductive glass*". *Physical Chemistry C* (2009) 113:1615–1619
- [147] L. Wang, Y. Liu, X. Jiang, D. Qin, Y. Cao. " *Enhancement of photovoltaic characteristics using a suitable solvent in hybrid polymer/multiarmed CdS nanorods solar cells.*" *Physical Chemistry C* (2007) 111:9538–9542
- [148] K.F. Jeltsch, M. Schadel, J.-B. Bonekamp, P. Niyamakom, F. Rauscher, H.W.A. Lademann, I. Dumsch, S. Allard, U. Scherf, K. Meerholz. " *Efficiency enhanced hybrid solar cells using a blend of quantum dots and nanorods*". *Advanced Functional Materials* (2012) 22:397–404
- [149] R. Zhou, Y. Zheng, L. Qian, Y. Yang, P.H. Holloway, J. Xue. " *Solution-processed, nanostructured hybrid solar cells with broad spectral sensitivity and stability*". *Nanoscale* (2012) 4:3507–3514
- [150] Y. Wu, G. Zhang. " *Performance enhancement of hybrid solar cells through chemical vapor annealing*". *Nano Letters* (2010) 101628–1631

- 
- [151] B. Sun, H.J. Snaith, A.S. Dhoot, S. Westenhoff, N.C. Greenham. “*Vertically segregated hybrid blends for photovoltaic devices with improved efficiency*”. *Applied Physics* (2005) 97: 014914–014916
- [152] C.Y. Kuo, M.S. Su, G.Y. Chen, C.S. Ku, H.Y. Lee, K.H. Wei. “*Annealing treatment improves the morphology and performance of photovoltaic devices prepared from thieno[3,4-*c*]pyrrole-4,6-dione-based donor/acceptor conjugated polymers and CdSe nanostructures*”. *Energy & Environmental Science* (2011) 4: 2316–2322
- [153] M.J. Greaney, S. Das, D.H. Webber, S.E. Bradforth, R.L. Brutchey. “*Improving open circuit potential in hybrid P3HT:CdSe bulk heterojunction solar cells via colloidal tertabutylthiol ligand exchange*”. *ACS Nano* (2012) 6: 4222–4230
- [154] J. Yang, A. Tang, R. Zhou, J. Xue. “*Effects of nanocrystal size and device aging on performance of hybrid poly(3-hexylthiophene):CdSe nanocrystal solar cells*”. *Solar Energy Materials and Solar Cells* (2011) 95:476–482
- [155] W. Yu, H. Zhang, Z. Fan, J. Zhang, H. Wei, D. Zhou, B. Xu, F. Li, W. Tian, B. Yang. “*Efficient polymer/nanocrystal hybrid solar cells fabricated from aqueous materials*”. *Energy & Environmental Science* (2011) 112: 2831–2834
- [156] H.C. Chen, C.W. Lai, I.C. Wu, H.R. Pan, I.W.P. Chen, Y.K. Peng, C.L. Liu, C.h. Chen, P.T. Chou. “*Enhanced performance and air stability of 3.2% hybrid solar cells: how the functional polymer and CdTe nanostructure boost the solar cell efficiency*”. *Advanced Materials* (2011) 23: 5451–5455
- [157] Z. Fan, H. Zhang, W. Yu, Z. Xing, H. Wei, Q. Dong, W. Tian, B. Yang. “*Aqueous-solution-processed hybrid solar cells from Poly(1,4-naphthalenevinylene) and CdTe nanocrystals*”. *ACS Applied Materials & Interfaces* (2011) 3: 2919–2923
- [158] Y.Y. Yu, W.C. Chien, Y.H. Ko, S.H. Chen. “*Preparation and characterization of P3HT:CuInSe<sub>2</sub>:TiO<sub>2</sub> thin film for hybrid solar cell applications*”. *Thin Solid Films* (2011) 520:1503–1510
- [159] A.R.W. Andrew, B. David, H.W. Jamie, A.T. Elizabeth, L.T. Eric, R.D. Halina, M. Paul. “*Lead sulfide nanocrystal: conducting polymer solar cells*”. *Journal of Physics D: Applied Physics* (2005) 38: 2006
- [160] A. Guchhait, A.K. Rath, A.J. Pal. “*To make polymer: quantum dot hybrid solar cells NIR-active by increasing diameter of PbS nanoparticles*”. *Solar Energy Materials and Solar Cells* (2011) 95 :651–656
- [161] C.Y. Liu, Z.C. Holman, U.R. Kortshagen. “*Optimization of Si NC/P3HT hybrid solar cells*”. *Advanced Functional Materials* (2010) 20:2157–2164
- [162] J .S. Huang, C.Y. Hsiao, S. Syu, J.J. Chao, C.F. Lin. “*Well-aligned single- crystalline silicon nanowire hybrid solar cells on glass*.” *Solar Energy Materials and Solar Cells* (2009) 93:621–624
- [163] H.J. Syu, S.C. Shiu, C.F. Lin. “*Silicon nanowire/organic hybrid solar cell with efficiency of 8.40%*.” *Solar Energy Materials and Solar Cells* (2012) 98: 267–272
- [164] H.R. Tan, X.W. Zhang, F.R. Tan, H.L. Gao, Z.G. Yin, Y.M. Bai, X.L. Zhang, S.C. Qu. “*Performance improvement of conjugated polymer and ZnO hybrid solar cells using nickel oxide as anode buffer layer*.” *Physica status solidi (a)* (2011) 208 :2865–2870
- [165] W. Chen, Y. Chen, F. Li, L. Chen, K. Yuan, K. Yao, P. Wang. “*Ordered microstructure induced by orientation behavior of liquid-crystal polythiophene for performance improvement of hybrid solar cells*.” *Solar Energy Materials and Solar Cells* (2012) 962:66–275
- [166] A.L. Briseno, T.W. Holcombe, A.I. Boukai, E.C. Garnett, S.W. Shelton, J.J.M. Frechet, P. Yang. “*Oligo- and polythiophene/ZnO hybrid nanowire solar cells*.” *Nano Letters* (2009) 10:334–340

- 
- [167] M. Bredol, K. Matras, A. Szatkowski, J. Sanetra, A. Prodi-Schwab." *P3HT/ZnS: a new hybrid bulk heterojunction photovoltaic system with very high open circuit voltage.*" *Solar Energy Materials and Solar Cells* (2009) 93: 662–666
- [168] J. Lee, J.Y. Jho." *Fabrication of highly ordered and vertically oriented TiO<sub>2</sub> nanotube arrays for ordered heterojunction polymer/inorganic hybrid solar cell.*" *Solar Energy Materials and Solar Cells* (2011) 95:3152–3156
- [169] Y.Y. Lin, T.H. Chu, S.S. Li, C.H. Chuang, C.H. Chang, W.F. Su, C.P. Chang, M.W. Chu, C.W. Chen. " *Interfacial nanostructuring on the performance of polymer/TiO<sub>2</sub> nanorod bulk heterojunction solar cells.*" *American Chemical Society* (2009) 131: 3644–3649
- [170] A. Abruci, I.K. Ding, M. Al-Hashimi, T. Segal-Peretz, M.D. McGehee, M. Heeney, G.L. Frey, H.J. Snaith." *Facile infiltration of semiconducting polymer into mesoporous electrodes for hybrid solar cells.*" *Energy & Environmental Science* (2011) 4: 3051–3058
- [171] S. Jeong, E. C. Garnett, S. Wang, Z. Yu, S. Fan, M. L. Brongersma, M. D. McGehee, Y. Cui." *Hybrid silicon nanocone–polymer solar cells*". *Nano Lett* (2012) 12:2971–2976
- [172] V. Kaltenhauser, T.Rath, M. Edler, A. Reichmann, G. Trimmel." *Exploring polymer/nanoparticle hybrid solar cells in tandem architecture*". *RSC Adv* (2013) 3:18643–18650
- [173] W.R Wei, M. L. Tsai, S. T. Ho, S. H. Tai, C. R. Ho, S.H. Tsai, C. W. Liu, R. J Chung, J. H. He." *Above-11%- efficiency organic-inorganic hybrid solar cells with omnidirectional harvesting characteristics by employing hierarchical photon-trapping structures.*" *Nano Lett* (2013)13: 3658–3663
- [174] F. C. Krebs." *Air stable polymer photovoltaics based on a process free from vacuum steps and fullerenes.*" *Sol. Energy Mater. Sol. Cells* (2008) 92:715-726
- [175] B. Azzopardi, J. Mutale." *Life cycle analysis for future photovoltaic systems using hybrid solar cells*". *Renewable and Sustainable Energy Reviews* (2010) 14:1130–1134
- [176] S. Shoaee, J. Briscoe, J. R. Durrant, S.e Dunn." *Acoustic Enhancement of Polymer/ZnO Nanorod Photovoltaic Device Performance*". *Adv. Mater* (2014) 26: 263–268
- [177] S. Shingubara, H. Hiroshima, " *Fabrication of nanomaterials using porous alumina templates*". *Journal of Nanoparticle Research* (2003) 5:17–30
- [178] S. Öztürk, N.Tasaltın, N. Kılınç, H. Yüzer, Z. Z. Öztürk." *Fabrication of ZnO nanowires at room temperature by cathodically induced sol–gel method*". *Appl Phys A* (2010) 99: 73–78.
- [179] G.Meng, T. Yanagida, K. Nagashima, T. Yanagishita, M. Kanai, K. Oka, A. Klamchuen, S. Rahong, M. Horprathum, B. Xu, F. Zhuge, Y. He, H. Masuda, T.Kawai ." *Facile and scalable patterning of sublithographic scale uniform nanowires by ultra-thin AAO free-standing membrane*". *RSC Adv* (2012) 2:10618–10623
- [180] Y. Du, S.Z. Shen, W.D. Yang, S. Chen, Z. Qin, K.F. Cai, P.S. Casey." *Facile preparation and characterization of poly (3-hexylthiophene)/multiwalled carbon nanotube thermoelectric composite films*". *Electronic material* (2012) 41(6): 1436-1441
- [181] M.E. Nicho, C.H. Escobar, M.C. Arenas, P. Altuzar-Coello, R. Cruz-Silva, M. Güizado-Rodríguez." *Microwave-assisted synthesis of poly(3-hexylthiophene) via direct oxidation with FeCl<sub>3</sub>* ". *Materials Science and Engineering* (2011) B(177): 176 :1393
- [182] S.S Jeon, S.J. Yang, K.J Lee, S.S.Im," *A facile and rapid synthesis of un-substituted polythiophene with high electrical conductivity using binary organic solvents*". *Polymer* (2011) 51: 4069-4076
- [183] P. S. Sharma. A. Pietrzyk-Le. F. D'Souza. W. Kutner." *Electrochemically synthesized polymers in molecular imprinting for chemical sensing*". *Anal Bioanal Chem* (2012) 402(3):177–3204
- [184] H. Masuda." *Ordered Metal Nanohole Arrays Made by a Two-Step Replication of Honeycomb Structures of Anodic Alumina.*" *Science* (1995) 268: 1466-1468

- 
- [185] O. Jessensky, F. Muller, U. Gosele. "Self-organized formation of hexagonal pore arrays in anodic alumina." *Applied Physics Letters* (1998) 72: 1173-1175
- [186] S.Chu, K. Wada, S. Inoue, M. Isogai, A.Yasumori. "Fabrication of ideally ordered nanoporous alumina films and integrated alumina nanotubule arrays by high-field anodization." *Adv. Mater* (2005) 17: 2115-2119
- [187] G.D. Sulka, K.G. Parkoła. "Temperature influence on well-ordered nanopore structures grown by anodization of aluminium in sulphuric acid." *Electrochimica Acta* (2007) 52:1880–188
- [188] Y. C. Choi, J. Y. Hyeon, S. D. Bu. "Effects of anodizing voltages and corresponding current densities on self-ordering process of nanopores in porous anodic aluminas anodized in oxalic and sulfuric acids." *Journal of the Korean Physical Society* (2009) 55: 835-840
- [189] N. Tasaltin, S. Ozturk, N. Kilinc, H. Yuzer, Z. Ozturk. "Simple fabrication of hexagonally well-ordered AAO template on silicon substrate in two dimensions." *Appl Phys A* (2009) 95: 781–787
- [190] P. Chowdhury, K. Raghuvanan, M. Krishnan, H.C. Barshilia, K.S. Rajam. "Effect of process parameters on growth rate and diameter of nano-porous alumina templates." *Bull. Mater. Sci* (2011) 34: 423–427
- [191] W. J. Stepniowski, D. Zasada, Z. Bojar. "Synthesis of anodic aluminum oxide (AAO) at relatively high temperatures. Study of the influence of anodization conditions on the alumina structural features." *Surface & Coatings Technology* (2011) 206: 265–272
- [192] W. J. Stepniowski, A. Stepniowska, M. Domańska, M. Norek, T. Czujko, Z. Bojar. "Fabrication and geometric characterization of highly-ordered hexagonally arranged arrays of nanoporous anodic alumina." *Polish Journal of Chemical Technology* (2013) 16: 63-69
- [193] K. Nielsch, J. Choi, K. Schwirn, R. B. Wehrspohn, U. Gusele. "Self-ordering regimes of porous alumina: The 10% porosity rule." *Nano letters* (2002) 2: 677-680
- [194] G. E. Totten, D.S. Mackenzie. "Handbook of aluminum, Physical Metallurgy and processes." Marcel Decker Inc vol. 1(2003)
- [195] G. D. Sulka, K. G. Parkola. "Anodising potential influence on well-ordered nanostructures formed by anodisation of aluminium in sulphuric acid". *Thin Solid Films* (2006) 515:338 – 345
- [196] W. Lee, R. Ji, U. Gosele, K. Nielsch. "Fast fabrication of long-range ordered porous alumina membranes by hard anodization." *Nature materials* (2006) 5: 741-747
- [197] T.Y. Kim, S.H. Jeong. "Highly ordered anodic alumina nanotemplate with about 14 nm diameter." *Korean J. Chem. Eng* (2008)25(3):609-611
- [198] L. Zaraska, G.D. Sulka, J. Szeremeta, M. Jaskuła. "Porous anodic alumina formed by anodization of aluminum alloy (AA1050) and high purity aluminum". *Electrochimica Acta* (2010) 55:4377–4386
- [199] G. Eddy, J. Poinern, N. Ali, D. Fawcett. "Progress in nano-engineered anodic aluminum oxide membrane development." *Materials* (2011) 4:487-526
- [200] W. J. Stepniowski, D. Zasada, Z. Bojar. "First step of anodization influences the final nanopore arrangement in anodized alumina." *Surface & Coatings Technology* (2011) 206 :1416–1422
- [201] L. Zaraska, W. J. Stepniowski, E. Ciepiela, G. D. Sulka. "The effect of anodizing temperature on structural features and hexagonal arrangement of nanopores in alumina synthesized by two-step anodizing in oxalic acid." *Thin Solid Films* (2013) 534: 155–161
- [202] H. Hagemam, R.G. Snyder. "Quantitative infrared methods for the measurement of crystallinity and its temperature dependence: polyethylene." *Macromolecules* (1989) 22:3600-3606
- [203] L.R. Chen, L. Z.Ping. "Polythiophene: synthesis in aqueous medium and controllable morphology." *Chinese Sci* (2009) 54: 2008-2032
- [204] X. Chen. K. Z. Xing, O. Inganaes. "Electrochemically induced volume changes in poly(3,4-ethylenedioxythiophene)." *Chemistry of Materials* (1996) 10(8): 2439-2443

- 
- [205] R.K Singh, J. Kumar, R. Singh, R. Kant, R. C. Rastogi, S. Chand, V. Kumar. “*Structure–conductivity correlation in ferric chloride-doped poly (3-hexylthiophene)*.” New Journal of Physics (2006) 8: 112-132
- [206] L. B. Groenendaal, F. Jonas F, D. Freitag, H. Pielartzik, R. J. Reynolds.” *Poly (3,4-ethylenedioxythiophene) and its derivatives: past, present, and future.*” Advanced Materials (2000) 12:481-494
- [207] R. D. McCullough, R. D. Lowe, M. Jayaraman, D. L. Anderson.” *Design, synthesis, and control of conducting polymer architectures: structurally homogeneous poly (3-alkylthiophenes).*” Org. Chem (1993) 58:904-912
- [208] S. R. P. Gnanakan, M. Rajasekhar, A. Subramania.” *Synthesis of polythiophene nanoparticles by surfactant- assisted dilute polymerization method for high performance redox supercapacitors.* Int. J. Electrochem. Sci (2009) 4:1289-1301
- [209] A. Mosra, P. Kumar, R. Srivastava, S.K. Dhawan, M. N. Kamalasanam, S. Chandra. “*Electrochemical and optical studies of conjugated polymers for three primary colours*”. Indian journal of Pure & Applied Physics (2005) 3: 921-925
- [210] E. Kim, Z. T. Jiang, K. No.” *Measurement and calculation of optical band gap of chromium aluminum oxide films.*” Journal of applied physics (2000) 39:4820-4825
- [211] L.S. Van Dyke, C.R. Martin. “*Electrochemical investigations of electronically conductive polymers. 4. Controlling the supermolecular structure allows charge transport rates to be enhanced*”. Langmuir (1990) 6: 1118-1123
- [212] J. M. Palmer.”*The measurement of transmission, absorption, emission and reflection*”. handbook of optics : Fundamentals, techniques and design. McGraw-Hill Volume 1 (1994)
- [213] F. Yakuphanoglu, S. Ilican, , M. Caglar, Y. Caglar.” *The determination of the optical band and optical constants of non-crystalline and crystalline ZnO thin films deposited by spray pyrolysis.*” Journal of optoelectronics and advanced materials (2007) 9: 2180 – 2185
- [214] R. Rusdi, A. Abd Rahman, N. S. Mohamed, N. Kamarudin, N. Kamarulzaman.” *Preparation and band gap energies of ZnO nanotubes, nanorods and spherical nanostructures.*” Powder Technology (2011) 210:18–22